To Marta, my wife…
for she exists

Contents

List of abbreviations

AM	Angular momentum
AHM	Adaptive helical mirror
BPM	Beam propagation method
CGH	Computer generated hologram
CP	Circularly polarized
FF	First fundamental
FFT	Fast Fourier Transform
HG	Hermite – Gaussian modes
HM	Helical mirror
IMI	Insulator – Metal – Insulator
LG	Laguerre – Gaussian modes
LP	Linearly polarized
MIM	Metal – Insulator – Metal
OAM	Orbital angular momentum
OV	Optical vortex
PSPP	Plasmonic Spiral Phase Plate
PVL	Plasmonic vortex lens
PWE	Paraxial wave equation
PZT	Piezoelectric transducer

SAM	Spin angular momentum
SH	Second harmonic
SHG	Second harmonic generation
SP	Surface plasmon
SPM	Spiral phase mirror
SPP	Spiral phase plate
SPP	Surface Plasmon polariton
SVEA	Slowly Varying Envelope Approximation

Chapter 1

Introduction

It is well known that light, just like many other physical phenomena such as sound and fluids, can be described by means of waves. These are regular solutions of the so – called wave equation, a partial differential equation which allows to analyse and predict the behaviour of such phenomena.
We use to think at waves as oscillations propagating in space and time and represent them through their wave-fronts, that is the locus of points having the same phase. However sometimes there are points or lines in space where a quantity describing the wave experiences jumps or becomes infinite; they are called singularities. In particular, when these abrupt variations happen in the phase of a field, we deal with phase singularities or phase defects, which appear as a veritable tear in the wave-front.
In 1974 Nye and Berry [1] studied and classified these singularities, assimilating them to the defects of crystal lattices and introducing in the physics of waves the crystallographic term "dislocation" to describe the structure of the wave-front. In analogy with crystals, they therefore identified three main kind of phase defects: edge, screw and mixed edge – screw dislocations.
Edge dislocations consist of semi-infinite lines of discontinuity introduced by enclosing a half plane in the wave-front (or in the crystal lattice); on the other hand screw dislocations take their name from the spiralling path which the phase (or the crystal's atoms) covers around the dislocation line. Finally, when a simple edge dislocation ends in a screw one, a mixed edge – screw dislocation is created.

In real wave trains we deal with physical quantities, and thus the amplitude of the considered field must be a continuous function of the spatial coordinates. This implies that at the points of the phase singularity, i.e. where the phase in indeterminate, the field's amplitude must vanish and the dislocation can be described as the locus of points where both the real and imaginary parts of the field equal zero. This mean that optical singularities can be seen as the locus of zero intensity.
Undoubtedly, the most fascinating and studied phase singularities are the vortices, which are the clearest example of screw dislocation. Their typical feature is a helical phase distribution which entails the circulation of the wave's energy around the dislocation line thus the presence of angular momentum.

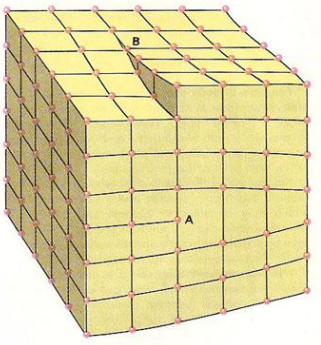

Figure 1.1. Dislocations in a crystal lattice. The edge dislocation (A) appears as an extra half plane of atoms, while in the screw dislocation (B) the atomic planes compose a helical structure around the dislocation line.

Vortices can be found in a large amount of physics branches, from classical fluids to quantum systems like super-fluids, to light.
As a matter of fact in optics, the latter are commonly known as optical vortices (OVs) and, since the seminal paper of Nye and Berry on wave dislocations, they were deeply investigated because of their manifold applications. The helical phase distribution associated to OVs and the corresponding rotating energy flow, allowed to use these fields for particles trapping [2] and manipulation [3] (optical tweezers). Furthermore, the

stability of such configurations is particularly suitable for optical computing, for the generation of optical solitons [4], and grants light by light wave guiding. Moreover the dark core of the OVs makes theme suitable for both astronomical [5, 6] and microscopy applications [7]. Finally, one of the most important features of OVs, the orbital angular momentum (OAM) of light, can play a considerable role in quantum information [8] for the generation of multi – dimensional quantum bits (qudits).

From the non exhaustive list of applications of OVs written above emerges that it is a crucial point to obtain an accurate control over features of OVs such as OAM. In particular this allows to extend the ability of manipulating particles and, above all, to thoroughly develop the quantum information aspect, by using spatial degrees of freedom for encoding information.

Consequently, the aim of this dissertation is to investigate different aspects of optical vortices, focusing on the generation and control of the orbital angular momentum both by means of linear and nonlinear interactions. Moreover, application of the studied techniques are proposed.

This thesis can be divided in three main parts: a first general section about OVs and OAM; a second part, including chapters 3, 4 and 5, which deals with linear interactions; and a third part which tackles quadratic nonlinear processes and how they affect OAM.

- Chapter 2 presents the general theory of optical vortices and orbital angular momentum, introducing the paraxial wave equation and Laguerre – Gaussian beams and the mathematical formalism used throughout the dissertation. Furthermore the most common techniques for generating OVs are discussed.
- Chapters 3 and 4 show two different methods which allow to generate optical vortex beams. A first approach uses a programmable segmented metallic mirror capable of producing OVs with tuneable topological charge. The second technique takes advantage of plasmonic interactions to generate a field with OAM.
- Chapter 5 proposes an experimental technique for probing the topological charge of an optical vortex generated with the techniques discussed in chapters 3 and 4.

- Chapter 6 investigates the behaviour of beams carrying orbital angular momentum in a quadratic parametric interaction of seeded second harmonic generation (SHG). Theory and numeric simulations are discussed.
- Chapter 7 describes an experiment of non – collinear second harmonic generation by off-axis fractional vortex beams. The focus is on the possibility of controlling the spatial configuration of the generated second harmonic field, holding the OAM to a zero value.
- Chapter 8 draws the conclusions of the thesis by summing up all the salient results.

All the topics discussed in chapters from 3 to 8 are subjects of published or to be submitted papers; furthermore regarding the device proposed in chapter 3 and 4 there are also pending patents.

Part 1

Optical Vortices

Chapter 2

The orbital angular momentum of light

The mechanical properties of electromagnetic fields began to play an important role in physics since 1873, when James Clerk Maxwell published his T*reatise on Electricity and Magnetism* [9]. Only few years after, the idea that electromagnetic radiation may have a direct influence on material objects was seriously considered [10] and finally developed by Poynting [11], who predicted that a circularly polarized light beam could exerts a torque on a mechanical body. Poynting previsions were confirmed by Beth in 1936 [12]: he measured the torque effect on a suspended quarter-wave plate hit by a beam of light with circular polarization and verified that, in agreement with both wave and quantum theories of light, there was an angular momentum transfer between the radiation and the plate. It is a widespread opinion that Beth's experiment laid the foundations for all the following works on the angular momentum (AM) of light, opening the way to this interesting branch of research.

A crucial turn happened when, beside the spin component of the angular momentum (SAM), which is due to the circular polarization of light, the role of the orbital component was made known and related to the helical structure of the phase of beams like Laguerre – Gaussian (LG) modes [13]. The work of Allen *et al.* [14] pointed out the correlation between the AM and the LG modes and the scientific community began to talk about these new, fascinating objects called optical vortices [15]. This, together with the theoretical bases developed by Nye and Berry [1, 16, 17], gave rise to that field of beam optics known as Singular Optics [18].

2.1 General theory of the angular momentum of light

According to the classical electromagnetic theory [19] the linear momentum density of an electromagnetic field is defined as:

$$\Pi = \varepsilon_0 \mathbf{E} \times \mathbf{B}. \tag{2.1}$$

From Eq. (2.1) the angular momentum density of the field can be calculated simply by choosing an appropriate reference point and, being **R** the defined arm, using the general expression of the cross product between the arm and the linear momentum:

$$\mathbf{j} = \varepsilon_0 \mathbf{R} \times \Pi. \tag{2.2}$$

The total angular momentum of the field is obtained by integrating over the whole space with the elementary volume dR

$$\mathbf{J} = \varepsilon_0 \int (\mathbf{R} \times \mathbf{\Pi}) dR. \tag{2.3}$$

It is possible to distinguish two separate components of the total angular momentum **J**, a spin component **S** originated from the polarization of the electromagnetic radiation, and an orbital component **L** which depends, as will be shown later, on the spatial distribution of the field itself. Therefore the first member of Eq. (2.3) can be rewritten as

$$\mathbf{J} = \mathbf{L} + \mathbf{S}. \tag{2.4}$$

This distinction comes from the atomic physics where spin is referred to the rotation of a particle around its centre of mass, while with orbital is intended the rotation with respect to the origin of the reference system.
The above equations have a general validity and can be used to evaluate the angular momentum of any field. However in the most common situation of laser beams, we deal with transverse electromagnetic fields, thus it can be

appropriate to reconsider these results under the hypotheses of the paraxial approximation.

2.2 Angular momentum of paraxial beams

In beam optics the electromagnetic field is supposed to show a slow variation of its transverse profile along the direction of propagation *z*. This means that the considered light beam is well collimated and most of the field's energy is concentrated around the propagation axis [20,21].
This consideration can be transposed in terms of the scalar wave equation by neglecting the second derivative of the field's amplitude $u(x,y,z)$ with respect to *z*. As a matter of fact, a scalar field propagating mainly along *z* can be written as $E = u(x,y,z)e^{ikz}$, where *k* is the wave number. Writing the Helmholtz equation and separating the transverse and longitudinal parts of the Laplace operator the following equation is obtained:

$$\left(\nabla_T^2 + \frac{\partial^2}{\partial z^2}\right)E + k^2 E = 0 \qquad \textbf{(2.5)}$$

By substituting *E* in the above equation and making explicit the transverse Laplacian, after trivial algebraic passages Eq. (2.5) leads to

$$\frac{\partial^2 u}{\partial x^2} + \frac{\partial^2 u}{\partial y^2} + \frac{\partial^2 u}{\partial z^2} + 2ik\frac{\partial u}{\partial z} = 0 \qquad \textbf{(2.6)}$$

As pointed out before, the hypothesis of paraxiality implies that the field's amplitude is slowly varying with *z*, so that the paraxial approximation can be expressed by imposing the condition

$$\frac{\partial^2 u}{\partial z^2} \ll k \frac{\partial u}{\partial z}, \tag{2.7}$$

which allows to rewrite Eq. (2.6) as

$$i \frac{\partial u}{\partial z} = -\frac{1}{2k}\left(\frac{\partial^2 u}{\partial x^2} + \frac{\partial^2 u}{\partial y^2} \right). \tag{2.8}$$

It can be demonstrated [22,23] that, under the paraxial approximation, for a linearly polarized electromagnetic field, the magnetic component assumes the expression of

$$\mathbf{H} = \frac{ik}{\mu_0}\left(u\hat{\mathbf{y}} + \frac{i}{k}\frac{\partial u}{\partial y}\hat{\mathbf{z}} \right) e^{ikz} \tag{2.9}$$

while the electric field becomes

$$\mathbf{E} = ik\left(u\hat{\mathbf{x}} + \frac{i}{k}\frac{\partial u}{\partial y}\hat{\mathbf{z}} \right) e^{ikz} \tag{2.10}$$

By substituting Eqs. (2.9) and (2.10) in Eq. (2.1) the Poynting vector can be found as

$$\mathbf{\Pi} = \frac{\varepsilon_0 \omega}{2i}(u^* \nabla u - u \nabla u^*) + \omega k \varepsilon_0 |u|^2 \hat{\mathbf{z}} \tag{2.11}$$

where the subscripted symbol T is omitted, thus ∇ is intended to represent the transverse gradient operator. Looking at equation (2.11) it can be noticed that the term in round brackets represents the transverse energy flow, while the term proportional to the square modulus of the amplitude *u* stands for the linear momentum density in the direction of propagation.

Of course this treatment can be generalized to the case of a circularly polarized field [22]. Calculations show that, besides the terms of Eq. (2.11), there is an additional contribution due to the mixed products – in Eq. (2.1) – of the orthogonal polarizations: this is the term responsible of the spin component of the angular momentum (SAM).

From what has been said it is clear that paraxial beams find a preferential direction of propagation in the *z* axis, therefore the main component of the electromagnetic field is directed along the $\hat{z}$ unitary vector. From this follows that the arm for determining the angular momentum can be chosen in the transverse plane; hence we can replace $\mathbf{R} = (x,y,z)$ with $\mathbf{r} = (x,y)$.

As a consequence, since the angular momentum is the cross product between the arm **r** and the linear momentum vector, emerges that its dominant component is indeed in the *z* direction.

For the sake of this dissertation the contribution of the polarization to the optical angular momentum will be neglected and focus will be placed on the orbital component (OAM) by considering a linearly polarized paraxial beam.

In this situation the AM that we indicated with **J** coincides with the OAM denoted by the symbol **L**.

It can be easily seen that the cross product between the transverse vector **r** and the linear momentum density vector produces an angular momentum vector which is mainly directed along *z*; furthermore it can be noticed that the *z* component of the orbital angular momentum is totally bound to the transverse component of the linear momentum density.

Since we are interested to the component of the AM along the direction of propagation, by substituting the transverse part of Eq. (2.11) in Eq. (2.3) the expression of the orbital angular momentum of the light beam along the propagation axis *z* can be found as:

$$L_z = \frac{\varepsilon_0 \omega}{2i} \iint \left[\mathbf{r} \times \left(u^* \nabla u - u \nabla u^* \right) \right]_z dr \,. \qquad \textbf{(2.12)}$$

The energy density of the field can be calculated by multiplying the *z* component of the linear momentum density by the speed of light *c*;

therefore it is possible to evaluate the orbital angular momentum of a single photon:

$$\frac{L_z}{W} = \frac{\frac{\varepsilon_0 \omega}{i} \iint \mathbf{r} \times \left(u^* \nabla u \right) dr}{\varepsilon_0 \omega k c \iint |u|^2 \, dr}, \qquad \textbf{(2.13)}$$

being W the energy of the light beam.

It was pointed out that the OAM in the *z* direction comes from the transverse part of the linear momentum vector. In particular the tangential component of the energy flow is directly responsible for the orbital component of the angular momentum. It will be shown later that the latter is a typical feature of the so called helical beams, which are solutions of the wave equations in a cylindrical reference frame. Hence can be useful to reconsider the previous equations writing them in cylindrical coordinates. The transverse position vector thus becomes a function of the polar coordinates $\mathbf{r} = (r,\theta)$ while the amplitude distribution will be $u(r,\theta,z)$.

Looking at Eq. (2.12) it can be noticed that, in cylindrical coordinates, the cross product $\mathbf{r} \times \nabla$ equals the azimuthal derivative operator $\partial / \partial \theta$. Equation (1.12) can thus be rewritten as

$$L_z = \frac{\varepsilon_0}{i\omega} \iint u^*(r,\theta) \frac{\partial}{\partial \theta} u(r,\theta) \, r dr d\theta . \qquad \textbf{(2.14)}$$

The orbital angular momentum per photon can be determined from Eq. (2.13) and is

$$\hbar \ell = \frac{\iint u^*(r,\theta) \frac{\hbar}{i} \frac{\partial}{\partial \theta} u(r,\theta) \, r dr d\theta}{\iint \left| u(r,\theta) \right|^2 r dr d\theta} \qquad \textbf{(2.15)}$$

The symbol $\hbar$ was introduced to point out the analogy with the quantum – mechanical operator of the *z* component of the OAM of a wave function

[23]. In this way Eq. (2.15) represents the expectation value of such quantum operator. From Eq. (2.15) emerges the role of the tangential component of the Poynting vector in the OAM. Therefore, as mentioned before, can be confirmed that while the spin angular momentum depends on the – circular – polarization of the light beam, the OAM is bound to the azimuthal field' spatial configuration.
Some considerations should be added about the nature of the orbital angular momentum. Since the spin angular momentum is due to the polarization of the field, it does not depend upon the chosen reference frame, so it is said to be intrinsic. This is not true about the OAM which has a strong dependence on the spatial field distribution thus is strictly related to the choice of the reference axis; hence it can be defined extrinsic [25]. However it is still possible to find conditions that allow to consider intrinsic the OAM [26]. As a matter of fact, if the direction of the reference axis is chosen in order to make the transverse momentum zero, the orbital angular momentum does not depend anymore upon the lateral position of the axis. It should be noted that this is always true when dealing with helical beams symmetric to the reference axis such as Laguerre – Gaussian beams. Nevertheless the situation drastically changes if these kinds of beams lose their cylindrical symmetry, as, for example, if they are truncated by an aperture.

2.3 Helical beams

Undoubtedly, the most important family of beams carrying orbital angular momentum are the so called helical beams. These are paraxial light beams, which are solutions of the cylindrical wave equation, characterized by a spiral phase distribution which grows linearly with the azimuth angle θ, whirling around the propagation axis: this means that their wave fronts are helicoids. The paraxial field distribution of such beams has the form of

$$u(r,\theta,z) = u_0(r,z)e^{il\theta} \qquad \textbf{(2.16)}$$

where l is an integer index and $u_0(r,z)$ is a complex function rapidly decaying with increasing values of r.

In such fields the phase follows a linear azimuth ramp, increasing, at a fixed value of r, from 0 to 2π as shown in Fig. 2.1. However when r → 0 the phase becomes indeterminate, giving rise to a singularity point which is a screw wave front dislocation or, in other words an optical vortex. From the definition of phase dislocation introduced in chapter 1 entails in correspondence to the defect's axis, there is a point of destructive interference where both the real and imaginary parts of the field vanish.

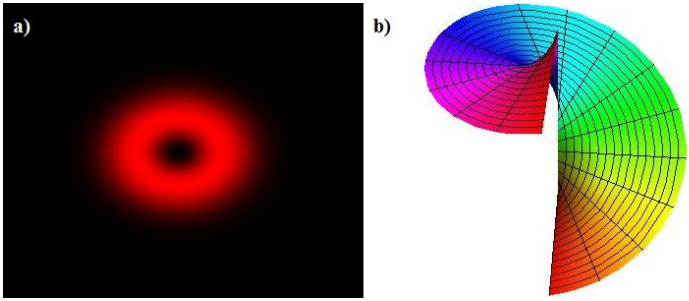

Figure 2.1. Wave front of a helical beam. The phase spirals around the beam's axis, raising from 0 to 2π. The axis corresponds to a line where phase is undetermined so that a screw dislocation is created.

This makes the beam to appear as a annular spot with a dark core, a feature that made theme earn the name of "doughnut modes".

A parameter can be introduced to characterize such vortex beams: the topological charge Q defined by means of the circulation integral

$$Q = \frac{1}{2\pi}\oint d\Phi \qquad \textbf{(2.17)}$$

being Φ the phase of the field. Here Q is an integer number, positive or negative, depending on the handedness of the helicoids, which represents the winding number of the phase around the dislocation line, or rather the number of 2π jumps which happen in a line enclosing the singularity.

Among helical beams, Laguerre – Gaussian (LG) [27] modes are the most common, since they can be generated as modes of a circular laser resonator.

In a cylindrical coordinates system, a normalized LG mode can be written as:

$$\psi_{p,l}^{LG}(r,\theta,z) = U_{p,l}\left(\frac{r\sqrt{2}}{w}\right)^{|l|} e^{-\left[\frac{ik}{2R(z)}-\frac{1}{w}\right]r^2} e^{i\left[kz-(2p+|l|+1)\arctan\left(\frac{z}{z_r}\right)\right]} e^{il\theta} L_p^{|l|}\left(\frac{2r^2}{w^2}\right) \quad \textbf{(2.18)}$$

where

$$U_{p,l} = \frac{1}{w}\sqrt{\frac{2p!}{\pi(p+|l|)}} \quad \textbf{(2.19)}$$

are the normalized coefficients, w is the z-dependent spot size, R(z) is the radius of the wave front curvature for a fixed z, z_r is the Rayleigh range, $L_p^{|l|}$ are the generalized Laguerre polynomials of indices p and l with argument $\frac{2r^2}{w^2}$. The distinctive indices p and l are integer numbers and represent respectively the number of nodes in the radial distribution and the phase change, modulo 2π, in a closed loop around the circumference of the beam axis, thus the topological charge Q.

Besides Laguerre – Gaussian modes, another family of helical beams are the Bessel – Gaussian beams, which have a transverse profile modulated by Bessel functions of the first kind with argument r. their inte

The doughnut structure of such fields is produced by the rotation, during the wave oscillation, of the electric field around the beam's axis; this, joined with the propagation along z generates a helical wave front and produces an orbital angular momentum.

The presence of OAM can be easily explained thinking that the Poynting vector is always perpendicular to the wave front surface [18]. In the case of a helical beam, the wave front surface is a helicoid; this means that, locally, the Poynting vector is tilted of an angle proportional to the slope of the phase ramp. Therefore there is a nonzero tangential component that results, as mentioned before, in orbital angular momentum.

The orbital angular momentum of such helical beams can be easily determined if we refer to the field distribution expressed by Eq. (2.16).

Since OAM is a constant of propagation, it can be evaluated for any value of *z*, thus can be opportune to choose the plane $z = 0$.
As a matter of fact, by substituting the expression of a generic helical beam in equation (2.14) we obtain

$$L_z = \frac{l}{\omega}\iint \varepsilon_0 \left|u_0(r)\right|^2 r dr d\theta \qquad \textbf{(2.20)}$$

It is possible to recognize that the integral in the above equation is the beam energy *W*. The *z* component of the total orbital angular momentum of the electromagnetic field thus can be written in the following way:

$$L_z = \frac{l}{\omega} W \qquad \textbf{(2.21)}$$

The beam energy can also be expressed in terms of the number of photons N, as $W = N\hbar\omega$ which makes Eq.(2.21) become

$$L_z = lN\hbar \qquad \textbf{(2.22)}$$

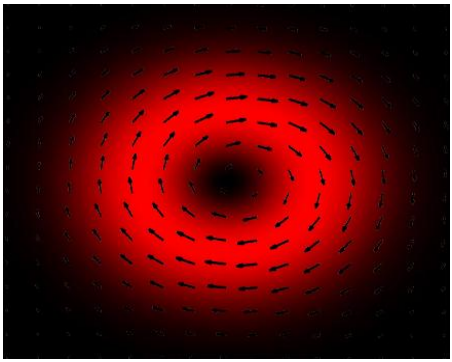

Figure 2.2. Intensity distribution of a LG_{01} mode and its corresponding transverse Poynting vector. Due to the rotational effect around the beam's axis, the presence of OV can be noticed. By changing the sign of the topological charge, the arrows point to the opposite direction.

This means that each photon of the beam, as predicted by Eq. (2.15), carries an orbital angular momentum of $l\hbar$. Moreover, the result of Eq. (2.22) entails that an optical vortex nested in a beam, carries an angular momentum per photon, in $\hbar$ units, equal to its topological charge. This result can also be applied to LG modes, allowing to assert that these beams carry an OAM per photon corresponding to their azimuth index *l*.
The rotational effects imposed by the presence of OAM can be hard to observe in typical vortex beams since they show circularly symmetric intensity distributions. However it is possible to obtain different field profiles without circular symmetry and it can be noticed that, during the propagation they rotate around their propagation axis.
In this situation, looking at Eq. (2.18), emerges that Laguerre – Gaussian beams form a set of orthogonal modes which are characterised by an intensity distribution which does not change with the free space propagation [20]. Therefore a generic paraxial field with a spatial distribution $u(r,\theta,z)$ can be written in terms of a modal decomposition of LG modes:

$$u(r,\theta,z)=\sum_{p=0}^{\infty}\sum_{l=-\infty}^{\infty}C_{pl}\psi_{p,l}^{LG}(r,\theta,z) \qquad \textbf{(2.23)}$$

where the expansion coefficients $C_{p,l}$ are determined by the projection relation

$$C_{p,l}=\int_0^{2\pi}\int_0^{\infty}u(r,\theta,0)\psi_{p,l}^{*}(r,\theta,0)\,r\,dr\,d\theta\,. \qquad \textbf{(2.24)}$$

The expansion of Eq. (2.23) is a powerful tool which allows to study analytically even fields carrying orbital angular momentum per photon with non-integer values. In fact, by substituting Eq. (2.23) in Eq. (2.15) and exploiting the orthonormality condition of such modes, after some algebra it can be found that the overall OAM is a weighted summation, performed over the radial and azimuthal indexes, of the angular momenta of the composing LG beams:

$$\ell = \sum_{p=0}^{\infty} \sum_{l=-\infty}^{\infty} l \left| C_{p,l} \right|^2 . \qquad \textbf{(2.25)}$$

In such a way OAM become a basis, hence beams with fractional values of OAM per photon may form, from a quantum-mechanical point of view, a N dimensional superposition state, which makes it appealing in quantum information [8].

2.4 Generation of optical vortices

There are many suitable techniques which allow to generate a screw phase dislocation, hence orbital angular momentum, in a light beam. Most of these methods resort to diffractive optical element, however they can be divided in categories following mainly two different philosophies: one produces the vortex beam by operating on cavity modes of the kind of Eq. (2.18), while the other aims to nest the phase dislocation by directly imprinting on the field the helical phase structure. Of course both of these techniques have their own flaws and advantages and their use depends on the application.

2.4.1 Generation of pure Laguerre – Gaussian modes

As mentioned above, LG beams are a solution of the paraxial wave equation for cylindrically symmetric reference system. As a matter of fact they can be obtained in laser resonators under specific conditions [28]. However, despite the pureness of such modes, since they occur spontaneously, is difficult to control the generation process thus to determine precisely the topological charge.

A more suitable way of generating LG modes, makes use of another kind of cavity modes, with rectangular symmetry and carrying zero orbital angular momentum, which are easier to obtain, the Hermite – Gaussian (HG) modes. Both Laguerre – Gaussian and Hermite – Gaussian form a

orthonormal basis, therefore a relation between the two bases can be found in order to transform a mode in another of the other kind [29]. For this sake mode converters based on astigmatic cylindrical lenses were proposed [30, 31]. These are made by a set of two cylindrical lenses separated by a fixed distance; an incident Hermite – Gaussian mode $HG_{n,m}$ (being n and m the indices corresponding to the number of horizontal and vertical nodal lines), rotated by 45° with respect to the optical axis of the lens, is transformed into a completely pure Laguerre – Gaussian mode whose indices are $l = n - m$ and $p = \min(n,m)$. Mode conversion was also obtained using an astigmatic fibre optic waveguide [32].

Higher order LG modes can be obtained with interference converters in which the output mode is produced by the superposition of an HG mode and an auxiliary beam.

It should be noted that these methods ensure a total mode conversion, thus the output beams are a real LG modes. However the proposed mode converters do not offer a compact solution and require a cumbersome experimental setup.

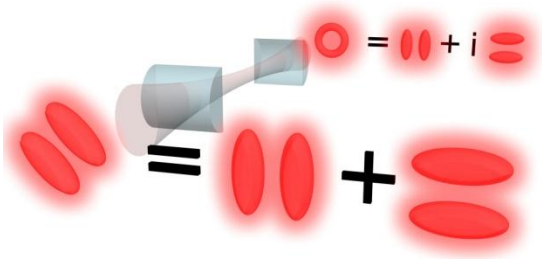

Figure 2.3. Cylindrical lenses based mode converter. The astigmatic lenses transform the HG modes in an LG one by introducing a π/2 phase difference between the modes of the superposition.

2.4.2 Screw dislocations imposed by phase device

Since OAM beams possess, as pointed out throughout this dissertation, a helical wave front, it is possible to nest the phase defect by imposing the

helical structure on the phase of the field. Therefore several diffractive optical devices were designed to accomplish this task.

One of the most common and simple technique is based on holograms imprinted with the interference pattern of a LG beam and a plane wave [33 – 35]. These holograms, commonly known as "fork holograms", show themselves as an edge dislocation enclosed in the lattice of the interference fringes which appears as a bifurcation. The number of "forks" in the fringe pattern is proportional to the topological charge – the index l – of the incident Laguerre – Gaussian beam.

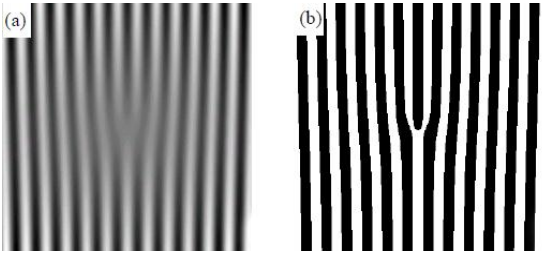

Figure 2.4. a) Interference pattern between a plane wave and a LG_{01} beam: the charge 1 OV produces a single bifurcation; b) holographic fork binary diffraction grating : when illuminated by a Gaussian beam it generates the recorded LG beam.

As a matter of fact when the hologram is illuminated by the reference field, a diffracted beam is generated with the phase fronts of the original LG mode. Notwithstanding it is possible to use phase holograms, a more efficient way is to employ amplitude holograms, i.e. binary diffraction gratings reproducing the interference pattern. On the output side of the grating, several diffraction orders are present, each of them carrying an optical vortex with a proportional topological charge.
Therefore the optical element acts as a transparency function of the kind

$$T(r)=\frac{1}{2}\left[1+\frac{r}{r_0}\sin\left(qx+m\theta\right)\right], \qquad \textbf{(2.26)}$$

where r_0 is a transmission parameter and q is the diffraction order. Since a simple binary diffraction grating can be used, the hologram can be easily calculated and generated by a computer (CGH) [36]. A more flexible and practical way of using the hologram technique relies on the spatial light modulators (SLM), liquid crystal based devices which can be configured in the shape of the fork grating. Differently from the transmission holograms, SLM is used as a reflective device, hence the incident beam is reflected from the grating into a set of diffraction harmonics. Furthermore SLM is completely real time driven by a computer, therefore it can be easily programmed in order to generate the desired OV beam. However, since SLM rely on liquid crystals, they have an intrinsic limit due to the power of the incident beam, which should not reach high values.
Because of the small dimensions and the tuning possibilities fork holograms offer an efficient solution to generate beams with orbital angular momentum, even though they do not produce pure Laguerre – Gaussian modes. Nonetheless they require precise alignment between the incident beam's axis and the central point of the grating, in order to imbed the singularity in the centre of the field distribution, thus to obtain, as will be shown later, an integer value of the OAM. Moreover it was pointed out that multiple diffraction orders are generated; among them the zero order beam – propagating along the same axis of the incident field and carrying zero orbital angular momentum – is present, hence it, together with the higher order harmonics, should be blocked so that the desired OV beam can be selected.

A simple, although less flexible diffractive optical element is the spiral phase plate (SPP), which is a transparent device which acts directly on the phase of the incident field imposing the helical structure of the wave front [37- 40]. The SPPs, as depicted in Fig. 2.5, have a staircase structure with a thickness which grows linearly from the base value h_0 to an upper value h_s. Therefore the optical path depends on the azimuth coordinate θ, thus imposing an azimuthal phase dependence.

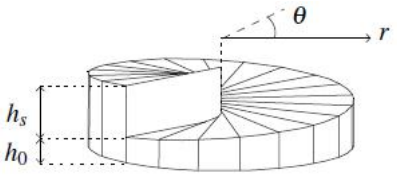

Figure 2.5. The spiral phase plate: the thickness of the device has a linear azimuthal dependence

These devices can be modelled as if they impose on the illuminating beam a transmission function acting only on the phase, which can be expressed as

$$T(r,\theta) = e^{iQ\theta} \tag{2.27}$$

being Q the topological charge, thus the OAM, imprinted on the beam. The physical features of the device are the step height h_s the refractive index n of the SPP and the background index n_0. Since the topological charge Q is bound to the optical path, it can be determined as

$$Q = h_s \frac{(n - n_0)}{\lambda}. \tag{2.28}$$

This means that, with a fixed SPP, the generated OV can be tuned both by changing the wavelength λ or by properly choosing the background medium, as in the experiments of Beijersbergen *et al.* poposed in ref. [31], where the spiral phase plate was immersed in a cell filled with an index matching fluid; in this situation a further degree of freedom was introduced by varying the background index through the control of the cell's temperature.

SPPs can be made of polymers and fabricated with micro machine moulding techniques [38] or can be produced with lithographic processes [41, 42].

However, since SPPs aim to impose the helical structure on the phase profile, there is a limit in realizing a true screw dislocation, that is a point phase singularity on the optical axis. As a matter of fact, in all the

fabrication techniques proposed there is a small area surrounding the optical axis, which cannot be controlled, hence introducing an height anomaly [38]. Nevertheless optical vortices of good quality can be generated. Ref. [37] shows that neither this devices can be considered as mode converters since they do not produce pure LG modes. Spiral phase plates are less tunable device with respect to the CGHs, especially if compared with SLM; however a certain degree of tuning can be obtained in polymer SPPs by changing the step height by means of a mechanical deformation [43]. The tuning restrictions of this device is given by the elastic limit of the plate material.

A completely different way of generating orbital angular momentum is the use of the so called Q – plates [44]. These are optical devices which are both anisotropic and inhomogeneous and convert spin angular momentum into OAM. This means that for a circularly polarized light beam, which carries SAM, incident on a Q – plate coupling of the SAM with OAM happens and a helical wavefront is generated. Of course the sign of the generated OAM depends on the input polarization direction. On the other hand, the absolute value of the OAM per photon is bound to the configuration of the Q – plate as shown in figure 2.6, or better by the local orientation of the optical axis in terms of two parameters.

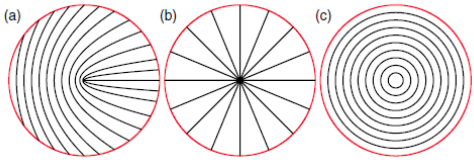

Figure 2.6. Different Q – plates configurations which generate OAM per photon equal to $l = \pm 1$ (a) and $l = \pm 2$ (b, c) depending on the direction of the polarization. Source Ref. [42].

These plates can be realized using both liquid crystals, polymers, or sub – wavelength gratings.

Part 2

Generation of OAM: linear techniques for creating optical vortices

Chapter 3

Helical reflection: optical vortices generated by a programmable spiral phase mirror

In the previous chapter several techniques were discussed for adding orbital angular momentum to a paraxial light beam. It was shown that all of them are valid methods notwithstanding they have their own advantages and drawbacks. In particular, looking at the devices previously described, it emerges that a common feature is undoubtely the lack of tunability in terns of topological charge, orbital angular momentum and operating wavelength, that is the difficulty of reaching a fast, easy and accurate control over the vortex charge, hence over the OAM of the output beam. Furthermore, all of the optical devices are macroscopic objects and tipically must be employed in experimental setup requiring a certain degree of alignment, therefore they are not thougt to operate as integrated optical elements.

The research path of this PhD, brought to study and design devices able to overcome the above limits, aiming both at the achievement of a good control of the OAM and at the integration features of OV generation devices.

This chapter and the following one will introduce two different techniques suitable for creating helical beams. The former is an adaptive segmented mirror controlled by electrcally driven actuators capable to configure itself in order to obtain a perfect tunability of the topological charge and OAM imposed on an incident beam by operating on its phase profile.

The second proposed device, which will be discussed in chapter 4, takes advantage of plasmonic interactions for generating a beam with OAM, starting from a circularly polarized light field; this allows the creation of OVs at the nanoscale, opening the way for integrated singular optics.

3.1 Programmable spiral phase mirrors

It was shown before that among all the techniques suitable to obtain OAM, the most commonly used are undoubtely the fork hologram (or its tunable analogous SLM) and the spiral phase plate. However both of them are affected by a common defect, that is the reduced possibility of a fast reconfiguration which allows to change in real time the properties of the output OV. Moreover SPPs are tightly bound to the wavelength of the incident field, because they operate on the optical path; on the other hand CGHs produce, in addition to the desired one, several diffraction orders which should be suppressed. Other than this limitation, SLMs can not sustain beams with excessive power, since they are made of liquid crystals. It was mentioned before that attempts to produce adjustable spiral phase plate have been undertaken by Rotschild *et al.* in Ref. [43]. They produced a SPP made of a plexiglass plate where is made a cut which goes from an edge to the center of the structure. The plate is then mounted on a rigid frame and one side of the cut is strained by means of screws: this technique allows to change the optical path, hence the SPP can be adapted to different wavelengths and, with fixed λ, can produce multiple values of the topological charge. Although this is a simple method to tune OAM it shows serious limits due to the elastic limit of the material which leads to the breakage of the device for too high values of the topological charge. Ref. [43] reports that this effect can take place even for Q greater than 3.

Alternative techniques for imprinting helical wavefronts take advantage of reflection based devices instead of transmission ones. This is the case of helical mirrors which operate on the incident beam by introducing a suitable phase difference with an azimuth dependence. As a matter of fact the mirror surface can be designed in order to vary linearly with the azimuth

coordinate, thus introducing an height difference between the extremes angular values.
Following this simple principle the helical surface of the device can be actively deformed by changing its pitch, hence making it an adaptive helical mirror (AHM).
Ghai *et al.* [46,47] designed and produced an AHM by using a technique similar to the one presented in Ref. [43]. In fact they made a radial cut, which goes from the edge to the center, onto a circular flat metallic mirror. Then a tubular piezoelectric transducer (PZT) deforms the mirror along its optical axis and stretches the edges of the cut in the shape of a helix. A voltage applied on the tubular PZT is responsible of its deformation and makes it elongate or contract along its length. This allows to control exactly the total helical deformation of the above mounted mirror which changes the helix pitch linearly with the applied voltage.

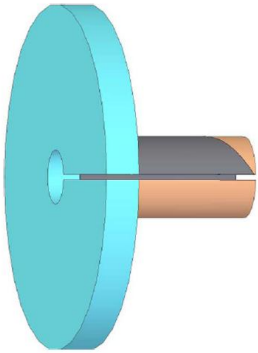

Figure 3.1. Continuous adaptive helical mirror. A radially cut flat mirror is mounted on a tubular PZT. The helical deformation is directly driven by the applied voltage.

In this way the AHM, differently from the common spiral phase plates, has a continuous helical surface which entails a better quality of the generated optical vortices. However the continuous nature of the helical mirror surface at issue entails an intrinsic limit to the programmability of the topological charge. As a matter of fact there is a maximum height

difference between the edges of the cut, corresponding to the breaking point of the mirror, which does not allow to exceed the absolute value of Q = 4. Moreover other issues concern the generation of OVs with opposite topological charge because of the depolarization limits of the transducer which may be depolarized if an excessive reverse voltage is applied on it.

More flexible solutions were proposed introducing segmented mirrors as OV generators [48]. Tyson *et al.* report the generation of optical vortices by reflection from a segmented mirror made of hexagonal cells. These segments were driven by actuators in order to configure the mirror as a spiralling surface. This system allows to tune the topological charge in the mechanical limits of the actuators which, in this situation do not show depolarization problems. Generation of OVs up to charge 5 was reported together with the possibility of producing vortices with fractional OAMs.

However, since helical wavefronts are purely azimuthal objects, the geometry proposed in Ref. [48] may not be optimal for the generation of OVs. In fact the hexagonal cells must be controlled both in the radial and azimuthal direction requiring a more complex control of the actuators. Furthermore the hexagonal geometry introduces a certain degree of approximation in reproducing the helical structure, especially in terms of the central anomaly.

From what showed above it can be understood that the philosophy of segmented mirrors may be a good solution to obtain a tunable topological charge device capable to operate on multiple wavelengths and which can be rapidly reprogrammed.

In this research work it was found a more suitable geometry of deformable mirror where the segmentation is made along the azimuth coordinate, hence resulting in a series of reflecting “slices” whose height can be driven independently by actuators. Since its main feature is to generate helical wavefronts, this device can be addressed as a programmable spiral phase mirror (SPM). The azimuthal steps can be thus configured both as helical ramps (single or multiple), then generating OAM, or as arbitrary azimuthally dependent profiles which can shape the beam’s intensity distribution in order to perform a sort of spatial encoding.

In this dissertation the design of the device is proposed, together with the corresponding numerical simulations which take into account both the

generation of OAM and the beam shaping configurations. Since the device is currently being fabricated, a possible experimental setup is also presented.
Finally it should be noted that there is a patent pending and a journal paper to be published.

3.2 Design of the spiral phase mirror

As pointed out before the issued device is composed by a number N of azimuthally distributed segments of metallic mirror which can be displaced independently from their original position by actuators, i.e. piezoelectric transducers. The azimuthal slices may be obtained by deposition of a metal layer which can be radially cut with a period of $2\pi/N$. Figure 1 shows an outline of the structure and one of its possible configurations.

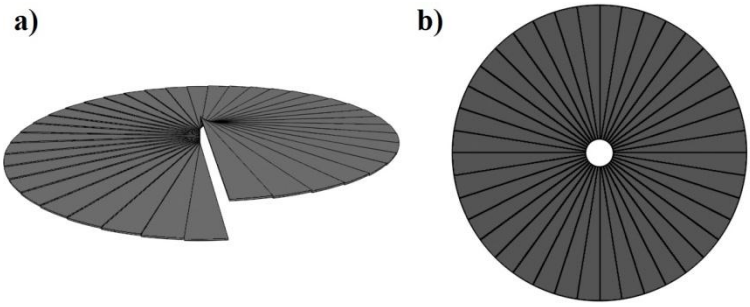

Figure 3.2. Schematic representation of the azimuthally segmented helical mirror composed by N = 40 steps. a) Perspective view: the steps are displaced in helical configuration; b) top view.

Looking at Fig. 1 it can be noticed that a central hole is present in the mirror. This is intrinsically bound to the fabrication process which cannot produce perfect wedges. However if the radial dimensions of the programmable SPM are large enough, the effect of the central hole can be neglected. Since the proposed device is intended to be a macroscopic object, the above conditions are always true.

The spiral phase mirror can be modelled similarly to SPP by treating it as a simple reflection function affecting only the phase of the field: we thus assume that, when an incident beam is reflected by the mirror, its disturbance results multiplied by a linearly azimuthally dependent phase function hence the amplitude remains unaffected. It was pointed out that the mirror' steps undergo to a displacement from their original position which deforms the mirror surface along the *z* axis, that is the propagation axis of the incident beam. Since each slice corresponds to a fixed discrete value of the azimuth coordinate, when the mirror is deformed, at each azimuth angle is associated a height displacement Δz. Therefore the mirror surface can be considered as if it undergoes to a displacement function $\Delta z(\theta)$ which is responsible of the phase change experienced by the reflected field.

If a paraxial light beam with amplitude $E(r,\theta,z)$ impinges on the mirror with normal incidence, the field E_R resulting from the reflection experiences an additional propagation distance which depends on the angular coordinate as follows:

$$E_R(r,\theta,z) = E(r,\theta,z)e^{ik\Delta z(\theta)}, \qquad \textbf{(3.1)}$$

being *k* the beam's propagation constant. Looking at Eq. (3.1) it is evident that the programmable SPM can be configured in order to assume an arbitrary azimuthally dependent height displacement.

If an optical vortex has to be generated, as it is known, a helical phase distribution is required; this means that, as happens for the spiral phase plates, the mirror' steps should be arranged in a staircase fashion, spiralling along the optical axis. The position of the segments composing the mirror thus grows linearly with the angle θ, creating the desired helical path.

It can be helpful to remind that an OV beam is characterized by a phase distribution which goes as $\exp[iQ\theta]$, hence, in order to obtain a vortex of topological charge Q, the phase change along θ should be Q times 2π.

In this situation a simple formula describing the mirror profile Δz, which relates the height of each step, the operating wavelength λ and the topological charge Q, can be derived by comparing the phase term of Eq.

(3.1) with the expression of the helical wavefront. Therefore, equalling the terms

$$ik\Delta z(\theta) = iQ\theta, \tag{3.2}$$

it can be found that the overall displacement is

$$\Delta z(\theta) = \lambda Q \frac{\theta}{2\pi}, \tag{3.3}$$

which can be clearly identified as a helical ramp. Since the steps are distributed along θ, this direction can be made discrete and, by associating each step with an increasing integer index dependent on the θ coordinate, Eq. (3.3) can be easily written in terms of the step index j which ranges from 1 to N:

$$\Delta z_j = \frac{(j-1)\lambda Q}{N} \tag{3.4}$$

Of course this implies an approximation of the spiral ramp, since there is a jump corresponding to the angle 2π (or 0) thus the displacement never reaches the value λQ. However the larger is the steps number N, the better is the spiral distribution, because the discrete angle asymptotically tends to assume the value 2π at the jump coordinate.

The helical mirror's profiles of Eqs. (3.3) and (3.4) may result difficult to obtain when higher topological charges are considered, thus limiting the operability of the device, as happened for the adaptive helical mirror of Ref. [46, 47]. As a matter of fact, a high value of the topological charge entails a large amount of displacement which cannot exceeds the maximum elongation of the actuators; furthermore large height differences result in longer re-configuration times, since the actuators would take more time to change their state of such amounts.

This problem can be overcome, provided that the mirror is composed by a suitable number N of segments [50], if the SPM displacement function is programmed as a saw – tooth profile with a number of periods equal to the desired topological charge. In this way, each ramp imprints an azimuthally

dependent phase shift of 2π, reducing drastically the maximum displacement of the steps, therefore eliminating the problems associated with common adjustable helical devices. This allows to reduce the situation to the unitary topological charge case. An example of multiple ramps configuration is depicted in Fig. 2 where a perspective view of the SPM programmed to generate a topological charge Q = 5: the displacement of each ramp introduces a phase difference of 2π.

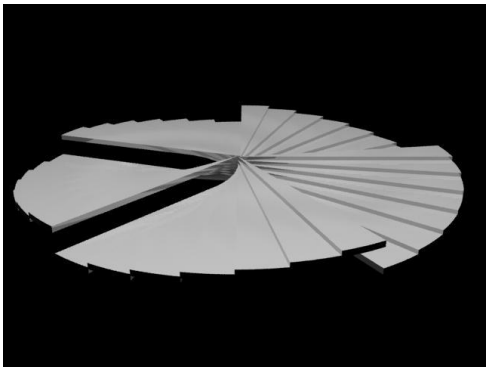

Figure 3.3. Programmable spiral phase mirror configured in the saw – tooth profile with Q = 5; the steps are arranged in five linear ramps along the azimuth coordinate, introducing an equal number of 2π phase shifts.

It was mentioned that the adaptive helical mirror proposed by Ghai *et al.* [47] suffered of problems regarding the inversion of the sign of topological charge because of hysteresis issues of the piezoelectric actuator. The programmable SPM overtakes these limits; in fact, in order to obtain a topological charge of opposite sign, it is sufficient to invert the direction of the ramps. In terms of the displacement function this means that the symmetric Δz function should be considered.

Of course the independence of the segments allows to program the mirror with an arbitrary azimuthal height function, a thing that entails the possibility of generating different field' space profiles. For example, by grouping steps together, it is possible to reduce the discretization of the helical ramp, going below the minimum number of steps suitable to represent a fixed topological charge. As a matter of fact, if the slices are

less than what was predicted in reference [50] the OAM per photon decreases from its starting value which, it is reminded, equals the topological charge. Therefore a further degree of tunability of the orbital angular momentum is added.
Other examples of configurations see the height profile arranged as a square, triangular, or trapezoidal wave profile: it is clear that all of these are techniques capable to tune the angular momentum and to configure the intensity distribution, entailing the possibility to introduce a system of spatial encoding.

3.3 Numerical simulations

In order to estimate the features of the designed mirror, numerical simulations were performed which allowed to observe the field's amplitude and phase profiles produced by the device and the corresponding orbital angular momentum. For this sake a simplistic but efficient and accurate paraxial model was considered so that the following setup can be represented. Supposing the SPM on the $z = 0$ plane, the profile of the incident field was considered to accumulate an optical path Δz, corresponding to the displacement function, and dependent on the azimuth coordinate θ. The so – obtained disturbance is then let propagate in free space and by passing through a lens of focal length f placed at a distance equal to f the far field pattern is observed. Finally, since it is a propagation constant, the OAM per photon is evaluated

By letting a Gaussian beam hit the mirror, it acquires the phase dependence expressed by Eq. (3.3). If we suppose that the incident beam hits the mirror in its waist, the diffracted beam on the back focal plane of the lens will be proportional to the Fourier transform of the reflected beam, that is the incident profile times the phase function $\exp[i\Delta z(\theta)]$ [27]:

$$E_R(x,y,z) \propto \iint e^{-\frac{x^2+y^2}{w^2}} e^{ik\Delta z(\xi,\eta)} e^{-i\frac{k}{f}(\xi x+\eta y)} d\xi d\eta, \qquad \textbf{(3.5)}$$

where ξ and η are the transverse Cartesian coordinates in the plane of the mirror (*z = 0*) and *w* is the spot size of the incident Gaussian beam. Note in Eq. (3.5) the azimuth coordinate was written in terms of its Cartesian component so that the field expression can easily be handled by the simulation.

On the Fourier plane we therefore calculate the OAM per photon of the diffracted field, in ħ units, as the ratio of the total orbital angular momentum and the field's energy as reported in chapter 2. For simplicity the expression used in the evaluation of the OAM per photon is reported, written for Cartesian coordinates, as follows:

$$\ell = -i \frac{\iint u^*(x,y)\left[x\frac{\partial}{\partial y}u(x,y) - y\frac{\partial}{\partial x}u(x,y)\right]dxdy}{\iint \left|u(x,y)\right|^2 dxdy}. \quad \textbf{(3.6)}$$

Calculating the OAM through Eq. (3.6) allows to generate a rectangular numerical mesh over which the field distribution $u(x,y)$ is defined.

For this purpose we considered a mirror composed by N = 360 steps, so that a high discretization degree is achieved; in this way large topological charges can be tested and height profiles with different complexities may accurately be reproduced. It should be noted that a high discretized azimuthal mesh requires an even larger number of spatial samples in the *x* and *y* direction in order to conserve the slice structure near the central point of the staircase, i.e. the singularity point, where the azimuthal steps become very small. If this condition is not satisfied defects appear in the reflected far field profile, producing effects similar to the anomalies of the common spiral phase plates. This may result more evident particularly when the circular symmetry is broken as happens for non-integer OAMs or when complex displacement functions are programmed.

Within this research work several SPM's configurations were tested by holding fixed the topological charge and varying the number of the composing steps and by modulating the height profile Δ*z*. Since the considered mirror possesses an azimuthal segmentation of 1 degree, the

simulations were performed by grouping multiple slices, so that SPMs with less steps could be represented.
The following numerical simulations were carried out by taking into account an operating wavelength of 830 nm. Furthermore for every considered situation are reported both the configuration of the spiral phase mirror, its corresponding field's intensity and phase distributions observed in the far field region. Studied profiles include the simplest helical profile, the saw-tooth and the triangular displacement functions, for different values of the ramp' slope.

Helical profile
In order to investigate the basic configuration of the SPM, the simplest case of a topological charge Q = 1 has been chosen and, to verify the behaviour of the azimuthal discretization, the N steps were subdivided into groups containing segments with the same displacement; in such a way larger sectors can arranged to form the well-known spiral distribution of Fig 3.2. Figure 3.4 reports the phase profiles imposed by the mirror on the incident field, together with the diffracted field's intensity for different numbers of the macro sectors N' composing the helical staircase.

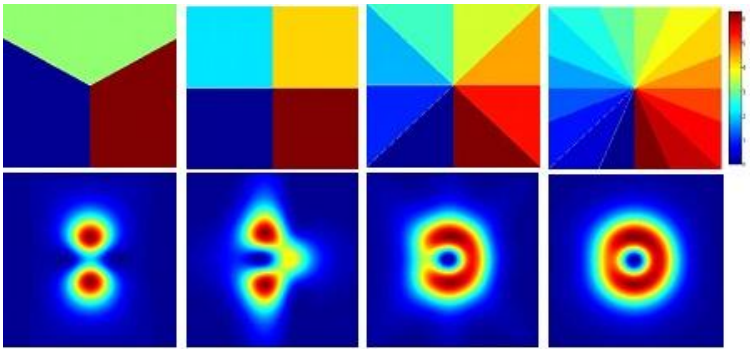

Figure 3.4. Phase distribution imposed by an helical mirror programmed for generating a topological charge Q = 1 (upper row) and the corresponding far field intensities of the reflected field (bottom row) for growing numbers of steps: a) N' = 3; b) N' = 4; c) N' = 8; d) N' = 16.

It can be noticed that for higher step values (N' >16) an intensity distribution similar to the LG_{01} mode appears while, on the contrary, when the slices are fewer the helical behaviour is lost. Similarly the orbital angular momentum grows with the steps number approaching its final value, thus equalling the topological charge.

Particular attention should be lent to the possibility of tuning the wavelength.

As a matter of fact Eq. (3.3) predicts that the vortex is generated when the overall optical path equals the wavelength. Therefore a helical staircase of fixed pitch produces the programmed OV only at a certain wavelength. This is the main problem related to most of the OV devices discussed above. Clearly the SPM overcomes this issue, allowing to adjust the spiral's pitch so that the same topological charge can be obtained even when the operating wavelength is changed. Moreover, since the spiral phase mirror is made of metal coated slices, a flat spectral response can be considered over a wide range of wavelengths in terms of both reflectivity and absorption. This entails that index matching conditions imposed by devices such as spiral phase plates result no more necessary. Furthermore its metallic features reduces the power constrains; in fact the above discussed devices are often made of polymers (SPPs) or liquid crystals (SLM), thus the power of the incident beam should not overstate the melting threshold of the material. On the other hand metal coatings withstand major levels of power, hence optical vortices can be easily generated even in more intense beams.

Of course this remains true when different height profiles are considered, making the SPM an optical vortex generators flexible in terms of topological charge and operating wavelength.

Saw tooth profile

It was pointed out before that, in order to reduce the problems related to an excessive step displacement arising when high topological charge are programmed, non-unitary helical wave-fronts are better obtained by assembling Q linear azimuthal 2π phase ramps instead of a single staircase with a $2\pi Q$ displacement. In this situation the maximum height difference should be fixed at $\Delta z = \lambda$, or multiples of the incident wavelength (always

reminding to not reach high values), for each ramp; therefore the unitary helical ramp so created can be replicated Q times in the whole azimuth distribution. Of course the simplest and most efficient configurations is obtained, provided that an enough coarse segmentation is defined, when unitary ramps are considered. This corresponds, along the coordinate θ, to a saw tooth profile, where the number of periods corresponds to the overall topological charge and the slope of the ramp is proportional to Q.

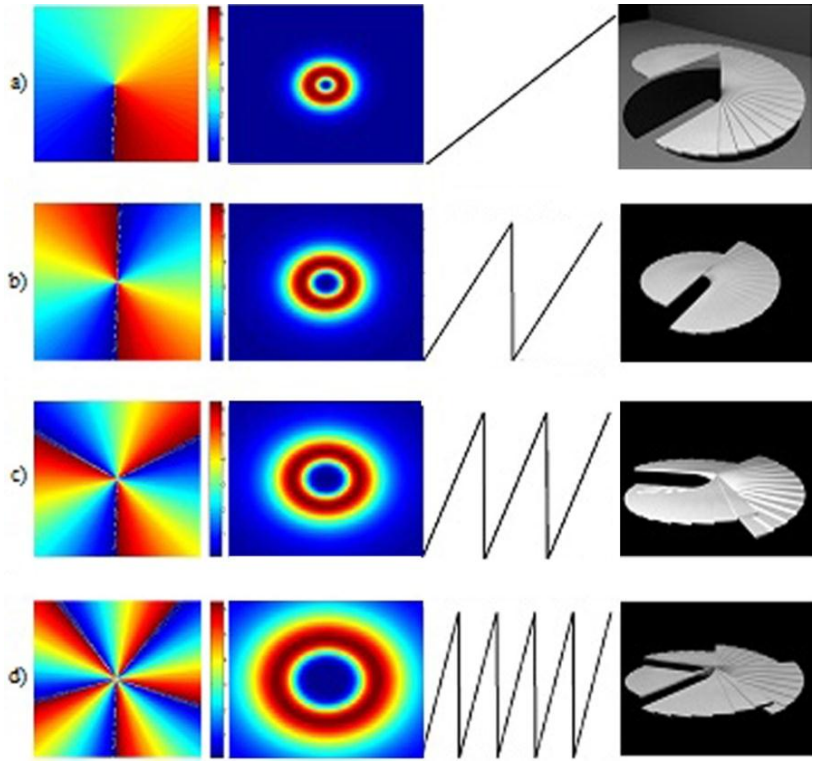

Figure 3.5. Helical mirror configured as a saw tooth profile; phase profiles are reported (first column) together with the corresponding diffracted intensities (second column), the displacement Δz as a function of the azimuth coordinate θ (third column and the perspective view of the distribution of the mirror' steps (fourth column). a) Q = 1, OAM =1; b) Q = 2, OAM = 2; c) Q = 3, OAM = 3; d) Q = 5; OAM = 5.

Figure 3.5 reports the mirror's displacement profiles and their corresponding generated intensities and phases calculated for values of the topological charge ranging from 1 to 5. Equation (3.6) was used to numerically evaluate the angular momentum of the fields considered and was found that it is always verified that $\ell = Q$. Obviously the condition on the number of steps for discretizing the helical surface remains valid even though should be applied to each composing ramp.

Triangular wave profile

In this case the slices are arranged in a triangular wave, i.e. the displacement grows linearly (positive slope) until it reaches a phase shift of 2π and then decreases to zero with a negative slope coefficient m. Therefore, with respect with the saw tooth case, here the number of ramps is doubled.

In the simulations the positive ramp' slope was held fixed and the maximum height difference was chosen in order to obtain a 2π phase shift. Then, by changing the steepness of the negative ramp from $m = 1$, which corresponds to a symmetric triangular wave, to higher values, the analysis of the intensity distribution and its corresponding OAM was carried out. In other terms, considering the saw tooth profile discussed in the previous section, it can be noticed that it corresponds to the particular case of a triangular wave whose negative ramp has infinite steepness. Therefore in the performed numerical simulations, starting from a saw tooth profile with fixed topological charge Q, the negative slope has been reduced until it reaches a symmetric distribution along the azimuth coordinate. This means that, while the slope becomes less steep, the number of periods decreases, as can be clearly seen from Fig. 3.6.

As the symmetric case is approached the phase jumps which separate the ramps are gradually removed. Therefore the positive phase accumulated in a fixed azimuthal arc begins to be compensated by the descending ramp. The complete compensation happens when the ramps have the same slope, entailing a zero net topological charge, hence a zero orbital angular momentum. A further reduction of the negative slope joined with an increasing positive ramp, leads to an inversion of the vortex charge.

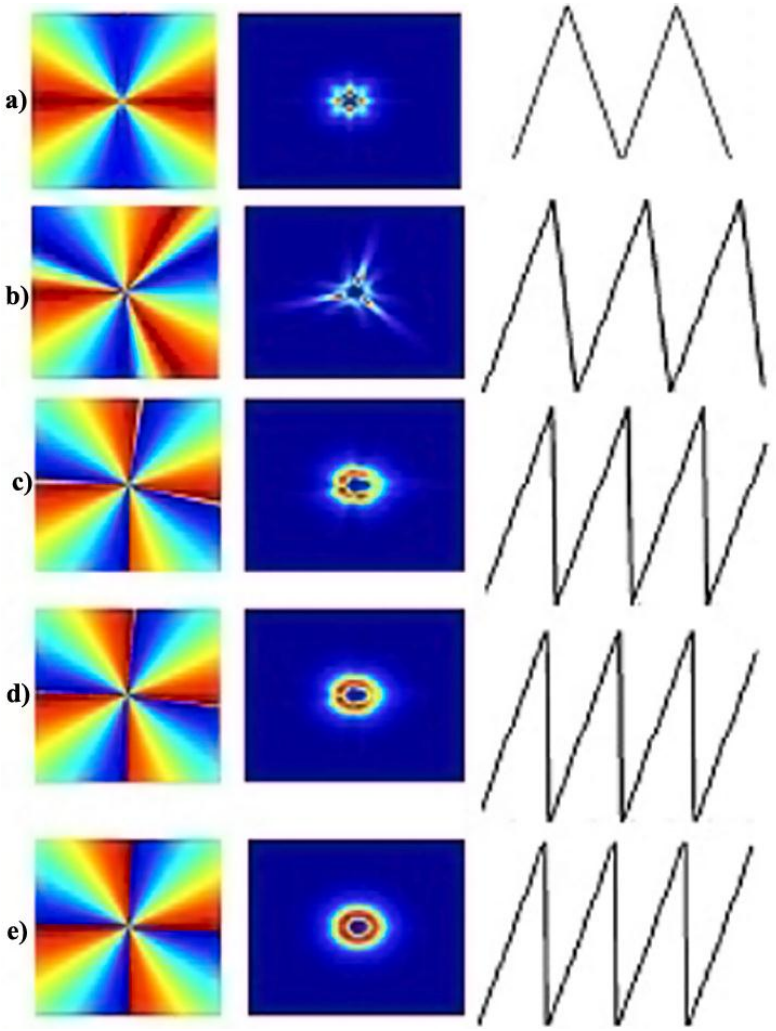

Figure 3.6. Triangular wave profile with different slope coefficients *m*; the maximum topological charge, i.e. the saw tooth profile, is Q = 4. From left to right: imprinted phase profile, far field intensity of the reflected beam, displacement function $\Delta z(\theta)$. a) $m = 1$, OAM = 0; b) $m = 3$, OAM = 0.5; c) $m = 20$, OAM = 2.23; d) $m = 100$, OAM = 4.

In all the intermediate cases between the saw tooth and symmetric triangular wave, the resulting OAM is proportional to the net difference over the azimuth circumference of the positive and negative phase contributions.
In figure 3.6 are again depicted the phase and intensity profiles of the reflected beams and the displacement function for increasing slopes (modulus) of the descending ramps.
The steps arrangement was omitted since it is analogous to what was showed in Fig. (3.5). It can be observed that, the steeper is the slope, the higher is the OAM, until it reaches its maximum value equal to the number of periods of the saw tooth situation.
Looking at Fig. (3.6) it clearly emerges that these configurations can be thus used in order to perform a tuning of the orbital angular momentum which can be simply controlled by the slopes of the azimuthal profile. Therefore, keeping fixed the maximum topological charge, it is possible to tune the OAM by adjusting the negative ramp' slope.
It is clear that the capability of displacing the mirror' slices independently allows to use the spiral programmable mirror for manifold applications; several configurations of the height function can be arranged, depending on the desired target which may be the generation of an optical vortex with a chosen topological charge, or the adjustment of the OAM.
Regarding the latter application, another tuning procedure can be performed. As a matter of fact it is possible to hold fixed the number of ramps, that is the number of periods, and varying both the positive and negative slopes. This possibility is illustrated in Fig. 3.7 where, as usually, the phase, intensity and displacement profiles are showed in the case of a triangular wave made of four periods.
As happened in the previous situation, the steps' configuration spaces from the saw tooth to the symmetric wave distribution.
The difference with the above case is that now, both the ramps change their slope independently in order to keep unaltered the number of periods. However, also in this case the increasing slope corresponds to an increasing OAM which tends to assume the integer value Q when the slope coefficient *m* becomes infinite. All the techniques discussed so far focus on the tuning of the angular momentum or of the topological charge.

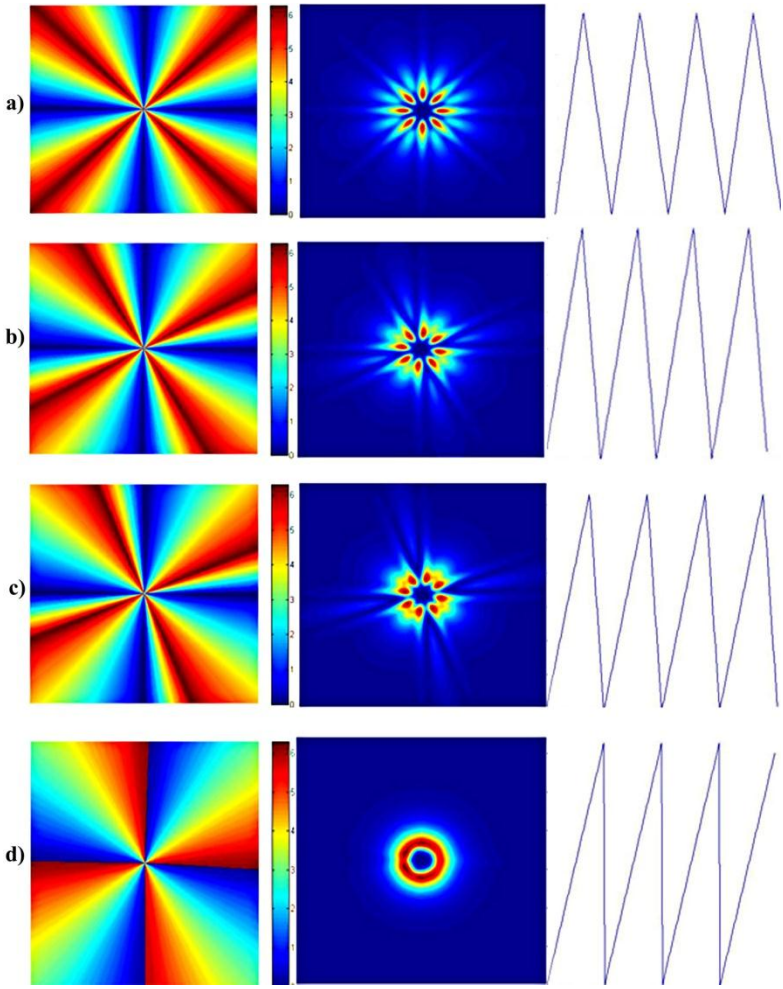

Figure 3.7. Triangular wave profile with different slopes and fixed number of periods L. From left to right: imprinted phase profile, far field intensity of the reflected beam, azimuthal displacement function $\Delta z(\theta)$. The OAM per photon grows as the descending ramp increases, in absolute value, its slope coefficient m. a) $m = 1$, OAM = 0; b) $m = 2$, OAM = 0.7; c) $m = 3$, OAM = 1.3; d) $m = 128$, OAM = 4.

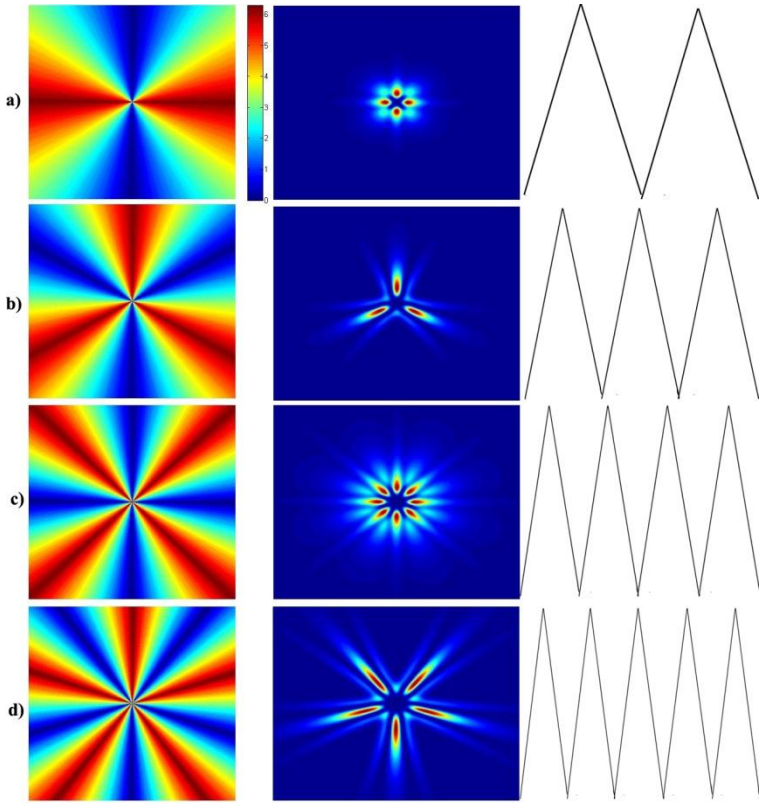

Figure 3.8. Phase (left column), far field intensity (centre column) of the field reflected by the spiral phase mirror with symmetric triangular wave displacement function (right column). The symmetric configuration entails a zero OAM whichever is the number of periods L. The far field pattern depends on the parity of the periods: even periods generated a doubled number intensity lobes with respect to odd number of periods.

In fact the attention can be moved from the OAM, which is held constant, to the spatial distribution, so that a programmable beam shaping technique is introduced which may put the basis for a kind of spatial encoding.

Nevertheless the flexibility of the SPM may be exploited to generate arbitrary transverse spatial field's distributions with azimuthal symmetry.

As a matter of fact, if the OAM is chosen to be, for example, zero, hence, as discussed above, arranging the segments of the SPM in positive and negative ramps with symmetric slopes, the spatial profile may be modified by changing the number of periods of the triangular wave.
In this situation a radial symmetric pattern can be generated; it is characterized by a number of intensity lobes proportional to the number of period L.
Figure 3.8 represents the intensity distributions corresponding to the phase profiles imprinted by the spiral phase mirror programmed with a symmetric triangular wave displacement function.
It can be observed that the diffracted field's transverse spatial profile is different, depending on the parity of the number of periods L: typical reflected intensity patterns can be associated univocally to even and odd values of L.
Looking at Fig. 3.8 it can be clearly observed that an even number of periods corresponds to intensity distributions made of 2L lobes, while fields reflected by a mirror whose steps are arranged in an odd number of periods, show L intensity maxima in the far field region. Therefore it is evident that both the number of periods L and its parity can be considered as parameters capable of controlling with an excellent degree of accuracy the field' spatial distribution in order, for example, to achieve a sort of spatial encoding suitable for optical communications.
It should be noted that what was discussed until now are only some possible configurations that can be programmed on the SPM; as a matter of fact the slices of the mirror can be arranged in many other fashions which allow to control both the topological charge, thus the orbital angular momentum, and the spatial profile.
Since the reflection by the mirror affects, as stated in the previous sections, the incident beam only for a phase factor, the considered mathematical model allows to evaluate analytically simple displacement profiles and remains a useful and efficient numerical tool suitable to investigate more complex height functions because of the simple integrability of Eqs (3.5) and (3.6).

3.4 Experimental setup

Differently from most of optical vortex generators like the already cited mode converters, fork holograms and spiral phase plate, which operate on the phase of a transmitted beam, the SPM works by imposing a helical phase dependence on a reflected beam, similarly to what happens using spatial light modulators. Therefore a suitable experimental setup should be employed in order to properly collect the helical beam reflected by the mirror.

A possible solution is the one sketched in Fig. 3.9, where a laser beam at the operating wavelength, consistent with the programmed displacement function, passes through a 45 degrees beam splitter cube and hits the mirror, which is controlled by a computer. A software allows to program the desired height profile, assigning a specified displacement value to each slice.

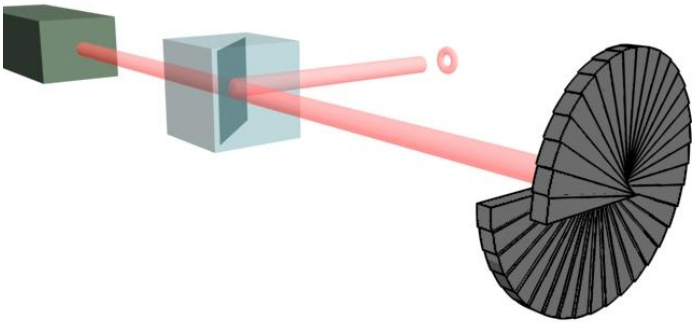

Figure 3.9. Experimental setup for the SPM. The incident beam is reflected by the mirror and sent back to the beam splitter cube. The helical shaped beam hits again the 45 degrees beam splitter and is partially reflected with a propagation direction perpendicular to the original. The beam's intensity is then collected.

This is then translated in an electrical signal which is transmitted to the actuators which effectively displace the segments of the mirror.
The helical beam produced by the reflection on the spiral phase mirror propagates in the backward direction until it reaches the beam splitter cube. Here part of the beam is transmitted and part is reflected at an angle of 90 degrees, allowing an easy collection of the generated optical vortex which can be sent to the rest of the setup.

In the previous sections the spiral phase mirror (SPM) was presented as an optical device capable of generating optical vortices. This device, by means of a series of independent electrically driven slices disposed in the azimuth direction, is suitable to adjust and control OVs' features like topological charge and orbital angular momentum, and can be adapted for a wide range of operating wavelengths.
It was shown that the possibility of controlling each azimuthal step independently leads to an easier tuning of the optical vortex and, since a smaller displacement is required when the device is programmed to reproduce a saw tooth height profile, it allows to obtain higher values of the topological charge with respect to former adjustable devices and faster reconfiguration times.
Moreover the sign of the OV can be reversed by simply inverting the direction, or the slope, of the ramps.
Furthermore arbitrary step displacement functions can be programmed; this means that it is possible to perform a continuous tuning of the OAM or, on the other hand, to produce well controlled transverse spatial field distributions which can be employed for spatial encoding.

Chapter 4

Surface plasmons assisted optical vortex generation: the Plasmonic Spiral Phase Plate

One of the optical vortex generation techniques adopted the philosophy of converting the spin component of the angular momentum (SAM) into the orbital one through a liquid crystal based optical device, the q-plate[44]. Throughout this dissertation it was pointed out that liquid crystal devices are limited in terms of input power and cannot be fabricated by integration processes. Both this limits can be overcome by moving to the nanoscale optics. This means that light would interact with matter with sub-wavelength features. Therefore a new field of optics comes into play: plasmonics. Plasmons are electromagnetic waves coupled with collective oscillations of electrons in metals and allow the control of electomagnetic fields on a subwavelength scale.

The research on plasmonics has reached very advanced levels that many plasmon-based devices were proposed and built. Many of these devices exploit the phenomenon of extraordinary transmission studied by Ebbesen *et al.* [52] to manipulate the electromagnetic field such as waveguides, sub-wavelength diffraction gratings [61], nanoslits, nanoholes [52, 53] and nanoantennas [54, 55]. The capability of controlling the sub-wavelength interactions allowed to design more complex devices suitable for beam shaping as plasmonic lenses [56, 57]. Even singular optics took advantage

of plasmonics for creating vortex devices [58]; furthermore OV measurement techniques were proposed [59].
In this chapter the design of an optical vortex plasmon based generator is presented. Differently from the plasmonic vortex lens (PVL) proposed by Kim *et al.*, which generates a vortex – a point phase singularity – in the surface plasmon field, the issued device produces an OV beam propagating in the free space and carrying OAM.
This device, which can be called Plasmonic Spiral Phase Plate (PSPP), operates a conversion between spin and orbital angular momentum when is illuminated by a circularly polarized beam (thus carrying SAM); under these conditions plasmonics interactions take place and a field with OAM is radiated.

4.1 The Plasmonic Spiral Phase Plate: general description

Recalling what was said in paragraph 2.3 about the energy circulation in helical beams, it can be remarked that OAM is related to a tangential component, in the transverse plane, of the Poynting vector. As a matter of fact an electromagnetic field whose wave-fronts are helicoids is associated with a linear momentum vector locally tilted from the propagation direction of an angle α, in order to be always orthogonal to the wave-front' surface. This implies that the Poynting vector twists around the main propagation axis, thus resulting in a vortex-kind behaviour.
The main idea behind the PSPP is to reproduce this phenomenon by means of an array of light sources equally spaced along a circumference, each of them radiating with a constant tilt angle α with respect to the propagation direction z as sketched in Fig. 4.1. The fields so generated compose, giving rise to an overall field distribution where the energy circulates around the z axis, thus creating an optical vortex.
As mentioned in the previous paragraph, light sources can be considered as plasmonic antennas, illuminated by a field with suitable polarization, so that surface plasmons are triggered and the directional emission takes place. In the next sections the details and the structure of these sort of nano

antennas will be discussed; however a general description of the device is given in Fig. 4.2 where a perspective view of the PSPP is outlined.

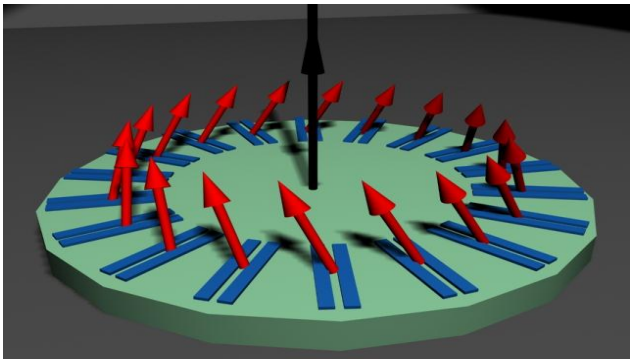

Figure 4.1. Outline of the working principle of a plasmonic spiral phase plate. An azimuthal array of light sources radiate a light field locally tilted of a constant angle with respect to the propagation axis *z*. The resulting Poynting vector rotates around the propagation direction.

The plasmonic plate is made of a metallic structure where deep slits are radially etched. In order to exploit plasmonic interactions, the slits' width is far below the operating wavelength; furthermore the tilt in the emission pattern is obtained by unbalancing the output edges of the slits. In practice for each slit, the input plane, i.e. the plane illuminated by the incident beam, sees aligned borders, while on the output face the borders of the aperture are misaligned so that one side is higher than the remaining. In this way along the azimuth coordinate the height of the output surface can be described by a square profile.

An incident circularly polarized field, propagating from the bottom side of Fig. 4.2, scattered by the edges causes the excitation of surface plasmon (SP) modes; these surface waves propagate along the air-metal interface, penetrating inside the sub-wavelength aperture and causing the extraordinary transmission. The SPs on the walls of each slit are guided along the thickness of the metal plate until they reach the output face (upper side of Fig. 4.2) where they couple again with air, being radiated by the structure. Since there will be an optical path difference between the SP on

the short side and the SP on the long side, an interference interaction occurs and the phase front will result tilted with respect to the *z* axis. Therefore the Poynting vector, which must keep the orthogonality with respect to the wave-front, will also be tilted of the same amount.

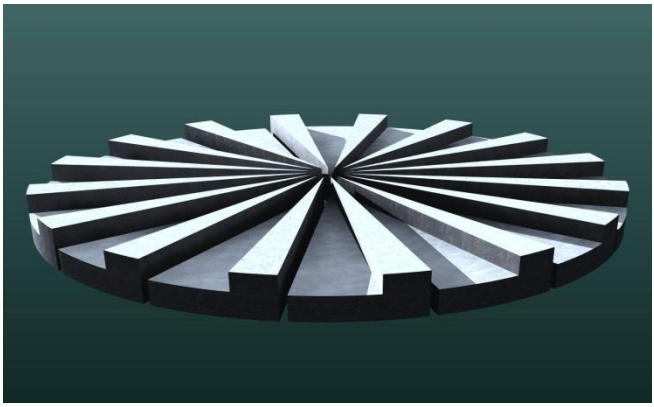

Figure 4.2. Perspective view of the PSPP. The azimuthal unbalanced apertures acts as an array of light sources with tilted emission pattern. The incident field illuminates the device from the bottom side.

4.2 Theoretical model

It was stated that the issued device aims to generate orbital angular momentum from a circularly polarized (CP) incident beam. This happens by conveniently placing a discrete number N of electromagnetic field' sources, each of them producing a skew Poynting vector, hence with a transverse component directed along the azimuth coordinate. The fields generated from these emitters compose as they diffract, originating a combined field whose linear momentum vector spirals about the propagation axis *z*; therefore a significant tangential component will be present. It is indeed this tangential component which entails the OAM, as can be seen from Fig. 4.3. In the far field region it can be thus expected to

observe a typical vortex-like pattern, with a central dark spot surrounded by a bright intensity distribution.

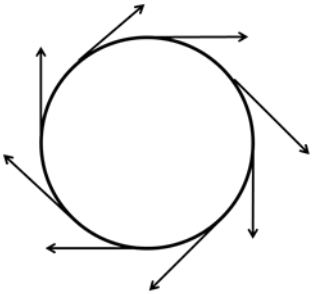

Figure 4.3. Projection on the transverse plane of the Poynting vector components corresponding to the azimuthal distribution of light sources. The composition of this source gives rise to an overall intensity vector which rotates around the propagation axis, thus entailing OAM.

In order to obtain desired pattern, the N emitters should be placed on the same plane and separated of a fixed angular distance. However this condition is not sufficient for producing OAM; as a matter of fact a helical wavefront is also necessary. This requisite can be satisfied by introducing among the light sources a constant azimuthal phase shift varying between 0 and 2π. In fact, if each emitter radiates with a phase difference of $2\pi/N$ with respect to the next, on the circumference the overall phase changes, discretely, of 2π, thus originating the equivalent of an optical vortex with unitary topological charge. This task can be accomplished by activating sequentially the emitters with a retardation of $2\pi/N$, a thing which can be done if these sources are driven by a circularly polarized incident field. The electric field vector of a CP beam rotates around the *z* axis as it propagates, hence light sources distributed on a circumference are illuminated sequentially as the rotation takes place.

The field generated by this circular array will have an angular momentum converted from SAM to OAM, therefore the generated orbital momentum per photon will be $\pm\hbar$, depending on the incident polarization handedness .

As pointed out in the previous chapters, OAM entails a torque effect; in this situation this phenomenon can be more evident if the inclination of the emitted field is increased, thus raising the tangential component of the Poynting vector. In the following paragraph more details about the nature of the emitters involved in the SAM to OAM conversion process will be provided.

4.3 Surface plasmon polaritons

The principle of operation described in the previous section have a completely general validity since the tilting effect can be obtained with whatever kind of emitter, regardless the dimensions or the underlying physical phenomena. Nevertheless nanoscale should be reached so that integrability of the device may be achieved; this implies that the most suitable emitters take advantage of plasmonic interactions which allow to use metal structure with sub-wavelength features.
Plasmons are collective oscillations of electrons inside a metal. Particularly surface plasmon polaritons (SPP) are electromagnetic modes propagating on the surface of an interface between a dielectric and a metal confined in the direction orthogonal to the metal surface. The conductor can be described using the free electron gas model, in which electrons are free to move inside the metal.

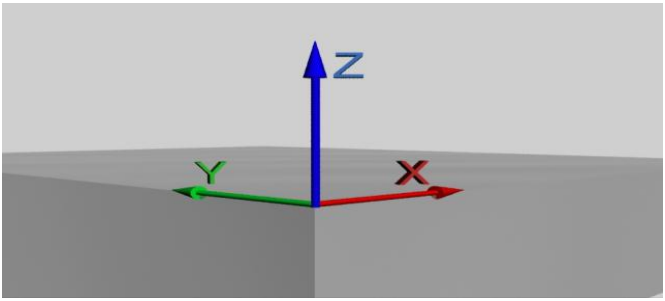

Figure 4.4. Metal – dielectric interface. The surface plasmon propagates along *x* and is confined in the *z* direction

Surface plasmons (SP) can be excited by properly coupling an incident electromagnetic field and the plasma oscillations of the metal [60] through a suitable matching condition which accounts for the momentum conservation principle.

In order to understand the physical phenomenon, a simple structure composed by an interface metal – dielectric on the plane $z = 0$ may be considered.
As suggested from figure 4.4 it can be supposed that the surface plasmon propagates in the x direction; moreover the electromagnetic mode should have an evanescent wave dependence (i.e. imaginary component of the wave vector) along z and does not vary along the y axis.
The field can thus be written as:

$$\mathbf{E}(x,y,z) = \mathbf{E}(z)e^{i\beta x} \tag{4.1}$$

being β the plasmon polariton's propagation constant, i.e. the wave vector component along the propagation direction.
If Eq. (4.1) is substituted in the Helmholtz equation the following well known relation is found [74,75]:

$$\frac{\partial^2 \mathbf{E}(z)}{\partial z^2} + \left(k_0^2 \varepsilon - \beta^2\right)\mathbf{E}(z) = 0 \tag{4.2}$$

where k_0 is the wave number in vacuum and ε is the dielectric constant of the medium.

Making explicit the harmonic time dependence $\left(\frac{\partial}{\partial t} = -i\omega\right)$, considering the propagation expressed by Eq. (4.1) $\left(\frac{\partial}{\partial x} = i\beta\right)$, the spatial homogeneity in the y direction $\left(\frac{\partial}{\partial y} = 0\right)$ and taking advantage of the

Maxwell's relations, which correlate the electric and magnetic component of the light field, a set of equations for all the vectorial components of the electromagnetic field can be written:

$$\begin{aligned}
&\frac{\partial E_y}{\partial z} = -i\omega\mu_0 H_x \\
&\frac{\partial E_x}{\partial z} - i\beta E_z = i\omega\mu_0 H_y \\
&i\beta E_y = i\omega\mu_0 H_z \\
&\frac{\partial H_y}{\partial z} = i\omega\varepsilon_0\varepsilon E_x \\
&\frac{\partial H_x}{\partial z} - i\beta H_z = -i\omega\varepsilon_0\varepsilon E_y \\
&i\beta H_y = -i\omega\varepsilon_0\varepsilon E_z
\end{aligned} \qquad \textbf{(4.3)}$$

which allow solutions for wave with different polarizations. There are two main sets of solutions: the transverse magnetic (TM) or *p* modes, where the only nonzero components are E_x, E_z and H_y, and the transverse electric (TE) or *s* modes, where all the components are zero excepts H_x, H_z and E_y. By means of simple algebraic passages in which the continuity conditions of the electromagnetic field at an interface is considered, it can be demonstrated that surface plasmons, that is waves propagating along *x* with an evanescent dependence in the *z* direction, can exist only for TM polarization.

In order to have SP propagation on a metal – insulator interface the continuity condition requires that the two media should have the real part of their electric permittivity of opposite sign.

If the metal is modelled following the Drude model, its permittivity is given by the relation

$$\varepsilon(\omega) = 1 - \frac{\omega_p^2}{\omega^2 + i\gamma\omega} \tag{4.4}$$

being ω_p the plasma frequency of the metal and γ the collision frequency of electrons. Looking at Eq. (4.4) can be noticed that below the plasma frequency the condition $\mathrm{Re}[\varepsilon]<0$ is generally verified for a metal, while typically $\mathrm{Re}[\varepsilon]>0$ for a dielectric. Therefore a dispersion relation for surface plasmons propagating at a single interface is given by

$$\beta = k_0 \sqrt{\frac{\varepsilon_m \varepsilon_d}{\varepsilon_m + \varepsilon_d}} \tag{4.5}$$

where ε_m and ε_d are respectively the permittivities of the metal and of the dielectric. In real metals the permittivity possesses even an imaginary part, hence also β is complex. This implies that the plasmonic mode propagating along the interface would be attenuated; a characteristic length which takes into account this attenuation can be identified as $L = \left(2\,\mathrm{Im}[\beta]\right)^{-1}$, the so-called propagation length. Typically, in the visible regime, L ranges from 10μm to 100μm. Moreover, from Eqs. (4.4) and (4.5), the equation relating β and the z component of the wave vector k_z can be deduced:

$$k_z = \sqrt{\beta^2 - \varepsilon_d \left(\frac{\omega}{c}\right)^2} \tag{4.6}$$

Equation (4.6) entails that the confinement of the wave on the metal surface is tightly bound to the length of propagation L: higher confinements of the radiation correspond to smaller propagation distances. Therefore a high confinement can be reached by considering high values of the propagation constant β. In this regime the SP propagates with a characteristic frequency ω_{sp} given by

$$\omega_{sp} = \frac{\omega_p}{\sqrt{1+\varepsilon_d}} \tag{4.7}$$

For our purposes it is useful to understand how plasmonic interactions work in geometries composed by multiple interfaces, as happens in multi-layered structures.

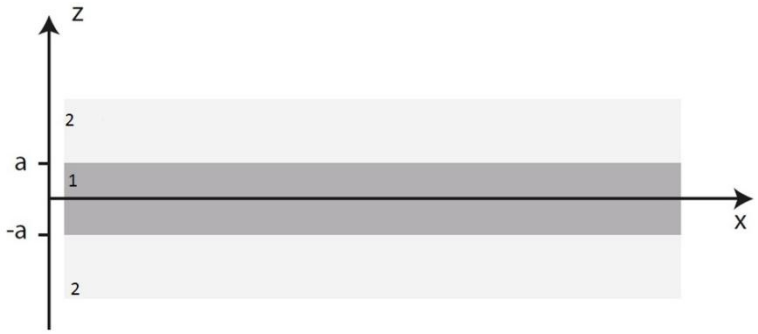

Figure 4.5. Multilayer structure. A medium with permittivity ε_1 is sandwiched between to symmetric half infinite media of dielectric constant ε_2.

Figure 4.5 shows the typical situation of a system composed by a dielectric layer with thickness a and dielectric constant ε_d sandwiched between two half infinite layers of metal whose dielectric function ε_m is given by Eq. (4.4) thus constituting a metal – insulator – metal (MIM) interface. The study of such a structure can of course be applied to the opposite configuration of an insulator – metal – insulator interface (IMI) by simply exchanging the dielectric constants' indices. However, since the electromagnetic sources studied in this dissertation are sub-wavelength slits, the following analysis is carried out by limiting to consider the MIM case, where the central dielectric is air.

In this structure the surface plasmons propagating at each metal – dielectric interface interact with each other, originating coupled modes. The dispersion relation of Eq. (4.5) therefore changes and is split in two

equations describing the conditions of existence of SP modes with even and odd vector parities.

$$\tanh k_d a = -\frac{k_m \varepsilon_d}{k_d \varepsilon_m}$$
$$\tanh k_d a = -\frac{k_d \varepsilon_m}{k_m \varepsilon_d} \qquad \textbf{(4.8)}$$

Equation (4.8) express the dispersion relation respectively of odd modes (E_x is an odd function of z while E_z and H_y are even) and even modes (E_x is even, E_z and H_y are odd).

Looking at these relation it is evident that the thickness of the dielectric layer a influences directly the propagation of such modes. As a matter of fact the lower is this thickness the higher is the coupling of the plasmons at the two interface; on the other hand, when a increases, the situation can be traced back to the problem of two separate metal – dielectric interfaces.

From Eq. (4.8) it can be easily seen that the fundamental odd mode has no cut-off frequency as the thickness a decreases. This entails that very high values of the propagation constant β can be reached, hence the field can be highly localized on the metal surface even for frequencies far below the characteristic frequency ω_{sp}, provided that very thin core layers are considered. This feature allows to excite high confined surface plasmons even in the infrared regime.

The capability of SPs of achieving such high field localizations leads to the possibility of confining the electromagnetic energy in volumes which are far smaller than the diffraction limit; it is indeed this fact behind the phenomenon of extraordinary transmission observed by Ebbesen *et al.* [52] and from which the device discussed in this work takes advantage. In fact in a sub-wavelength structure, as can be a nanoslit or a nanohole array, light can couple with SPs which propagate on the metal surface, thus crossing these sub-wavelength channel; on the other side of the structure the SP couples again with the electromagnetic radiation in the background medium thus re-emitting light.

It was pointed out that the presence of a SP mode is related to the evanescent behaviour in the *z* direction. To fulfil this requirement the *z* component of the wave vector should be imaginary so that the field decays exponentially from the surface.

Looking at Eq. (4.6) it can be noticed that this happens when the propagation constant of the SP is smaller than the wave number in the insulator. Therefore, in order to couple light with a surface plasmon, k_d must be greater than β. This means that is impossible to excite plasmons with standard techniques; as a matter of fact, if a flat metal - dielectric interface is considered, a light beam propagating in the dielectric half space and incident on the metal surface with an angle θ will have a wave number in the direction of propagation $k_x = k_d \sin\theta$ which is always smaller than the value of β given in Eq. (4.5) even at grazing incidence.

It is thus necessary to employ suitable techniques in order to excite a SP mode with incident light.

One of the simplest methods is the prism coupling used in the Otto configuration, where a prism is placed upon the metal layer leaving a thin air gap. If light hits the prism with an angle such that total internal reflection is achieved, an evanescent wave with wave number $k_x > \beta$ tunnels the air gap and excites the surface plasmon at the metal interface. Reversely the same phenomenon can be exploited to couple the guided plasmon to light, thus radiating.

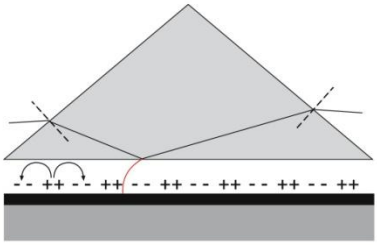

Figure 4.6. Prism coupling in the Otto configuration. Light hits the glass – air interface under total internal reflection conditions. The evanescent wave tunnels to the metal – air interface achieving phase matching with the SPP. Source ref. [60]

Nevertheless the most important solution, especially in the aim of this dissertation, to the issue of SP excitation, sees the generation of surface polaritons by means of suitable gratings.
This technique allows to achieve phase matching conditions, i.e. equalling the light and the plasmon propagation constants, by providing an extra momentum due to a grating patterned on the metal surface.
A periodic perturbation of the metal surface, which may be a shallow grating (a corrugation) etched on the metal or even made by a dielectric material deposed on the metallic layer, or a periodical hole (or slit) array with a lattice constant *a*, adds to the incident light a momentum component dependent on the lattice vector.

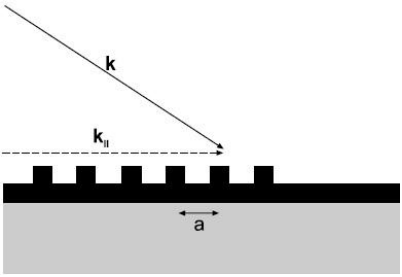

Figure 4.7. Grating coupling scheme. The momentum mismatch is compensated by the grating momentum vector.

Therefore plasmon excitation takes place when the condition

$$\beta = k \sin\theta \pm ng \qquad \textbf{(4.9)}$$

is fulfilled, being $g = \frac{2\pi}{a}$ the reciprocal vector of the grating and *n* is an integer indices which can be 1, 2, 3.... As happens for the prism coupling a periodic grating can be used in the reverse process of emission of a propagating plasmon.

The advantage of these method is the capability of tailoring the plasmonic interactions and the possibility of modelling them via analytical and efficient mathematical tools [61 - 63].
The momentum gap necessary to the plasmon excitation can also be filled by non-periodic surface perturbations. As a matter of fact a scatterer element present on the metal surface, when hit by the incident field, scatters light in all directions, thus producing a wide momentum spectrum. In this way it is possible to produce the extra momentum in the propagation direction Δk_x needed to fulfil the phase matching condition

$$\beta = k \sin\theta \pm \Delta k_x \qquad \textbf{(4.10)}$$

Naturally other techniques exist to couple light with surface plasmon polaritons, but they are beyond the scope of this thesis. However for completeness' sake will be briefly mentioned. One of them involves tightly focused optical beams obtained with a high numerical aperture objective, which possess large angular spreads, covering angles greater than the critical angle. Another method takes advantage of near field microscopic techniques to excite plasmons in sub-wavelength areas which configure as point sources (hence with enough high momentum). These techniques make use of probe tips with apertures far below the plasmon wavelength made of tapered optical fibres [64].

4.4 Transmission of light through a sub-wavelength slit

A simple slit with sub-wavelength features etched in a metal slab, from a plasmonic point of view, may be considered as a multi-layered structure discussed in the previous paragraph, where a dielectric medium – air in this case – is sandwiched between two half infinite (compared to the operating wavelength) blocks of metal. It was shown that in such metal – insulator – metal system the plasmonic fundamental mode with odd parity propagates regardless the thickness of the core layer. It was also pointed out that this phenomenon is the basis of the so-called extraordinary transmission of light through sub-wavelength apertures.

When one side of the aperture is illuminated by a light beam with TM polarization, thus having the electric field vector orthogonal to the MIM interfaces, as shown in Fig. 4.8, the edges of the slit behave as scatterers, providing the phase matching conditions necessary to excite SPPs on the metal surface. Practically these corners can be considered as point sources of surface plasmon polaritons.

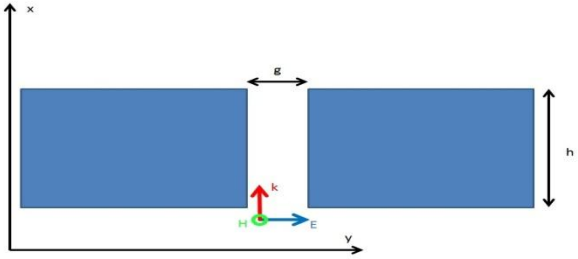

Figure 4.8. **S**lit with sub-wavelength width g. A TM polarized field hits the metal slab on the bottom side. The electric component is orthogonal to the MIM interfaces while the magnetic field is parallel to the aperture walls.

When the metal thickness is small in the x direction electromagnetic radiation tunnels the metal layer and is transmitted on the other side of the slab without the assistance of SP modes. The guided plasmonic interactions become relevant when the metal layer is enough thick so that light is prevented from direct tunnelling. As mentioned above, the scattered radiation activate plasmon modes which propagate along the inner walls of the aperture analogously to a waveguide. If the gap g of the slit is very narrow – far below the incident wavelength – there will be coupling between the SPPs on the two interfaces air – metal: they thus propagate with a common propagation constant β. Nevertheless the momentum spectrum provided by the interaction with the edges at the input plane possess enough spatial components to excite plasmons modes which propagate along the external surface of the slit, that is in the y direction. If the metal structure if sufficiently extended in the horizontal direction – more than the surface plasmon propagation length – and there are no

scattering elements on the SPPs propagation path, they do not interact with the channelled modes, thus not affecting the transmission.

When the guided SPPs reach the upper side of the MIM channel, they interact again with the edges of the output plane; these, on their turn, provide the momentum components necessary to fulfil the phase matching conditions, allowing the coupling of SPPs with air: therefore light is re-emitted in air [65]. On the other hand the interaction with the output corners causes a reflection of the plasmonic wave in the backward direction, thus inside the channel. This mechanism is repeated when the reflected surface mode reaches the edges at the input plane and so on. Therefore multiple reflections are generated inside the aperture which give rise to an interference pattern of the plasmonic wave on the slit's walls. Moreover there will be other components of the electromagnetic field which are emitted in air on the bottom side and which propagates on the input surfaces.

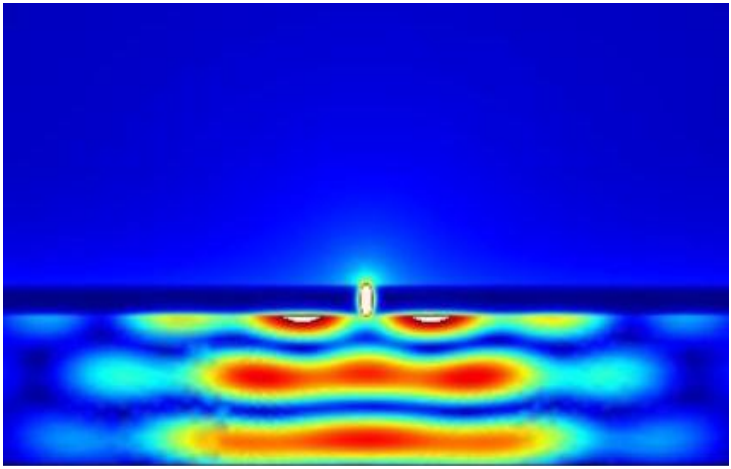

Figure 4.9. Transmission of the electromagnetic field through a sub-wavelength slit in a metal layer. The TM polarized incident wave excites surface plasmons as interacts with the slit's corners. The generated SPPs propagate inside the aperture and are radiated on the other side of the slit. Part of the power is reflected back. Additional SP modes propagate on the input and the output metal surfaces.

Similarly, on the output side, a portion of the upcoming plasmonic wave crosses the corner and propagates on the upper metal surface, as can be seen in Fig. 4.9. Looking at Fig. 4.9 it can be noticed that there is a strong localization of the field inside the aperture and that the light emitted on the output plane of the slit is radiated with an isotropic pattern.
If we consider a sub-wavelength slit similar to the one discussed so far but with misaligned edges on the output plane, the emission pattern on the exit plane changes from being isotropic to a tilted directional profile.

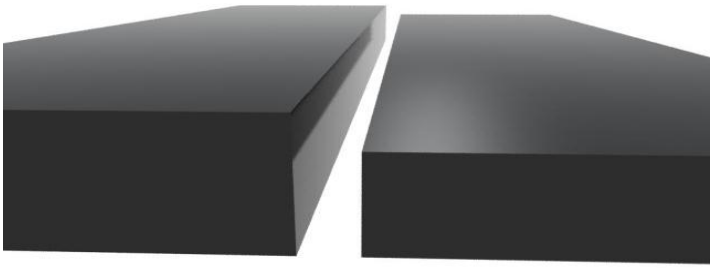

Figure 4.10. Unbalanced sub-wavelength aperture. The left edge on the output plane is higher than the right one.

Figure 4.10 depicts a three dimensional view of the structure: the left edge is placed at a difference height with respect to the other border. As shown from Fig. 4.10 the nano aperture configures as an infinite slit in the z direction, that is the direction orthogonal to the plane of Fig. 4.9; in this way spatial uniformity can be considered along this axis, thus simplifying the analysis. From now on this kind of misaligned slit will be referred as the unbalanced slit.
Similarly to the previous situation, on the input side an incident TM polarized electromagnetic field (with the E vector perpendicular to the aperture walls) illuminates the edges of the metallic structure. As is known surface plasmons are excited and part of them propagate inside the aperture with a propagation constant β. Since the considered slit has a very narrow width, of the order of some tens of nanometres, the SPPs are guided with a common mode index. When the surface waves reach the other side of the slab interaction with the corners takes place; however the plasmon guided

on the higher side (left, referring to Fig. 4.10) will be scattered after it propagated for a longer path with respect to the mode on the other wall. Moreover, when the height of the lower corner is passed, the SPP on the left wall propagates decoupled from the other one as happens in a single metal – dielectric interface. Therefore while in the common waveguide stretch the surface plasmons are coupled, hence are guided with a common β, in the remaining stretch the surviving plasmon propagates with a propagation constant k_{sp} given by the single interface dispersion relation of Eq. 4.5. When studying the field at the output plane multiple reflections inside the channel can thus be neglected, since they are common to the plasmons on both the walls; the only relevant factor is the path difference related to the constant k_{sp} of the single interface stretch.

The edges of the slit therefore will emit light into air with a phase retardation equal to $k_{sp}d$, being d the height difference between the borders. If a two dimensional structure is considered, a corner where plasmonic interaction takes place, can be treated as a point light source; the three dimensional geometry discussed above can thus be represented as a linear distribution of point sources along the z direction. Consequently the problem of the emission of the unbalanced aperture can be modelled as a diffraction problem involving two point sources, one for the left and one for the right edge, emitting light with a relative phase difference of $k_{sp}d$ [66].

A solution of the first order for determining the emission pattern of the unbalanced plasmonic slit, following the above considerations, can be obtained by means of a Fresnel – Kirchhoff diffraction integral where two out of phase point sources are taken into account. For simplicity' sake can be conveniently chose the reference frame, as shown in Fig. 4.11, aligning it to the plane containing the slit borders. Therefore under the rotated reference system (x', y', z') the diffracted field emitted from the slit can be expressed as

$$E_F \propto \frac{1}{i\lambda}\iint \frac{e^{ikr'}}{r'}\delta(z')\left[\delta\left(y'+\frac{a}{2}\right)e^{ik_{sp}d}+\delta\left(y'-\frac{a}{2}\right)\right]dy'dz' \quad \textbf{(4.11)}$$

being k the wave vector of the radiated electromagnetic field, $k_{sp}d$ is the phase difference between the two sources and $a = \sqrt{g^2 + d^2}$ is the distance of the two edges on the output plane.

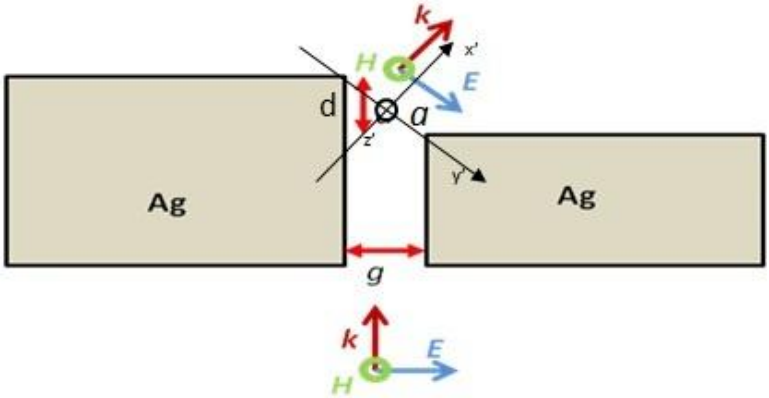

Figure 4.11. Unbalanced nano slit etched in a silver layer. The reference frame on the output side is tilted so that alignment with the emitters plane is achieved. The radiated electromagnetic field is tilted with respect to the incident beam propagation direction.

The emitted field will have a component of polarization parallel to the incident field and one perpendicular. In order to determine the emitted radiation pattern in the far field region, the Fraunhofer approximation may be used; equation (4.11) therefore becomes

$$E_F \propto \frac{2e^{ik_0\left(x'+\frac{y'^2+z'^2}{2x'}\right)+i\frac{k_{sp}d}{2}}}{i\lambda x'}\cos\left(\frac{\pi y' a}{\lambda x'}-\frac{k_{sp}d}{2}\right) \qquad \textbf{(4.12)}$$

It can be easily verified that the scalar field expressed by Eqs. (4.11) and (4.12) is effectively deflected with respect to the aperture's axis, i.e. the x axis, proportionally to the ratio a/d. This means that exists a dependence which relates the inclination of the emitted field, the width g of the slit and the height difference d between the output edges. Without losing general

validity this result can be extended to the three dimensional case, where the slit, as pointed out before, extends indefinitely along *z*, by considering that the far field pattern of Eq. (4.12) is the same for any value of *z*.
This simple scalar analytical model can obviously be applied to the balanced slit case, where the height difference is zero: it can be clearly seen that in this situation the field results un-deflected with respect to the *x* axis.

4.5 Azimuthal distribution of plasmonic light sources

It is convenient to recall that the aim of the device discussed in this chapter is to convert a light beam carrying spin angular momentum into a field with orbital angular momentum. It was showed that this can be done by mean of a superposition of opportunely distributed and, eventually, tilted light beams. The suitable arrangement of such sources sees theme disposed in an azimuthal array and activated with a fixed angular phase retardation.
From what was showed until now it can be easily understood that these emitters will be obtained from the unbalanced plasmonic slits presented in the previous paragraph, which, once illuminated by a locally TM polarized incident field, produce a deviation of the radiated field from the direction of propagation.
In order to accomplish this task, the issued device will be fabricated by opening slits in a sufficiently thick – in order to avoid tunnelling of light – metal layer. Each of these apertures should have its edges parallel to the radial direction; moreover each slit should be rotated about a pivot point placed in the symmetry centre of a constant incremental angular amount, as sketched in Fig. 4.12. It should be noticed that the helical wave front can be obtained both with balanced and unbalanced nano apertures, provided that a suitable illuminating field is considered; nevertheless unbalanced slits guarantee an additional torque effect since the more tilted Poynting vector possesses a higher tangential component.
Since the excitation of surface plasmons requires that the magnetic field **H** is parallel to the metal – dielectric interface, that is a TM polarization, a suitably polarized incident field should be chosen so that every slit receives

the correct illumination. This means that a linearly polarized beam is not appropriate to trigger surface plasmons in the whole device.

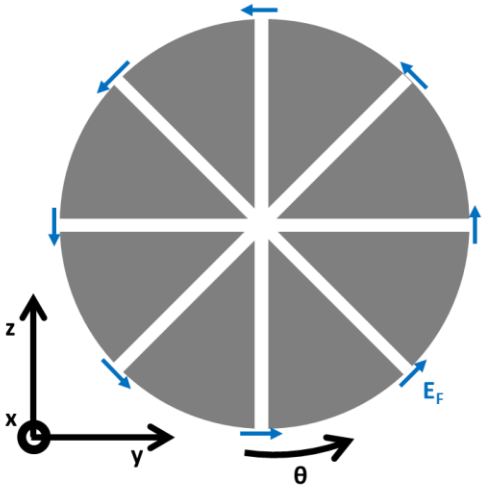

Figure 4.12. Outline of the plasmonic spiral phase plate (top view). The azimuthal distribution of nano apertures results in a metallic slice array. Each of the N slits is rotated of an angle $2\pi/N$ with respect to its preceding neighbour thus forming the equivalent of an azimuthal periodical grating. The illuminating field E_F must be orthogonal to the slit's walls, hence directed along the azimuth coordinate.

As a matter of fact, a linearly polarized beam would have its electric component orthogonal only to the walls of two opposite slits, while the other apertures would see a tilted or even parallel electric field. It becomes thus necessary to illuminate the structure with a field whose polarization is such that the electric field vector is locally orthogonal to each slit. Since the plasmonic channels are distributed along the azimuth direction, it is evident that the incident field can have only circular or azimuthal polarization. The latter is a polarization state in which the polarization vector points, at every position, in the azimuth direction; therefore the orientation of the polarization vector varies spatially while locally remains

linear, that is, at a fixed time all the points in the space see an electric field vector directed along θ with the same phase.

Nevertheless the fundamental requirement for generating OAM is to have a constant phase difference among the azimuthal sources, so that between the first and the last emitter a 2π phase shift is accumulated. Therefore the only polarization state suitable to excite plasmons in every slit is the circular polarization (with left or right handedness) because it guarantees, as happens for the azimuthal state, an electric field locally orthogonal to the walls and, since the field vector completes a rotation in a length λ, illuminates each aperture with a phase retardation equal to $2\pi/N$, being N the number of slits. As stated above, the latter feature is not present when the field is azimuthally polarized.

The field generated by such an array can be evaluated by making use of the mathematical model proposed in the former paragraph for the single slit. As a matter of fact, Eq. (4.12) can be used for each slit accounting a convenient rotation of the reference frame. Hence the contributes of the separate slits can be composed in order to obtain the overall field. Looking at Fig. 4.12 a general reference system (*x, y, z*) can be chosen to represent the whole device, then Eq. (4.12), written for the local slit output frame (x', y', z'), can be rearranged by firstly rewriting it according to the frame aligned with the slit's wall, then again to the main reference system. For simplicity's sake the main frame can be chosen coincident with the reference system at the input (*x, y, z*) of the first slit. Therefore two rotations are necessary to write the field of a generic aperture in the main reference system. A first rotation of an angle $\varphi = \arcsin(d/a)$ should be performed around the *z'* axis of figure 4.11 thus aligning with the slit's walls; the second rotation of the angle $\theta = j*(2\pi/N)$ is then performed about the *x* axis of the reference system showed in Fig. 4.12. Hence the two following rotation matrices can be applied sequentially to Eq. (4.12)

$$\begin{pmatrix} \cos\varphi & -\sin\varphi \\ \sin\varphi & \cos\varphi \end{pmatrix} \qquad \begin{pmatrix} \cos\theta & -\sin\theta \\ \sin\theta & \cos\theta \end{pmatrix} \qquad \textbf{(4.13)}$$

in order to obtain the field, in the Fraunhofer approximation, emitted by each aperture, evaluated in the reference frame of Fig. 4.12.
If the simpler case of the balanced slits is considered, the φ rotation is not present since $d = 0$ and the reference system at the output plane coincides with the one at the input plane of the aperture. The electromagnetic field is polarized so that the electric field vector is orthogonal to the channel's walls, thus along *y*; the polarization state is the same for each slit. The field radiated from the jth plasmonic waveguide forming an angle θ_j with the *z* axis will be :

$$\mathbf{E}_{Fj}(x',y',z',\theta_j) = \frac{2e}{i\lambda x'} e^{ik_0\left(x'+\frac{y'^2+z'^2}{2x'}\right)+i\frac{k_{sp}d}{2}} \cdot \cdot \cos\left(\frac{\pi y' a}{\lambda x'} - \frac{k_{sp}d}{2}\right)\left(\hat{\mathbf{y}}\cos\theta_j + \hat{\mathbf{z}}\sin\theta_j\right) \quad \textbf{(4.14)}$$

where $\hat{\mathbf{y}}$ and $\hat{\mathbf{z}}$ are the unitary vectors respectively along the *y* and *z* axis. It can be convenient to write the polarization vector expressed by the last term of Eq. (4.14) in a cylindrical coordinate system having the origin coincident with the centre of the device; it can easily be found that the polarization state of $\mathbf{E}_{Fj}$ is directed along the azimuth direction $\hat{\boldsymbol{\theta}}$.
The fields emitted by the azimuthally distributed sources compose as they diffract, giving rise to an overall diffracted field given by the sum of the N contributions $\mathbf{E}_{Fj}$ written in the device reference system.

$$\mathbf{E}_T(x,y,z) = \sum_{i=1}^{N} \mathbf{E}_{Fi}\left(x,y,z,\theta_i\right) = \sum_{i=1}^{N} E_{Fi}\left(x,y,z,\theta_i\right)\hat{\boldsymbol{\theta}} \quad \textbf{(4.15)}$$

Since each field is directed along the azimuth coordinate, emerges that the generated field will have azimuthal polarization, as expressed by Eq. (4.15). Figure 4.13 reports the intensity pattern of the overall field, estimated with the above mathematical model, generated by a plasmonic plate made of 32

slits and observed after a propagation distance of about 5mm. It can be noticed that the beams' deflection operated by the plasmonic sources results in an azimuthal distribution of the involved fields, as predicted from Fig. 4.3.

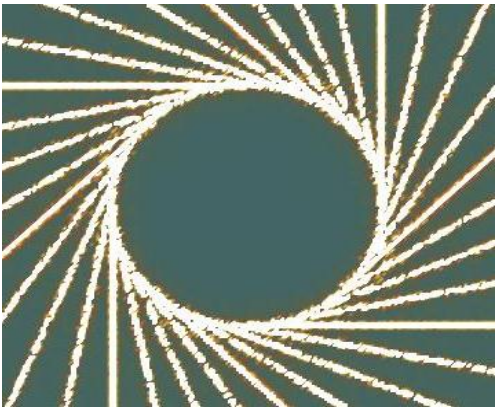

Figure 4.13. Intensity distribution of the field radiated by the plasmonic spiral phase plate observed after some millimeters of propagation. The fields emitted by the slits displace laterally with respect to the plate's axis originating a vortex-like distribution.

A final remark regarding the simplistic mathematical tool used until now should me mentioned. In fact this model refers only to the emission of the plasmonic light sources, aiming to determine the final diffracted generated field; thus all the underlying physical plasmonic phenomena present in the slits before that the interaction between the SPPs and the output edges takes place are not taken into account.

Therefore this model retains its validity until the slits can be considered as separated, not interacting objects. In this case more complex considerations should be made.

The non-interaction condition is fulfilled whenever sufficiently large distances from the centre of the device are considered. This means that, aside from technological remarks, the device should be fabricated with a central pillar enough wide to separate the nanoapertures.

4.6 Torque effect

It was shown in the previous sections that each unbalanced sub-wavelength slit emits an electromagnetic field with a tilted Poynting vector with respect to the aperture's axis. A non-negligible transverse component of such a vector will be present, growing with the height difference between the output borders of the slit. This entails that the metal structure undergoes to a net force which opposes to the Poynting vector. Since the slits are azimuthally distributed, the overall Poynting vector is, as shown in Fig. 4.3, rotating about the symmetry axis, resulting in a torque effect on the device.
This effect, as expected, is related to the square modulus of the magnetic field; the torque can thus be expressed as follows

$$C = N \int_0^{R_{\max}} \frac{m(h)}{c} d \left| H_0(r) \right|^2 r dr \qquad \textbf{(4.16)}$$

where c is the speed of light in vacuum, h the thickness of the metallic base of the structure, H_0 is the generated magnetic field, N is the number of apertures, d the height difference between the edges, $R_{\max}$ is the maximum radius of the plasmonic spiral phase plate, and m is a parameter dependent on the base's thickness.
The device can be designed in order that the produced torque effect is such to exert a rotation on the structure, provided that it is suspended in a liquid background.
If I is the moment of inertia of the PSPP, considering it composed by a solid half-disc, due to the upturned sides of the slits, superposed to the full disc of the base, it can be found that

$$I = \frac{\pi}{2} \left(\frac{d}{2} + h \right) R_{\max}^4 \rho \qquad \textbf{(4.17)}$$

being ρ the mass density per unit volume of the metal. Therefore the whole structure illuminated by a circularly polarized field undergoes to an angular acceleration equal to

$$\alpha = \frac{C}{I} \tag{4.18}$$

which, as can be noticed by looking at equations (4.16) and (4.17), can be dimensioned as a function of the typical features of the plasmonic phase plate.

4.7 Numerical Simulations

The PSPP behaviour can be further investigated, with a more precise degree of accuracy with respect to the simplistic model proposed in section 4.5, by modelling the output face of the slit on the plane *z = constant* (referring to the frame of Fig. 4.12) as an electric dipole aligned with the line linking the edges, and making use of a vectorial electromagnetic model. The slit, indefinitely extended along *z* can thus be represented as a linear distribution of oscillating tilted electric dipoles which have the typical radiation patterns with their maxima on the plane orthogonal to the dipole's axis, as can be seen from Fig. 4.14.

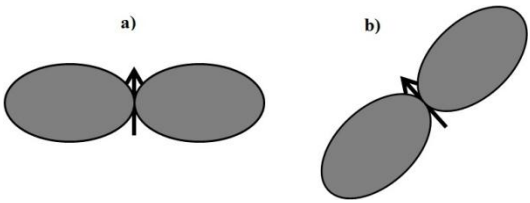

Figure 4.14. Oscillating dipole's radiation pattern for vertical (a) and tilted dipoles (b). The electric field is maximum on the orthogonal plane of the dipole's axis. If the dipole is tilted also the pattern undergoes to an inclination of the same angle.

Therefore the overall device can be seen as an azimuthal array of tilted oscillating dipole lines radiating on their local azimuth plane. This entails that the PSPP can be interpreted as a azimuthal distribution of nanoantennas. Figure 4.15 gives an outline of the device according to the dipole model.

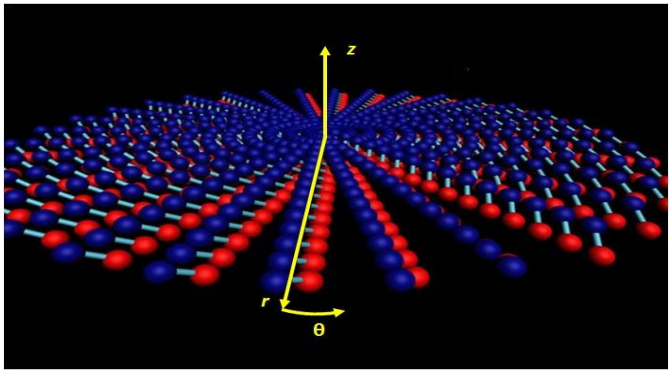

Figure 4.15. Electric dipoles model. The azimuthal array of sub-wavelength apertures is represented as a distribution of line dipoles tilted with respect to the *z* axis.

It may be convenient to adopt a cylindrical reference system for describing the dipoles distribution.
In the far field region, the electric field radiated by the aperture will have only the θ component, hence, using the frame of Fig. 4.15, it may be written as[67]

$$E = \frac{1}{4\omega\varepsilon_0}\sqrt{\frac{k_0^3}{r}}e^{ik_0 r}\, p_z \sin\theta\ \hat{\theta}\,, \qquad \textbf{(4.19)}$$

which entails a Poynting vector given by

$$\Pi \cong \frac{\mu_0}{16}\left|p_z\right|^2 \frac{\omega}{r}\sin^2\theta \qquad \textbf{(4.20)}$$

being p_z the dipole moment along the z direction.

The effective amplitude associated to each dipoles line can be obtained by multiplying Eq. (4.19) by a suitable parameter related to the transmission coefficient of the plasmonic plate, under the hypothesis that it is illuminated by an unitary amplitude field. The latter can be evaluated numerically with tools such as the finite elements method.
Starting from Eqs. (4.19) and (4.20) numerical simulations were performed in order to calculate the far field radiation pattern of the device. At the same time, other simulations were carried out for estimating the transmission behaviour of each slit. The obtained data were then merged so that a single numerical model capable of testing and dimensioning the overall device is obtained.
In this way the analysis of the structure was decomposed into two separated problems of interaction and emission, thus allowing to strongly reduce the computing resources. As a matter of fact, the issued structure has a complex geometry which requires a very high simulation's detail, i.e. a very tight mesh, in order to observe the plasmonic interactions which operate on lengths far below the illuminating wavelength. Therefore, since the device's dimensions are of the order of microns, the ratio of device's features and mesh elements' size would be very high, requiring a huge amount of spatial samples, thus making difficult to perform simulations with electromagnetic numerical tools as, for example, the Green method.

As pointed out before, the fields emitted by the apertures compose as they diffract, giving rise to a continuous field distribution with a rotating intensity vector; it was also noted that the larger is the number of slits, the higher would be the accuracy in producing an output helical wave front profile.
Looking at the emission problem, the device output behaviour was numerically simulated by calculating the electromagnetic field radiated by an azimuthal distribution of $N = 16$ dipole lines, each of them emitting an electric field expressed by Eq. (4.19), placed on the same plane $z = constant$ and with a relative phase shift of $2\pi/N$ between two neighbouring nano-apertures.

Therefore a vectorial propagation operator was applied in order to evaluate the intensity and phase patterns in the far field region.

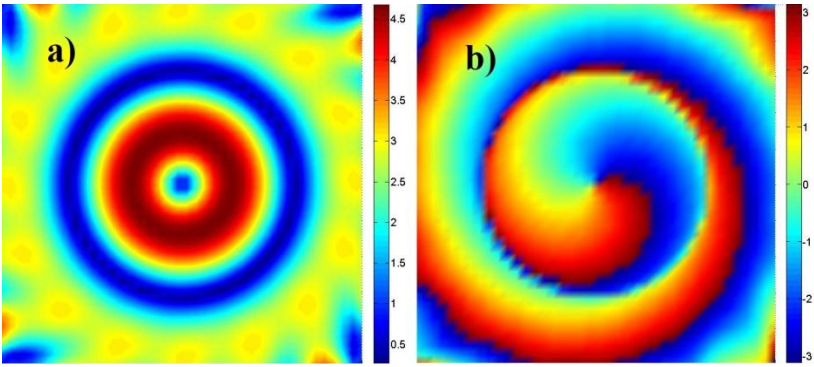

Figure 4.16. Modulus (a) and phase (b) of the *z* component (propagation direction) of the electric field generated by the azimuthal array of 16 light sources emitting with a relative phase shift of $2\pi/N$, evaluated in the far field region, after 500μm of propagation. The phase whirls around a central point ranging from $-\pi$ to π, hence an optical vortex is present on the propagation axis.

Figure 4.16 reports the modulus and phase of the electric field along the direction of propagation after it propagated for 500μm from the device plane, while in Fig. 4.17 it is shown the time averaged Poynting vector projected on the transverse plane.
It can be seen that even with only 16 slits the vortex – like behaviour is well reproduced since the phase spirals around the *z* axis changing its value of 2π; as a consequence also the dark central spot can be noticed in the intensity profile.

4.8 Dimensioning of the PSPP

When projecting the PSPP, the first issue concerns the metallic material used for the fabrication of the device which should be suitable for plasmonic applications. At an operating wavelength of 830nm, which is typical of common light sources as Ti:Sapphire femtosecond laser, one of

the most suitable metals is silver (Ag), since it does not introduce high losses.

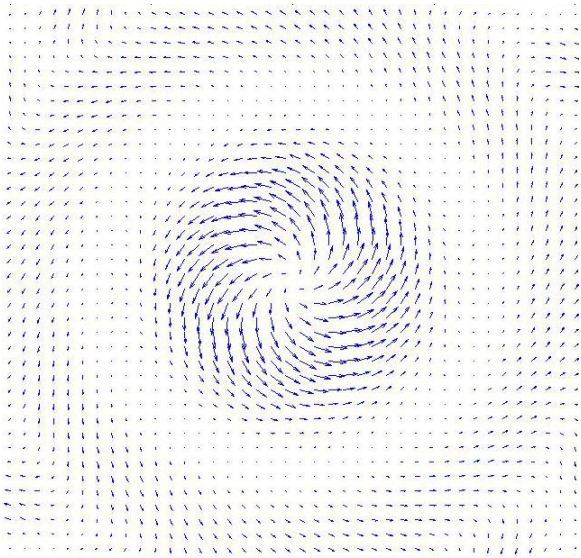

Figure 4.17. Time averaged Poynting vector on the transverse plane (x, y) . A tangential component is present, entailing the rotation about the propagation axis z, where the phase singularity is nested.

Dimensioning with other metals as gold (Au) is also possible provided that a proper wavelength is employed. At the chosen λ Ag has an electric permittivity of -25.22 and an electric conductivity of 3629 S/m [69].
The slits were designed in order to maximize at the operating wavelength the transmission coefficient, i.e. the percentage of the incident beam reaching the output plane, and the tilt angle of the generated field. The considered procedure can be followed with any wavelength or metal.
The main features of the plasmon based light source, that is width of the aperture and thickness of the metal layer, are determined by numerically creating a two dimensional map which relates the transmission coefficient with such parameters.

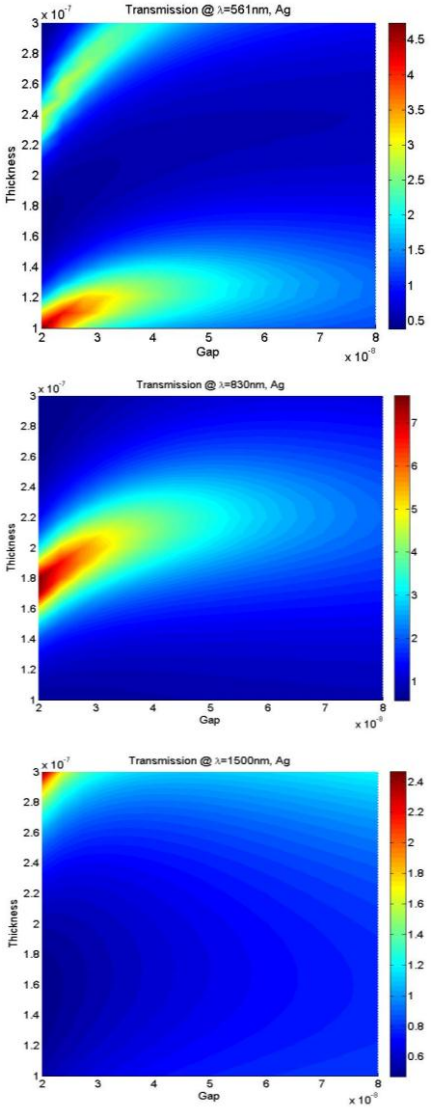

Figure 4.18. Transmission coefficient of a sub-wavelength slit etched in a silver layer as a function of the aperture's width and of the metal thickness, evaluated for three different wavelengths: a) 561nm; b) 830nm; c) 1500 nm.

For simulating the sub-wavelength slit the software COMSOL Multiphysics was used, carrying out parametric simulations where, for each value of the thickness *h* (see Fig. 4.8) the gap *g* varies, hence the ratio of the transmitted and incident fields is evaluated. In each simulation the aperture's width ranges from 20nm to 80 nm while the thickness changes from 100nm to 300nm. This procedure was then replicated for three significant wavelengths: 561nm, 830nm and 1500nm.

Figure 4.18 reports the transmission maps for a single slit cut in a silver layer. It can be noticed that a strong transmission peak is present for some thickness and gap values; this peak moves toward higher values of the thickness *h* as the incident field's wavelength increases.

As mentioned before, the main interest is toward the wavelength of 830nm, therefore the optimum parameters were chosen according to the transmission map of Fig. 4.18. Keeping in mind the practical and technological limits which do not allow to grow with high precision metal layers or to etch apertures whose thickness and width are too small, it was chosen as the optimal dimensioning point the couple of values 200nm and 35nm respectively for the metal thickness and the aperture's gap.

As a matter of fact, with a fixed value of *h*, as it is shown in Fig. 4.19a, a maximum in the transmission curve can be found corresponding to a slit 35nm wide.

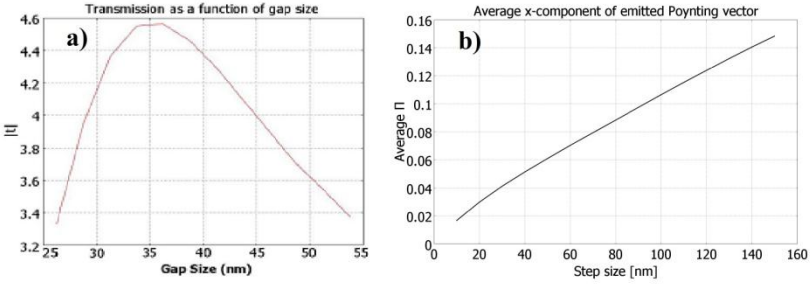

Figure 4.19. a) Transmission coefficient (modulus) of the slit as a function of the gap size: a plasmonic resonance peak is present at 35nm; b) Averaged horizontal component of Poynting vector of the emitted electromagnetic field: positive values correspond to right tilted vector, negative values to left tilting.

It should be noticed that the transmission do not increase linearly as the gap becomes wider but has a distinct peak; this is because the value of 35nm corresponds, for the selected metal and thickness, to a plasmonic resonance which boosts the transmitted field.
Once thickness and gap are determined the height difference *d* between the borders on the output face of the slit has to be found. This can be done by holding fixed *h* and *g*, hence evaluating a quantity representative of the tilting of the generated field. For this sake the horizontal component of the Poynting vector is particularly suitable because the more is the beam tilted, the higher will be this component. These tilting index can be further improved if an average is performed on a semicircle, with a radius large enough to enclose the aperture, which covers a portion of the output half – plane. Positive values of the averaged *x* component of the Poynting vector thus correspond to a beam tilted toward right, while negative values indicate left oriented tilted beams. In the issued simulations it was chosen a semicircle with radius of about 10μm, so that plasmons propagating on the upper face of the slits are enough attenuated, thus not contributing to the calculated average. The considered nanoslit, as shown in figures 4.10 and 4.11, has the higher edge on the left side, therefore it can be expected that, as *d* grows, the positive *x* component of the Poynting vector increases, entailing a right tilting of the output field.
Looking at Fig. 4.19b, the curve relating the averaged *x* component of the Poynting vector and the step (height difference) size is shown. With fixed gap and thickness the parameter *d* was changed from 0nm (balanced slit) to 150nm. It can be seen that a quasi linear dependence exists, thus allowing to choose the value of *d* corresponding to the desired tilting. However there are some considerations which limit the choice of the step size *d*. As a matter of fact, as *d* increases higher order surface plasmon modes propagate along the aperture's wall which produce nodes in the field distribution on the metal surface. If one of these node correspond to the upper edge of the slit, coupling with light in air is reduced, entailing a minimum in the radiated field. Furthermore higher order modes cause the existence of multiple emitting points of the metal surface, thus introducing fringes in the generated pattern and, as a consequence, reducing the directivity of the device.

Figure 4.20 depicts the magnetic component of the field interacting with the unbalanced nanoaperture dimensioned as follows: base thickness *h* of 200nm, aperture's width *g* = 35nm, height difference between the edges equal to *d* = 150nm. It is evident how the generated field results deflected toward the right direction. It can be also seen that the surface plasmons propagating on the input (lower) and output (upper) faces of the slit are enough attenuated before they reach the borders, thus preventing the existence of undesired reflections.

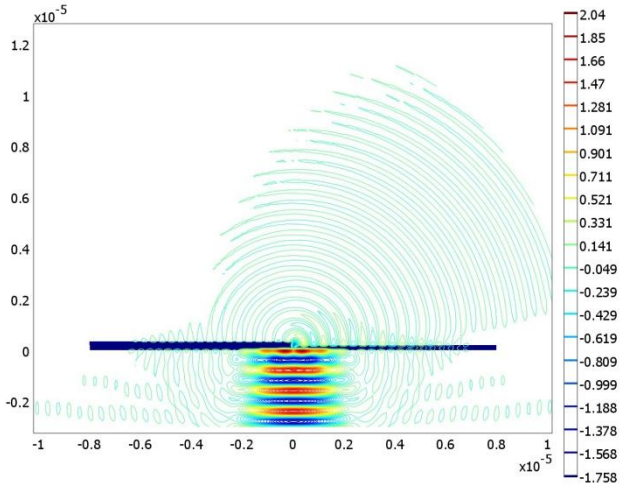

Figure 4.20. Contour map of the amplitude of the overall magnetic field at a wavelength λ = 830nm for a silver nano aperture 35nm wide, etched in a metal layer of 200nm and with a step size of 150 nm.

The simulations discussed in paragraph 4.7 made use of the transmission coefficient within from the interaction problem for evaluating the effective amplitude of the field emitted by the dipole lines.

The chosen values for the device's salient parameters, reported also in Fig. 4.21 which collects the results obtained from the simulations discussed until now, allow to estimate the torque effect by applying Eqs. (4.16) and (4.18). In fact it can be found an overall torque C = 3.5 10^{-21} Nm and an angular

acceleration $\alpha = 2\ 10^{-4}$ rad/s^2 which are sufficient to make a free PSPP to rotate about its axis.

The device presented in this chapter therefore configures as an angular momentum converter which transforms a SAM incident field in a beam carrying OAM. Furthermore it is a device working on the micro- and nano-scale, allowing to employ it for generating optical vortices within the field of integrated optics. Moreover, since the size of the PSPP is particularly reduced, the torque effect present in all the OAM generating devices, is no more negligible, allowing to take advantage of it for micromachining purpose. As a matter of fact the rotating effect can assimilate the PSPP to a micro helix which can be exploited, for example, as a micro gear or even as a micro turbine.

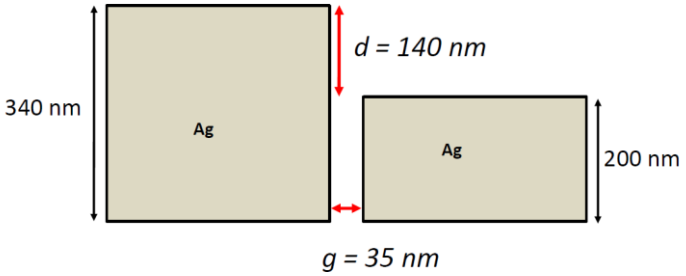

Figure 4.21. Outline of the sub-wavelength slit etched in silver layer, optimized for maximum transmission and tilting of the electromagnetic field.

Part 3

Measurement of Orbital angular momentum

Chapter 5

Measurement of the topological charge of an optical vortex by single slit diffraction

Until now we focused on the problem of generating optical vortices, hence orbital angular momentum. However, a fundamental issue concerns the possibility of measuring the salient features of the generated OVs, like the magnitude and the sign of their topological charge.

Clearly this is not a novel field of research because the topological charge was measured since the beginnings of singular optics. As a matter of fact are indeed information coming from such techniques that allow to correctly generate vortices.

The most common and proved methods for measuring topological charges rely on interferometry. In 1992 Bazhenov *et* al. [35], in one of the seminal papers on singular optics, showed that the interference pattern obtained from the interaction of a reference plane wave incident with an angle 2θ and a helical beam, is a grating with a dislocation nested in its centre. Differently from the interference pattern of two plane waves, one of the fringes disappears (or originates) in the centre of the grating, thus distorting the periodic pattern. An intensity given by the following equation was found:

$$I\left(\rho,\varphi,z\right)=E_0^2+\left(E_0\rho e^P\right)^2+2E_0^2\rho e^P\cos\Phi \qquad \textbf{(5.1)}$$

where

$$P = \ln \frac{\left(k_x \sin\theta A/2\right)^2}{z^2 + \left(k_x \sin\theta A/2\right)^2} - \rho^2 \frac{A}{A^2 + \left(\dfrac{2z}{k_x \sin\theta}\right)^2}$$
$$\Phi = \varphi - \rho^2 \frac{2z/\left(k_x \sin\theta\right)}{A^2 + \left(\dfrac{2z}{k_x \sin\theta}\right)^2} - \arctan \frac{Ak_x \sin\theta}{2z} + \pi \qquad \textbf{(5.2)}$$

being *A* related to the initial conditions. The experimental pattern obtained by this interference scheme is reported in Fig. 5.1. It is worth noting that this technique allows also to measure the sign of the dislocations: different signs cause different orientations of the bifurcation in the fringe pattern.

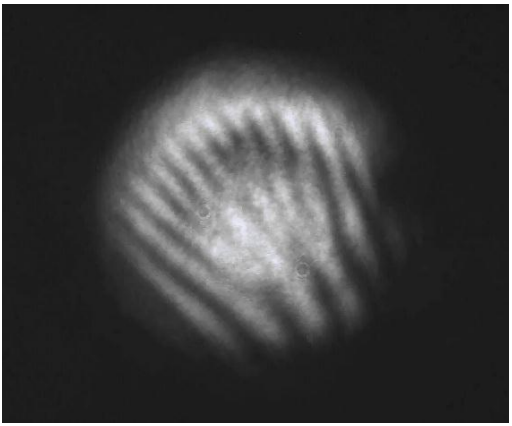

Figure 5.1. Experimental intensity pattern of the interference between a plane wave propagating with an inclined incident angle and a helical beam with non-integer topological charge.

This result suggested the idea of generating optical vortices by nesting a dislocation in their phase profile, leading to the well-known fork hologram. In fact, reversing the problem Bazhenov *et al.* proposed to reconstruct the

screw dislocation wave-front by using the diffraction of a plane wave by a synthetized grating including the dislocation itself. Since 1992 this technique was improved, and computer generated holograms became the most used technique for generating optical vortices. They were overcome only when liquid crystals based spatial light modulators, working on the same principles, were employed.

Since then, the many alternative solutions were proposed in order to avoid the use of experimental setups requiring accurate alignment of the interfering beams. Therefore simpler interferometric setups were used, starting, for example, from a Young's double slit experiment [78]. In this paper, the bending and orientation of the interference fringes originated by illuminating a double-slit screen with a Laguerre-Gaussian beam, is used as a measuring parameter for the magnitude and sign of the topological charge. This bending is due to a non-uniform phase term between the edges of the slits and related to the presence of a helical wave-front. However in reference [78] are not reported measurements of topological charges higher than 1. Moreover, from the amount of the bending would be difficult to distinguish accurately the magnitude of the OV.

In recent years other configurations, always relying on diffraction by apertures, were proposed. The most interesting works see characterization of the optical vortex by studying the diffraction pattern produced by annular [79], hexagonal [80] or triangular apertures [81]. All of the techniques proposed by references [79-81] performing a spatial spectral analysis of the beam, allow to detect without any ambiguity both the magnitude and the sign of the topological charge of the incident vortex, even when high values of the topological charge are involved.

Nevertheless it was demonstrated that a simple setup of a single-slit diffraction experiment, can be sufficient to characterize the optical vortex beam [82]. In this experiment, light fields carrying OVs were let to illuminate a screen with a single slit. Because of the non-uniform phase term discussed in Ref. [78], there is, as expected, bending of the interference fringes; their orientation reveals the sign of the topological charge. However the dark spot of the OV beam causes also the presence of a nodal line at the centre of the pattern; this, besides the bending, allows to measure also the magnitude of Q, since the number of nodal lines directly

depends on the topological charge itself. Ghai *et al.* [82] specify that, since the dark core widens, with this technique, is difficult to perform measurements on OV with Q higher than 2.
In this chapter an evolution of the latter technique is discussed, in order to overcome the limits intrinsically related to what proposed in Ref. [82].

5.1 Diffraction from a single slit

For determining the field diffracted by a narrow aperture, if the dimensions of the slit are significantly larger than the incident wavelength, an elementary optical model based on transmission functions can be used.
If a plane wave illuminate a slit infinitely extended along the *y* dimension and with an aperture, along the *x* axis of 2*a*, is considered, it is well-known that the diffracted field in the Fraunhofer region will be proportional to the Fourier transform of the field emerging from the aperture. Modelling the slit with a *rect* transmission function, the emerging field will have a disturbance given by

$$U = rect\left(\frac{x}{a}\right) \tag{5.3}$$

which, in the far field region, will produce an intensity pattern with a sinc^2 dependence on the transverse coordinate.
Considering as the incident field, a plane wave carrying a phase singularity, i.e. with a helical wave-front, the emerging field can be simply written as

$$U = rect\left(\frac{x}{a}\right)e^{il\varphi} \tag{5.4}$$

The diffracted field can be calculated by using the Fraunhofer integral which gives the profile expressed by Eq. (5.5).

$$I = a^2 \frac{\sin^2\left(\frac{\pi}{\lambda} a \sin\alpha + \delta\right)}{\left(\frac{\pi}{\lambda} a \sin\alpha + \delta\right)^2} \qquad \textbf{(5.5)}$$

In Eq. (5.5) the additional phase term δ accounts for the non-uniformity of the helical phase and is proportional to the difference of the phase evaluated in the left and right sides of the slit. This term is responsible for the bending of the interference fringes discussed in the above references.
Looking at the intensity pattern, it was pointed out that a single slit illuminated by a plane wave produces a sinc^2 diffraction pattern. However when a vortex beam illuminates the slit, the dark core entails the splitting of the sinc in the far-field region, causing a nodal line separating the two central intensity lobes. Increasing the topological charge lead to doubling the nodal lines, giving information about the magnitude of optical vortex.
When topological charge is larger than 2 or 3, the dark core of the OV beam begins to cover completely the slit, making difficult to produce distinguishable patterns.
However, if the slit is moved in the horizontal direction, a full scan of the vortex beam can be performed, thus realising a sort of tomography which allows to measure higher values of Q. As a matter of fact, by moving the slit in the *x* direction, diffraction fringes are dynamically modified, reducing to the simpler case of single (or small) topological charge.

5.2 Numerical simulations

In order to verify the possibilities related to the proposed method, an experimental setup as described in Fig. 5.2 was numerically simulated.
As usual, Laguerre-Gaussian modes are used for modelling optical vortex beams. These illuminate a narrow slit, several microns wide, placed in the plane $z = 0$. The emerging field, given by the product of the incident beam on the plane $z = 0$ and the transmission function, is expressed by Eq. (5.6)

$$U(\xi,\eta,z=0)\equiv U_0\equiv E_0\tau_0=\left(\frac{\sqrt{\xi^2+\eta^2}\sqrt{2}}{w}\right)^{|l|}e^{-\frac{\xi^2+\eta^2}{w}} \times e^{ikz}e^{il\varphi}L_p^{|l|}\left(\frac{2\left(\xi^2+\eta^2\right)^2}{w^2}\right)rect\left(\frac{\xi-\xi_0}{a}\right) \quad \textbf{(5.6)}$$

where ξ_0 is the centre of the slit, ξ and η are the transverse coordinate on the plane $z = 0$. Field given by Eq. (5.6) is then propagated in the free space. A lens of focal length f performs a Fourier transform on the field, so that the light collected on a screen is the far-field intensity distribution.

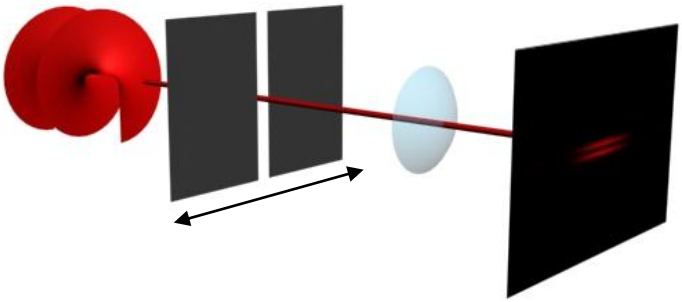

Figure 5.2. Sliding single slit experiment. A vortex beam illuminates a narrow slit. The diffracted light is collected by a lens of focal length f which realises a far-field transformation. A screen is placed on the back focal plane of the lens. The intensity profile is a sinc^2 with its central lobe split by a nodal line. The slit is moved along the horizontal direction.

Simulations were performed by using a rectangular 300×300 spatial mesh, which resulted at the same time, accurate and easy to handle numerically, since a matrix based integration was used to calculate Fourier transforms. Far field pattern on the back focal plane of the lens was evaluated by solving the Fraunhofer diffraction integral:

$$U(x,y,z=2f) = -\frac{i}{\lambda f}\exp\left[ik\left(f+\frac{x^2+y^2}{2f}\right)\right] \times\iint U_0(\xi,\eta,0)\exp\left[-\frac{ik}{f}(x\xi+y\eta)\right]d\xi d\eta \quad \textbf{(5.7)}$$

Eq. (5.7) was numerically integrated for every position of the slit, that is the parameter ξ_0 is let free to change in order to scan the whole beam's transverse profile.

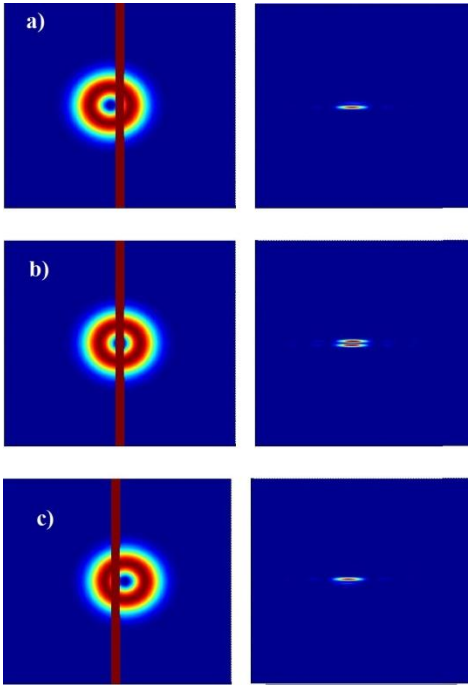

Figure 5.3. Incident field (left column) and calculated far field pattern (right column) obtained from the sliding single slit experiment for a vortex with topological charge Q = 1. As the slit moves from left to right, the fringes move from the bottom to the upper part of the figure. a) ξ_0 = -32μm; b) ξ_0 = 0μm; c) ξ_0 = 32μm

In the considered setup, the incident beam is chosen with an operating wavelength of 1μm and a spot size of 500μm; the slit is 50μm wide and infinitely extended in the vertical direction.
Figure 5.3 and 5.4 report the intensity profiles of the calculated far field for different values of the slit's displacement, together with the relative position of incident field and aperture. Figure 5.3 shows the experiment for a topological charge Q = 1, while figure 5.4 for Q = 1.

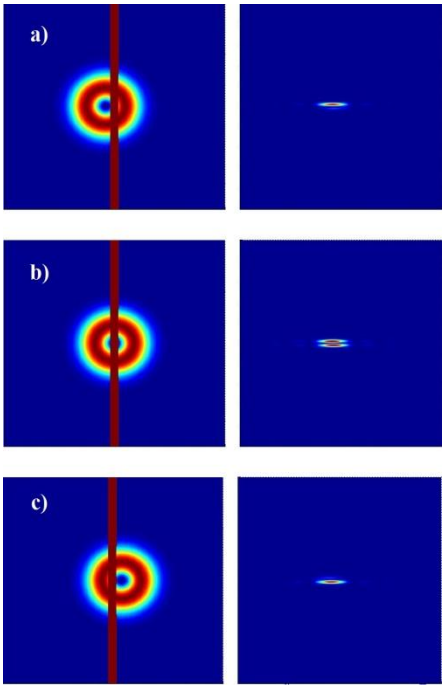

Figure 5.4. Incident field (left column) and calculated far field pattern (right column) obtained from the sliding single slit experiment for a vortex with topological charge Q = -1. As the slit moves from left to right, the fringes move from the upper to the bottom part of the screen. a) ξ_0 = -32μm; b) ξ_0 = 0μm; c) ξ_0 = 32μm

It can be seen that for a positive value of the topological charge, as the slit moves from left to right, the sinc^2 pattern moves from down to up, while,

when Q has opposite sign, the fringes move toward the lower part of the screen. Looking at these figure, the bending of the diffraction fringes can be also noticed.
However such results are not surprising since can be obtained also from the fixed single slit experiment, as happened in reference [82]. The advantages of this technique can be appreciated when higher topological charges are taken into account, as shown in Fig. 5.5 and 5.6.
As the slit moves, the fringes move following the same trajectories of the case of unitary topological charge. However the number of central intensity maxima increases. As a matter of fact, when unitary topological charge was considered, the far field intensity pattern revealed two main lobes separated by a dark nodal line. On the other hand, in this case, the horizontal movement of the aperture reveals 4 lobes separated by 3 nodal lines which appear sequentially.
Of course this can be expanded also to higher topological charges. Therefore, the magnitude of the topological charge of an optical vortex can be measured by counting the number of main intensity maxima appearing during the scan. It is found that Q equals exactly the number of nodal lines separating the lobes. The sign of topological charge, is given by the direction along which the fringes move.

5.3 Rectangular aperture

A further improvement of this technique can be found considering a rectangular aperture, i.e. a slit limited in both horizontal and vertical directions.
In this case the non-uniform phase term is accumulated not only between the left and right side of the aperture, as happened for the one dimensional slit, but also between the upper and lower side. In the situation of a slit infinitely extended along one direction, the diffraction pattern showed bent fringes because the term δ is accumulated only in the limited direction.
As pointed out before, δ depends on the phase difference between the edges.

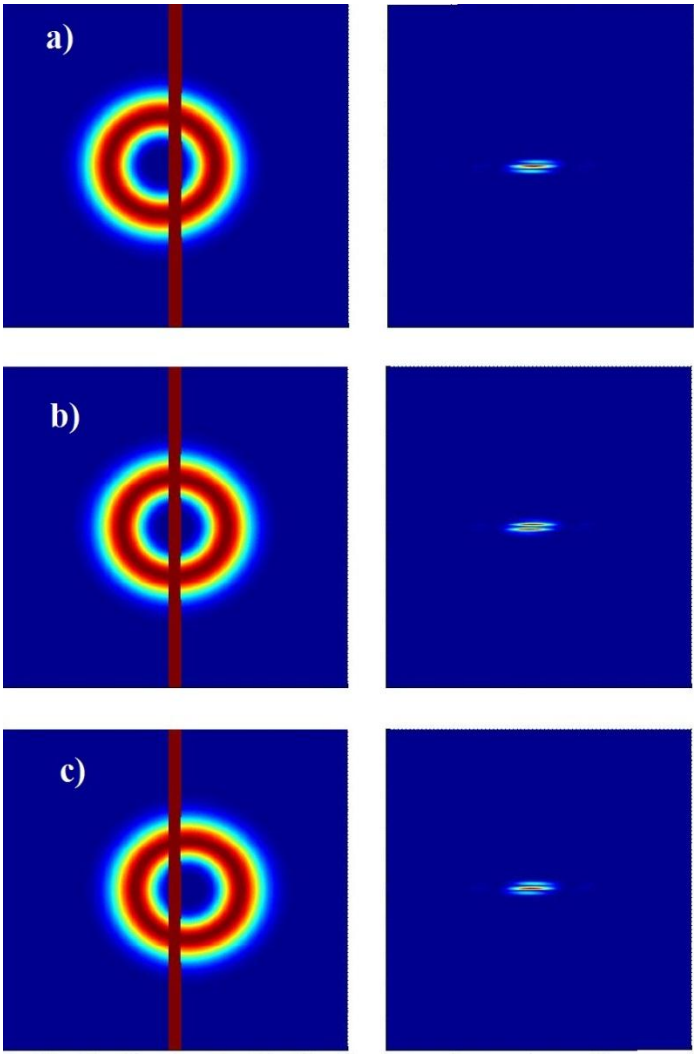

Figure 5.5. Incident field (left column) and calculated far field pattern (right column) obtained from the sliding single slit experiment for a vortex with topological charge Q = 3. As the slit moves from left to right, the fringes move from the bottom to the upper part of the screen. a) ξ_0 = -32μm; b) ξ_0 = 0μm; c) ξ_0 = 32μm

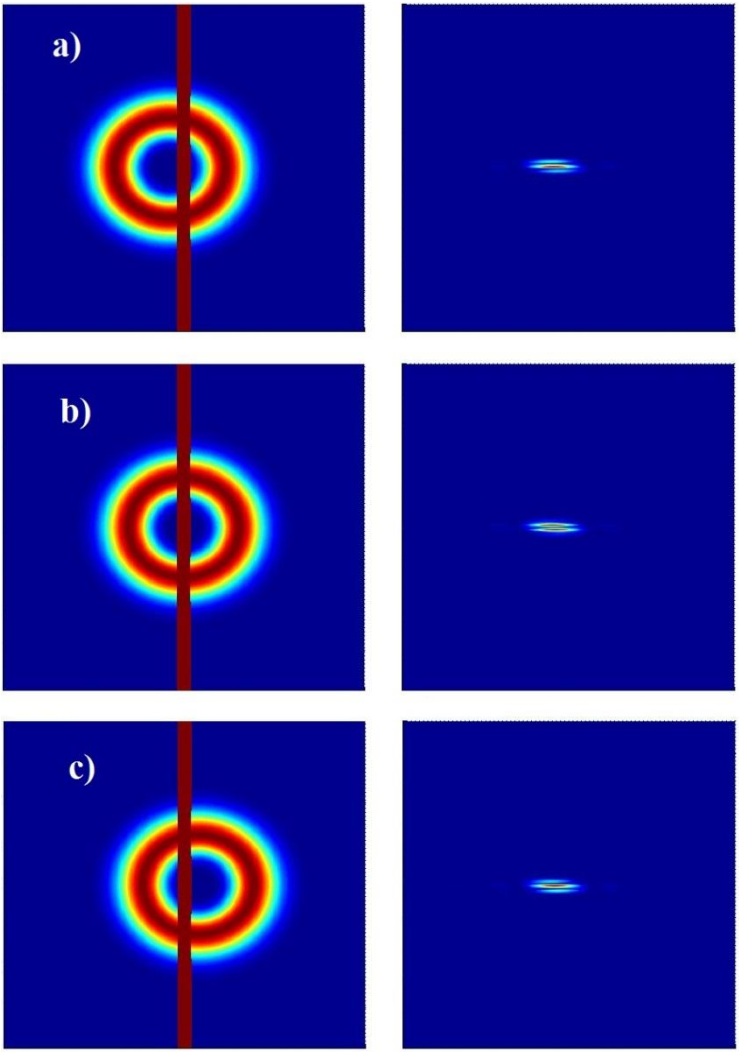

Figure 5.6. Incident field (left column) and calculated far field pattern (right column) obtained from the sliding single slit experiment for a vortex with topological charge Q = -3. As the slit moves from left to right, the fringes move from the upper to the bottom part of the screen. a) ξ_0 = -32μm; b) ξ_0 = 0μm; c) ξ_0 = 32μm

Since in a helical beam the phase changes uniformly of 2π on a circumference around the singularity, when an aperture limited in both horizontal and vertical direction is considered, as its aspect ratio approaches unity, δ tends to become the same along x and along y. This implies that, in a square or circular aperture, the additional phase term is compensated, and the bending of the fringes in the diffraction pattern disappears.
Apparently this may appears to be limiting for the sign determination of the topological charge. However, since there is spatial limiting in both directions, more spectral components are included in the far field pattern, allowing to easily measure the magnitude of higher topological charges, by sacrificing the possibility of determining the sign.
Adopting the setup proposed in this chapter, where the aperture moves with respect to the incident field, thus performing an horizontal scan of the beam itself, may overcome this limitation.
As a matter of fact, by following the dynamics of the intensity maxima appearing on the far-field screen, it is possible to distinguish between two opposite orientations of the optical vortex. As described in the previous paragraph, if the intensity lobes migrates from the bottom to the upper part of the screen a positive topological charge is present, otherwise the sign of Q is negative (or vice versa , depending on which direction is chosen as positive).

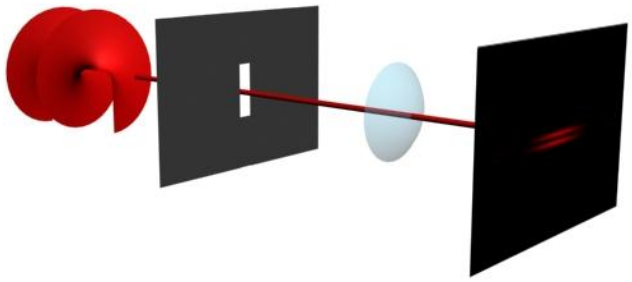

Figure 5.7. Sliding rectangular aperture experiment. A vortex beam illuminates a rectangular aperture. The diffracted light is collected by a lens of focal length f which realises a far-field transformation. A screen is placed on the back focal plane of the lens. The intensity profile is a sinc^2 with its central lobe split by a nodal line. The aperture is moved along the horizontal direction.

Also for this case numerical simulations were performed, referring to a setup, depicted in Fig. 5.7, similar to the one described in the previous paragraph.
For this sake an aperture with a moderate aspect ratio1:4 was chosen, under analogous illuminating conditions of the previous situation, i.e. wavelength of 1μm and spot size of 500μm. The transmission function of such aperture will be:

$$\tau_0 = rect\left(\frac{\xi - \xi_0}{a}\right) rect\left(\frac{\eta}{b}\right) \qquad \textbf{(5.8)}$$

Multiplying Eq. (5.8) for the LG beam in the plane $z = 0$ the field U_0 emerging from the aperture is obtained. By substituting it into Eq. (5.7) and performing numerical integration, the far-field diffracted intensity pattern is found. Some results are shown in Fig. 5.8, 5.9 and 5.10 where the diffraction patterns for different values and sign of the topological charge are numerically calculated.
In these figures are respectively considered cases of topological charge equal to 2, -2 and 3. It can be easily observed that there is no more bending in the fringes, and that the trajectory of the intensity maxima follows what was already observed in the vertically infinite narrow slit discussed before.

The numerical model based on transmission functions adopted in this chapter, allowed to test a simple techniques for measuring magnitude and sign of even large topological charge optical vortices. Its simplicity relies on the well-known diffraction experiment of single slit diffraction, hence it does not require particular care to be performed. Furthermore, numerical simulations showed that better results can be obtained if a rectangular aperture is used. Although the technique of diffraction by apertures was already studied (using different geometries), the dynamic method proposed in this chapter allows to measure not only the magnitude, but also the sign of topological charge.

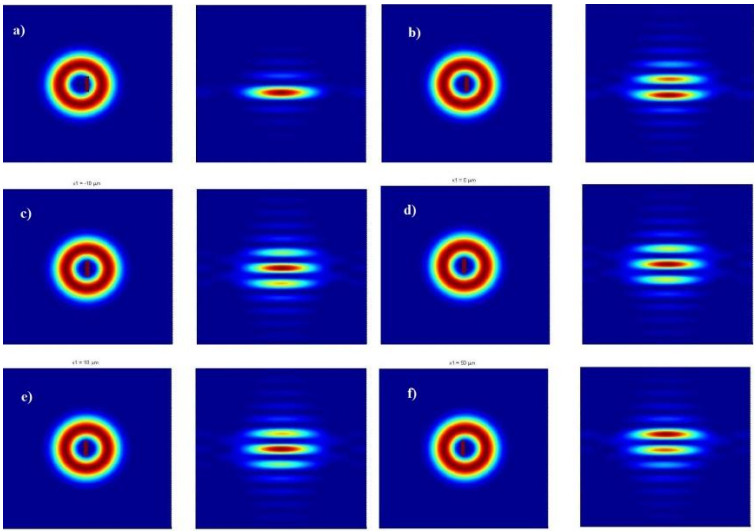

Figure 5.8. Incident field and slit position (left column) and calculated far field pattern (right column), obtained from diffraction by a rectangular aperture sliding in the horizontal direction. The aperture is illuminated by a vortex beam with topological charge Q = 2. Phase uniformity avoids bending of the fringes. As the slit moves from left to right, the fringes move from the bottom to the upper side of the screen. a) ξ_0 = -150μm; b) ξ_0 = -50μm; c) ξ_0 = -10μm; d) ξ_0 = 0μm; e) ξ_0 = 10μm; f) ξ_0 = 50μm.

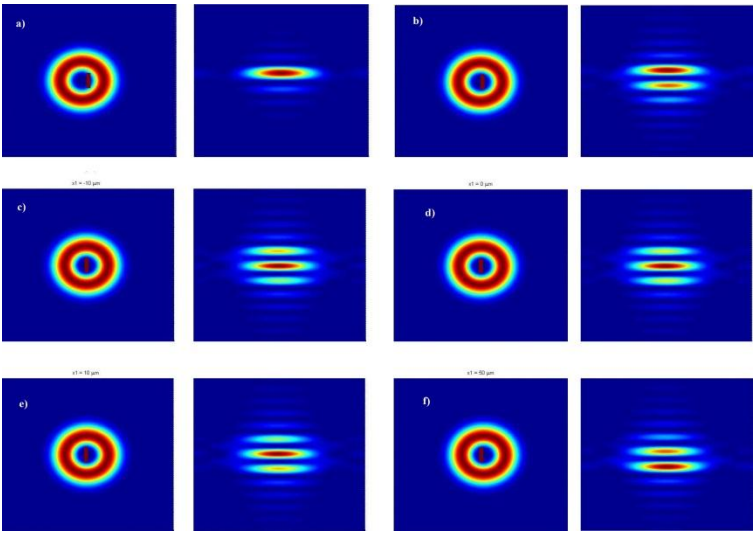

Figure 5.9. Incident field and slit position (left column) and calculated far field pattern (right column), obtained from diffraction by a rectangular aperture sliding in the horizontal direction. The aperture is illuminated by a vortex beam with topological charge Q = -2. Phase uniformity avoids bending of the fringes. As the slit moves from left to right, the fringes move from the upper to the lower side of the screen. a) ξ_0 = -150μm; b) ξ_0 = -50μm; c) ξ_0 = -10μm; d) ξ_0 = 0μm; e) ξ_0 = 10μm; f) ξ_0 = 50μm.

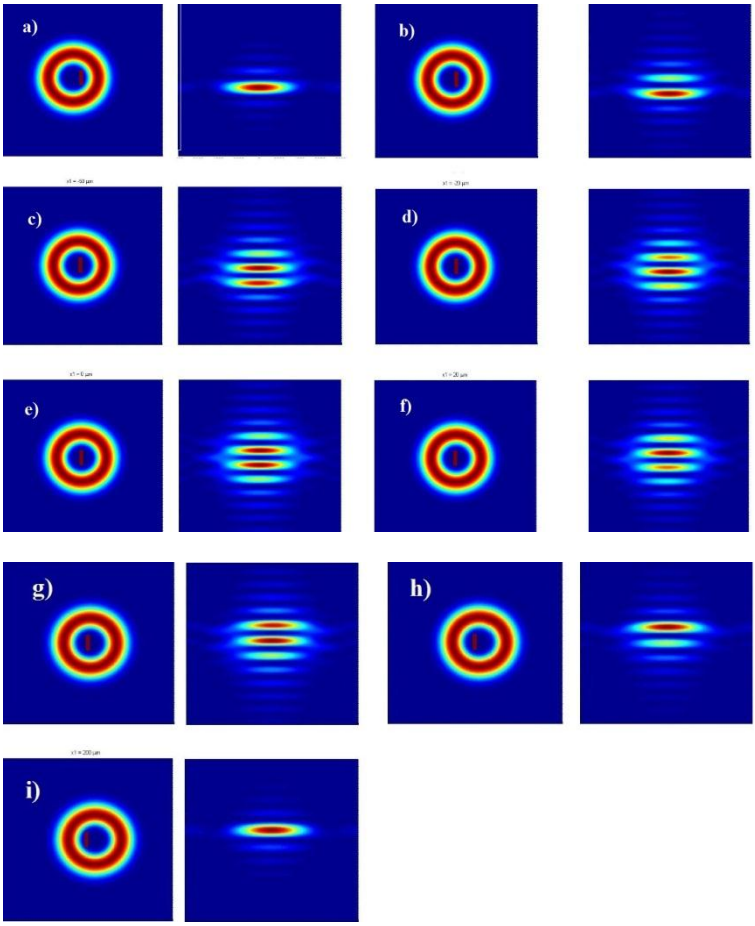

Figure 5.9. Incident field and slit position (left column) and calculated far field pattern (right column), obtained from diffraction by a rectangular aperture sliding in the horizontal direction. The aperture is illuminated by a vortex beam with topological charge Q = 3. Phase uniformity avoids bending of the fringes. As the slit moves from left to right, the fringes move from the lower to the upper side of the screen. a) ξ_0 = -200μm; b) ξ_0 = -100μm; c) ξ_0 = -50μm; d) ξ_0 = -20μm; e) ξ_0 = 0μm; f) ξ_0 = 20μm.

Part 4

Nonlinear interaction of Optical Vortices

Chapter 6

Nonlinear parametric control of Orbital Angular Momentum

It was pointed out several times in this dissertation that it is important to achieve precise control over the orbital angular momentum of light. As a matter of fact this may be helpful in applications such as optical tweezers where particle manipulation requires accurate control; another important application concerns quantum information, where OAM states are used as a basis for n-dimensional qubits.

Undoubtedly it was done a lot of work concerning this topic, focusing especially on the study of dynamics and linear interactions of optical vortices [83-86]. In fact propagation dynamics were thoroughly investigated, showing many interesting aspects of objects like optical vortices: Indebetouw [83] demonstrated that OV behave like charged particles directly affecting OAM.

It was shown that vortices with topological charges of opposite sign tend to attract one each other during propagation. If their initial distance is sufficiently small they may collide, interfering destructively and hence annihilating each other: this obviously leads to the vanishing of the angular momentum. On the other hand, if topological charges are of the same sign, the vortex distribution remains invariant with the propagation (i.e. the distances among the vortices are conserved) and it simply rotates rigidly as a solid body, as a consequence of OAM. The array also expands or contracts together with the host beam.

The result obtained studying the propagation dynamics led to move the investigation on nonlinear interactions [87-90]. This topic revealed as an interesting tool for controlling the dynamics of optical vortices. As a matter of fact, a wide variety of effects has been analyzed and observed, such as the rising of vortex solitons [91], splitting of solitons [92], and creation and annihilation of vortices due to the interaction of the singularities in nonlinear media by means of the dislocations' dynamics.

Some of the nonlinear processes which affect the propagation dynamics of optical vortices are parametric frequency conversion in quadratic nonlinear media [93].

Among them, second harmonic generation in a collinear scheme was also copiously studied since the beginnings of singular optics. In these papers a purely Laguerre-Gaussian mode was used to illuminate a nonlinear crystal in order to generate a second harmonic field [94-97]. Scope of these works was mainly the demonstration of the conservation of orbital angular momentum in frequency conversion processes. It was indeed observed that a LG_{01} beam which undergoes to second harmonic generation (SHG), doubles its azimuthal index, becoming a LG_{02}, hence its topological charge.

To the writer's knowledge further studies were done on nonlinear interactions, exploring parametric down-conversion processes. It was found that, differently from what happens in SHG processes, in down-conversion OAM is not conserved [98-99].

As it was mentioned before, one of the most intriguing applications of vortex beams' interactions is the possibility of getting control not only on the vortices and their position, but also on the field distribution, hence on the OAM.

In this chapter will be discussed a study done on the behaviour of orbital angular momentum in a seeded second-harmonic process. Aim of this work is to provide a fast and efficient method which allows to tune continuously, at a suitable value, the OAM of a field. This techniques takes advantage of easy-to-control parameters such as intensity of the interacting beams, type and length of the involved nonlinear crystal. In what follows will be presented a detailed analysis of the method, testing it with fields carrying both integer and fractional OAMs. As will be shown below, integer OAM beams are obtained simply by nesting an OV in a Gaussian

beam, while fractional values of OAM are achieved both by impressing in a beam a mixed screw – edge dislocation, or by displacing an integer optical vortex from the propagation axis [23].
Particular attention was dedicated to fractional OAM beams because they play an important role as application to quantum information.
To fully understand the problem, in this chapter a theoretical analytical model will be developed to describe the evolution of OVs in quadratic parametric processes. On the other hand, numerical simulations were performed, using a beam propagation method for solving the coupled nonlinear equations written for the interacting fields. In order to have the clearest view of the situation, both phase matched and non-phase matched interactions are considered. Finally analytical and numerical results are compared.

6.1 Second order parametric processes

Nonlinear optical phenomena occur when the optical properties of a material system are modified by the presence of light, and the response of the system depends in nonlinear manner on the strength of the optical field [100]. It is common knowledge that this feature is accounted by the Polarization P of the material system, that is the dipole moment per unit volume. This term is usually linearly related to the applied field by means of the permittivity ε_0 and of a constant of proportionality known as linear susceptibility, which is indicated by the symbol $\chi^{(1)}$. However, more generally, Polarization can be expanded in a power series, introducing higher order terms (second, third, etc.) which have a nonlinear dependence on the electric field:

$$\tilde{\mathbf{P}}(t) = \varepsilon_0 \left[\chi^{(1)} \tilde{\mathbf{E}}(t) + \chi^{(2)} \tilde{\mathbf{E}}^2(t) + \ldots \right] \equiv \tilde{\mathbf{P}}^{(1)}(t) + \tilde{\mathbf{P}}^{(2)}(t) + \ldots \quad \textbf{(6.1)}$$

Higher order polarization terms are thus related to the electric field by the corresponding order susceptibilities, as $\chi^{(2)}$ and so on. Obviously second order processes depend on the presence of $\chi^{(2)}$ which is a third rank tensor measured in m/V (the inverse of the electric field) and the corresponding

polarization term can be referred as second-order nonlinear polarization $\tilde{P}^{(2)}(t) = \varepsilon_0 \chi^{(2)} \tilde{E}^2(t)$. Usually it is referred to the second-order susceptibility with the symbol $d_{eff} = ½\, \chi^{(2)}$.

Second-order polarization plays the role of a source of different components of the electromagnetic field. This can be easily understood by taking into account Maxwell's Equations and combining them in order to obtain the wave equation which, in this case, becomes a nonlinear wave equation:

$$\nabla^2 \tilde{E} - \frac{n^2}{c^2} \frac{\partial^2 \tilde{E}}{\partial t^2} = \frac{1}{\varepsilon_0 c^2} \frac{\partial^2 \tilde{P}^{(2)}}{\partial t^2} \qquad \textbf{(6.2)}$$

Considering an electric field given by

$$\tilde{E}(t) = E e^{-i\omega t} + c.c \qquad \textbf{(6.3)}$$

if it interacts with a nonlinear crystal with second-order susceptibility $\chi^{(2)}$, a nonlinear polarization term is created, according to Eq. (6.1):

$$\tilde{P}^{(2)}(t) = 2\varepsilon_0 \chi^{(2)} E E^* + \left(\varepsilon_0 \chi^{(2)} E^2 e^{-i2\omega t} + c.c. \right) \qquad \textbf{(6.4)}$$

which has components at different frequencies, one at zero frequency (first term), and one oscillating at double frequency with respect to the incident field (second term). Therefore, looking at Eq. (6.2), it can be noticed that the interaction with the nonlinear crystal causes the generation of a field component at the second-harmonic frequency.

More generally an incident field composed of multiple frequencies can be considered:

$$\tilde{E}(t) = E_1 e^{-i\omega_1 t} + E_2 e^{-i\omega_2 t} + c.c. \qquad \textbf{(6.5)}$$

Analogously to what happened before, the corresponding second-order polarization will be:

$$\tilde{P}^{(2)}(t) = \varepsilon_0 \chi^{(2)} \Big[E_1^2 e^{-2i\omega_1 t} + E_2^2 e^{-i\omega_2 t} + 2E_1 E_2 e^{-i(\omega_1+\omega_2)t} + 2E_1 E_2^* e^{-i(\omega_1-\omega_2)t} + c.c. \Big] + 2\varepsilon_0 \chi^{(2)} \left(E_1 E_1^* + E_2 E_2^* \right) \tag{6.6}$$

Looking at Eq. (6.6) terms at multiple frequencies can be identified. First two terms in the square bracket oscillate at twice the frequency of the incident fields, therefore are related to *Second-Harmonic generation*. The third term has a frequency given by the sum of ω_1 and ω_2: this corresponds to *Sum-Frequency generation*. The frequency of the fourth term is the difference of the two input frequencies, hence the corresponding nonlinear process is called *Difference-Frequency Generation*. The remaining term, outside the square bracket has zero frequency and is called *Optical Rectification*.

Typically when a nonlinear interaction takes place only one of the above processes is enough efficient to generate an appreciable signal. This because the nonlinear polarization can efficiently produce an output signal only if certain phase-matching condition is satisfied. Usually this condition can be satisfied only for a certain frequency. Therefore, since phase matching depends on polarization and on the orientation of the nonlinear crystal, these features must be selected according to the desired generated frequency.

6.2 Difference – frequency generation

In a more general fashion an interacting field, as the one of Eq. (6.5), is a superposition of frequencies, hence, by making explicit the harmonic time dependence, it can be expressed as

$$\tilde{\mathbf{E}}(\mathbf{r},t) = \sum_n \tilde{\mathbf{E}}_n(\mathbf{r},t) = \sum_n \mathbf{E}_n(\mathbf{r}) e^{-i\omega_n t} + c.c. \tag{6.7}$$

This implies that all the quantities related to the electrical field of Eq. (6.7), as linear a nonlinear polarization, are given by a similar superposition. Therefore, by substituting such expressions in the wave Eq. (6.2), a nonlinear wave equation that is valid for each frequency can be obtained:

$$\nabla^2 \mathbf{E}_n(\mathbf{r}) + \frac{\omega_n^2}{c^2}\varepsilon(\omega_n)\mathbf{E}_n(\mathbf{r}) = -\frac{\omega_n^2}{\varepsilon_0 c^2}\mathbf{P}_n^{NL}(\mathbf{r}) \qquad \textbf{(6.8)}$$

In a difference-frequency generation process there is the interaction of fields with three different frequencies, each of them has to satisfy Eq. (6.8). These fields can be considered as plane waves whose amplitudes change as they propagate inside the crystal along the *z* direction. Figure 6.1 shows an outline of the process indicating the interacting fields:

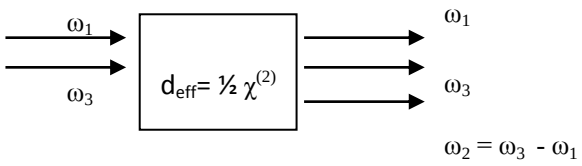

Figure 6.1. Sketch of Difference-frequency generation

Therefore, the involved fields are:

$$\tilde{E}_i(z,t) = A_i(z)e^{i(k_i z - \omega_i t)} + c.c. \qquad \textbf{(6.9)}$$

with i = 1, 2. Field at frequency ω_3 is usually much more intense than the other two: this means that it is substantially unaffected by the energy exchange which happen in the nonlinear interaction. In this situation the second order polarization at the difference-frequency is

$$P_1 = 4\varepsilon_0 d_{eff} E_3 E_2^* \qquad P_2 = 4\varepsilon_0 d_{eff} E_3 E_1^* \tag{6.10}$$

By substituting Eqs. (6.9) and (6.10) into Eq. (6.8), after some algebraic passages, and under the hypothesis that the amplitudes of the interacting fields vary slowly (Slowly Varying Envelope Approximation, SVEA), the coupled equations describing difference frequency generation are obtained.

$$\frac{dA_1}{dz} = \frac{2i\omega_1^2 d_{eff}}{k_1 c^2} A_3 A_2^* e^{i\Delta kz} \qquad \frac{dA_2}{dz} = \frac{2i\omega_2^2 d_{eff}}{k_2 c^2} A_3 A_1^* e^{i\Delta kz} \tag{6.11}$$

where

$$\Delta k = k_3 - k_1 - k_2 \tag{6.12}$$

is the momentum mismatch and is related to the phase matching condition: when phase matching is fulfilled this term is zero. Supposing that phase matching condition is verified, these equations can easily be de-coupled by substituting one into the other, hence leading to the following equation

$$\frac{d^2 A_2}{dz^2} = \frac{4\omega_1^2 \omega_2^2 d_{eff}^2}{k_1 k_2 c^4} A_3 A_3^* A_2 \equiv \kappa^2 A_2 \tag{6.13}$$

Since κ is a real constant, the solution of this equation is a superposition of hyperbolic functions

$$A_2(z) = B\sinh(\kappa z) + C\cosh(\kappa z) \tag{6.14}$$

where B and C are integration constants depending on the boundary conditions. Typically the difference-frequency field is not present at the input plane of the nonlinear crystal, hence $A_2(0)$ can be taken as 0, while a suitable input value can be chosen for A_1. Solution for both field can thus be found as:

$$\begin{aligned} A_1(z) &= A_{10}\cosh(\kappa z) \\ A_2(z) &= i\sqrt{\frac{n_1\omega_2}{n_2\omega_1}}\frac{A_3}{|A_3|}A_{10}^{*}\sinh(\kappa z) \end{aligned} \qquad \textbf{(6.15)}$$

Which are both exponentially growing function. From Eq. (6.15) can be noticed that E_1 always undergoes to amplification while E_2 is amplified with a phase dependent on the phases of the other interacting fields.
There can exist a particular case where frequencies ω_1 and ω_2 are equal: this degenerate case is a down-conversion interaction which can be interpreted as the reverse of the second harmonic generation process. Normally in this situation it is not possible to write separate equations for the fields, unless the degeneration is removed by making the field distinguishable, for example by polarization.

6.3 Composition of fields with different orbital angular momentum

Recalling what was said in chapter 2 about the orbital angular momentum, a linearly polarized field with a helical phase dependence, possess only OAM. For convenience Eq. (2.15) expressing the OAM per photon of a light beam, calculated with respect to the propagation axis *z*, is reported

$$\hbar\ell = \frac{\iint u^{*}(r,\theta)\frac{\hbar}{i}\frac{\partial}{\partial\theta}u(r,\theta)\,r\,dr\,d\theta}{\iint |u(r,\theta)|^{2}\,r\,dr\,d\theta} \equiv \frac{L}{W} \qquad \textbf{(6.16)}$$

where the nature of the terms of the ratio is emphasized. As a matter of fact, OAM per photon is obtained by dividing the total (orbital) angular momentum L, related to the spatial distribution, by the field's energy W. This distinction may be helpful for calculating the OAM of a linear superposition of two or more fields.
In particular, it can be taken into account the case of a field obtained by the sum of two beams carrying different angular momentum $\ell_1 = l$ and $\ell_2 = m$, with the following spatial distribution:

$$u(\rho,\varphi) \propto \mathcal{A}_1 e^{il\varphi} - i\mathcal{A}_2 e^{im\varphi} \qquad \textbf{(6.17)}$$

Such a field configuration was chosen by looking at the results obtained in the previous paragraph, considering a composition of fields involved in a parametric amplification process. However this will become clearer in the following sections.
In order to evaluate the OAM per photon, in ħ units, corresponding to the superposition field of Eq. (6.17), the latter must be substituted in Eq. (6.16). Indicating with L_1, W_1 and L_2, W_2 respectively the total orbital angular momentum and the energy of the fields u_1 and u_2, after simple algebraic passages an expression for the total OAM per photon can be obtained:

$$\ell = \frac{L_1 + L_2 + \mathcal{A}_1\mathcal{A}_2\left(me^{i\pi(m-l)} - le^{i\pi(m-l)}\right)\dfrac{\sin\left[\pi(m-l)\right]}{(m-l)}}{W_1 + W_2 + 2|\mathcal{A}_1||\mathcal{A}_2|\dfrac{\sin^2\left[\pi(m-l)\right]}{(m-l)}} \qquad \textbf{(6.18)}$$

Equation (6.18) is quite difficult to handle and does not provide a simple analytical expression of the total OAM per photon in terms of the angular momentum of the composing fields. However some consideration can be done, in order to drastically simplify it.
As a matter of fact the terms on the right side of Eq. (6.18) show a *sinc* function dependence with the difference (m-l) as argument. It can be noticed that, in particular cases when l and m assume integer values or

when $m = l$ (i.e. the argument of the *sinc* is 0), these terms vanish and the OAM depend only on the total angular momentum and energy of the separate composing fields. Under these circumstances Eq. (6.18) can be re-written as

$$\ell = \frac{L_1 + L_2}{W_1 + W_2} \tag{6.19}$$

Therefore total OAM per photon of a superposition of fields is given by the weighted summation (in terms of energy) of the OAM of the composing fields. As a matter of fact, when fields u_1 and u_2 have the same amplitude the OAM corresponding to their superposition is the arithmetical average, that is $(\ell_1 + \ell_2)/2$; on the contrary, when one of the beams is far more intense than the other, the overall OAM reduces to the angular momentum of the dominant field. As mentioned before, the result expressed by Eq. (6.19) will be applied in the next paragraph to determine the OAM of fields interacting in a nonlinear parametric process.

What was found until now can be easily applied to superposition of optical vortices. In section 2.3 it was pointed out that every field distribution can be expressed by means of a superposition of Laguerre-Gaussian modes, since the constitute an orthonormal basis, as expressed by Eq. (2.23), reported here below.

$$u(r,\theta,z) = \sum_{p=0}^{\infty} \sum_{l=-\infty}^{\infty} C_{pl} \psi_{p,l}^{LG}(r,\theta,z) \tag{6.20}$$

This means that each integer OAM state is orthogonal, hence can be treated as separate from other OAM states. Moreover, Eq. (6.20) allows to include in this analysis even fractional OAMs since they are superposition of integer values.

Clearly this analytical treatise can be extended to superposition of whichever number of fields carrying OAM; the hypotheses made for obtaining Eq. (6.19) retain their validity also for fractional values.

6.4 Seeded Second-Harmonic Generation

Using second order nonlinear processes for controlling light reveals as a powerful tool, and is a valid alternative to intensity dependent changes induced in cubic nonlinear material [101-102] for at least two reasons: speed, and, primarily, because of low-loss properties, in contrast with third-order processes. As a matter of fact third-order interactions take advantage of the nonlinear susceptibility $\chi^{(3)}$ which is typically smaller than second order susceptibility, therefore the related processes may be far less efficient. The possibility of lossless operation is attractive, because it can help to revive the idea of fast control of light-by-light for all optical signal processing. A large number of devices exploiting these phenomena have been proposed; among them, for example, in Ref. [103] was discussed a way of controlling the reflectivity of a field at fundamental frequency (FF) under conditions of a second harmonic (SH) beam far more intense than the FF, and under suitable phase matching conditions.

Vortex dynamics in presence of phase screw dislocations in a beam together with nonlinear interaction, have been also studied. In reference [90] a parametric interaction in a quadratic nonlinear medium has been reported under the fundamental field weak depletion regime; it has been shown that, by changing the relative amplitude and phases of the fields at the input plane of the nonlinear crystal, a control of the vortex dynamic can be performed. However from here emerges that this research was focused only on OV's dynamics, but nothing is reported about the control of OAM carried by each beam.

Scope of this work is to show the evolution of the orbital angular momentum of fields propagating in a nonlinear crystal, interacting in a seeded second harmonic generation process. While in normal second harmonic generation interactions there is only a pump field at FF which is incident on the nonlinear crystal, in seeded SHG both the FF and SH beams are present at the input interface of the crystal. This transforms the nonlinear interaction in a parametric amplification process where, depending on the initial phase of the involved fields, amplification or de-amplification can occur.

Nevertheless the case discussed in this dissertation can be more properly treated as parametric down conversion, since an un-depleted pump beam (i.e. not affected by the interaction) at SH frequency impinges, together with a field at FF, on a second-order nonlinear crystal. Therefore an energy transfer from SH to FF field will be present, modifying the properties of the latter.
In what follows, will be considered a collinear parametric interaction involving fields carrying OAM, both co-propagating in a nonlinear crystal, under two different conditions, i.e. phase-matching and non-phase-matching. The analysis is performed by combining fields, both carrying angular momentum, with different input amplitude, then the more suitable conditions for controlling the OAM carried by the beams is determined.

Considering two fields at the input plane of a $\chi^{(2)}$ nonlinear crystal at frequency ω and 2ω, both of them must satisfy the nonlinear wave equation given by Eq. (6.8). Differently from what was discussed in section 6.2, this time the amplitude of such fields depends both on z and on the transverse coordinate $\mathbf{r} = (\rho,\varphi)$. Therefore they can be written in the form of

$$\tilde{E}_i\left(\mathbf{r},z,t\right) = A_i\left(\mathbf{r},z\right)e^{i\left(k_i z-\omega_i t\right)} + c.c. \qquad \textbf{(6.21)}$$

By substituting Eq. (6.21) into the nonlinear wave equation, a set of coupled equations for the interacting fields is obtained:

$$\begin{aligned} 2ik_1\frac{\partial A_1}{\partial z} + \nabla_T^2 A_1 &= -\frac{2\omega_1^2}{c^2} d_{eff} A_2 A_1^* e^{i\Delta kz} \\ 2ik_2\frac{\partial A_2}{\partial z} + \nabla_T^2 A_2 &= -\frac{\omega_2^2}{c^2} d_{eff} \left|A_1\right|^2 e^{-i\Delta kz} \end{aligned} \qquad \textbf{(6.22)}$$

being

$$k_i^2 = \frac{\varepsilon\left(\omega_i\right)\omega_i^2}{c^2} \qquad i = 1,2 \qquad \textbf{(6.23)}$$

the wavenumber, A_1 and A_2 the complex envelopes of the interacting fields, d_{eff} is the effective coefficient accounting for the nonlinearity, ∇^2_T is the transverse Laplace operator, Δk is the momentum mismatch given by Eq. (6.12), ω_1 and ω_2 are the frequencies of FF and SH fields respectively.

For simplicity's sake, the coupled equations were solved under phase-matching conditions ($\Delta k = 0$). Furthermore, the main hypothesis is that SH field is far more intense than FF: the second harmonic field can thus be treated under the un-depleted approximation, that is A_2 constant with z.

It is possible to account for the OAM by making explicit the helical phase dependence, hence decomposing the complex envelope in a part depending *mainly* on z, and in another with a phase purely depending on the azimuth coordinate φ. Since main interest is on the evolution of OAM, the involved envelopes can be considered as plane waves with a screw phase singularity nested within. Therefore the dependence on the radial coordinate can be neglected, so amplitudes become:

$$\begin{aligned} A_1(\mathbf{r},z) &= \mathcal{A}_1(z,\varphi)u(\rho,\varphi) = \mathcal{A}_1(z,\varphi)e^{il\varphi} \\ A_2(\mathbf{r},z) &= \mathcal{A}_2 u(\rho,\varphi) = \mathcal{A}_2 e^{im\varphi} \end{aligned} \qquad \textbf{(6.24)}$$

Since un-depleted SH field approximation is considered, the set of coupled equations reduces to only the first of Eqs. (6.22) which, by substituting Eqs. (6.24), takes the form of:

$$\frac{\partial \mathcal{A}_1(z,\varphi)}{\partial z} = -i\left[\frac{l^2}{2k_1 r^2}\mathcal{A}_1(z,\varphi) - \frac{2\omega_1}{n_{\omega_1}c}d^{(2)}\mathcal{A}_2\mathcal{A}_1^*(z,\varphi)e^{i(m-2l)\varphi}\right] \qquad \textbf{(6.25)}$$

Equation (6.25) can be solved by separating the real part of $\mathcal{A}_r$ from its imaginary part. After some simple algebraic passages it is found that the solution for the complex envelope of the FF field shows, according to the theory presented in section 6.2, a hyperbolic dependence on the propagation coordinate z.

$$\mathcal{A}_1(z,\varphi) = \mathcal{A}_1(0,\varphi)\cosh\left(\frac{2\omega d^{(2)}|\mathcal{A}_2|}{nc}z\right) + i\mathcal{A}_1^*(0,\varphi)e^{i(m-2l)\varphi}\sinh\left(\frac{2\omega d^{(2)}|\mathcal{A}_2|}{nc}z\right) \quad \textbf{(6.26)}$$

where $\mathcal{A}_1(0,\varphi)$ $\mathcal{A}_2$ constant account for the boundary conditions.
Therefore the complete solution for the field at fundamental frequency becomes:

$$A_1(\mathbf{r},z) = \mathcal{A}_1(0,\varphi)e^{il\varphi}\cosh\left(\frac{2\omega d^{(2)}|\mathcal{A}_2|}{nc}z\right) + i\mathcal{A}_1^*(0,\varphi)e^{i(m-l)\varphi}\sinh\left(\frac{2\omega d^{(2)}|\mathcal{A}_2|}{nc}z\right) \quad \textbf{(6.27)}$$

The OAM of the fundamental field expressed by Eq. (11) can be estimated by making use of what was found in the previous section and expressed by Eq. (6.19), considering the two terms of the envelope of Eq. (6.27) as the fields of the linear superposition of Eq. (6.17). As a matter of fact, by simply looking at Eq. (6.27) to separate contributions to the OAM can be found: these are the terms with helical dependence.
By separately substituting the two terms of the superposition of Eq. (6.27) in Eq. (6.16), the following values can be obtained: the OAM per photon of the first term is *l*, while is *m* – *l* for the second term; since there is no *z* dependence inside such components, clearly their values remain constant during propagation.
As the field propagates inside the crystal, for small values of *z*, the hyperbolic cosine is dominant, as can be seen from Fig. 6.2, hence the overall momentum corresponds with the OAM of the first term of Eq. (6.27), that is *l*, the starting OAM of the field at fundamental frequency. When *z* increases, the second term, proportional to the hyperbolic sine,

grows, tending asymptotically to reach a value comparable with the first term.

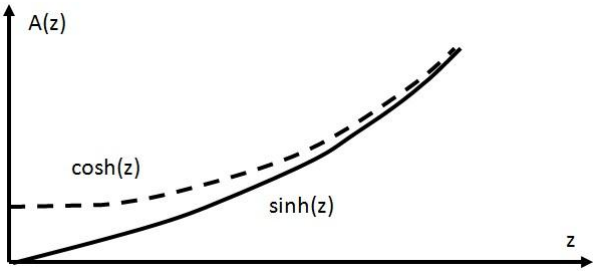

Figure 6.2. Hyperbolic cosine (dashed line) and hyperbolic sine (solid line). For small values of *z* the cosine is dominant. As *z* increases both function tend to a common asymptote.

Therefore, for large propagation distances, the weights of the two contributions become equivalent, and the total OAM per photon is given by half the summation of the two OAMs, i.e. $[l + (m - l)]/2 = m/2$, namely half of the orbital angular momentum of the second harmonic field. This result should not be surprising since momentum conservation must be fulfilled.

Looking at Eq. (6.27) it can be noticed that amplification is strongly dependent on the SH field amplitude which exponentially affect the growth of FF field. This implies that, by changing the input SH intensity, the distance over which the energy of the two OAM contributions becomes equivalent is modified: the higher is the SH amplitude, the shorter is this length.

In Fig. 6.3 is plotted the behaviour of the OAM per photon, in ħ units, of the FF field with the propagation distance *z* for different starting values of the angular momentum of both the SH and FF beams and for different amplitudes of the second harmonic signal. Cases considered include interaction of both integer and fractional values of the OAM per photon. It should be noted that, in order to use Eq. (6.19), that is to simplify Eq. (6.18), when dealing with fractional OAMs same starting values for fundamental and second harmonic fields must be chosen.

It is evident that, regardless of its starting value, the momentum of the FF changes with propagation, in order to match half of the momentum of the SH field.

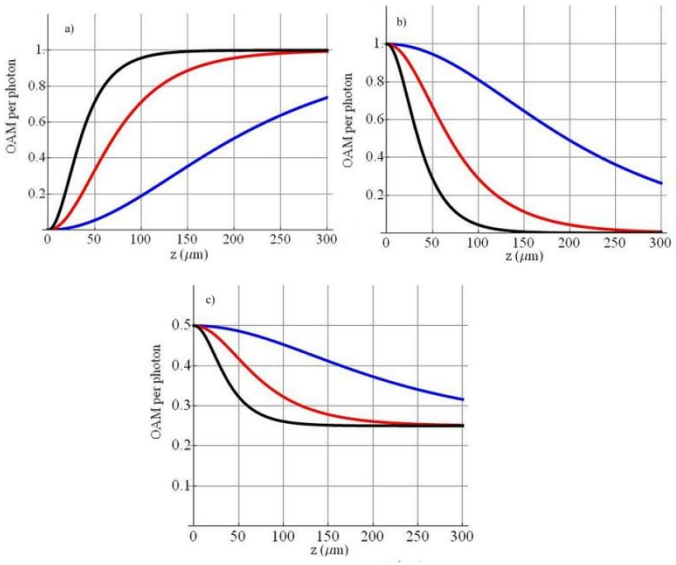

Figure 6.3. OAM per photon of the fundamental field vs. Propagation length inside the nonlinear crystal, for didderent input values of the SH and FF OAMs, and different amplitudes of the SH field; Blue: 7×10^6 V/m, Red: 2×10^7 V/m, Black: 4×10^7 V/m. a) FF with $\ell = 0$, SH with $\ell = 2$; b) FF with $\ell = 1$, SH with $\ell = 0$; c) FF with $\ell = ½$, SH with $\ell = ½$. During the interaction the FF field changes its OAM from its starting value to half the OAM of the SH field.

Looking at Fig. 6.3 can be easily seen that the SH amplitude affects the distance over which FF reaches its final value. Of course such length can be controlled also by changing the nonlinear coefficient, which means changing the nonlinear crystal. Furthermore it is evident that if a crystal is chosen, whose length is smaller than the "regime" length, fundamental frequency fields emerges from the crystal with an intermediate value of OAM.

All these can be considered as parameters on which can be used in order to control the output orbital angular momentum.

6.5 Numerical simulations

6.5.1 Model

In order to verify what was predicted by the analytical solution of the seeded second harmonic generation process discussed in the previous section, numerical simulations were performed, solving the coupled equations (6.22) by means of a beam propagation method. Since an accurate and efficient numerical model is used, integration of Eqs. (6.22) was directly carried out, not considering the un-depleted approximation for the SH field. The only hypothesis taken into account is the Slowly Varying Envelope Approximation, that is field amplitudes do not change abruptly along *z*.

Starting from the nonlinear wave equation, the set of coupled equation (6.22) can be rearranged in a more suitable fashion, writing them in Cartesian coordinates; in this way numerical integration results simpler since a rectangular mesh of spatial samples can easily be defined:

$$\begin{aligned}\frac{\partial A_1(x,y,z)}{\partial z} = & \\ & \frac{i}{2n_b k_0}\frac{\partial^2 A_1(x,y,z)}{\partial x^2} + \frac{i}{2n_b k_0}\frac{\partial^2 A_1(x,y,z)}{\partial y^2} \\ & + \frac{i}{2n_b} k_0 \left[\left(n_\omega^2(x,y,z) - n_b^2 \right) \right. \\ & \left. + 4d^{(2)}(x,y,z) \frac{A_1^*(x,y,z) A_2(x,y,z)}{A_1(x,y,z)} \right] A_1(x,y,z)\end{aligned} \qquad \textbf{(6.28)}$$

$$\frac{\partial A_2(x,y,z)}{\partial z} = \frac{i}{4n_b k_0}\frac{\partial^2 A_2(x,y,z)}{\partial x^2} + \frac{i}{4n_b k_0}\frac{\partial^2 A_2(x,y,z)}{\partial y^2} + i\frac{k_0}{n_b}\left[\left(n_{2\omega}^2(x,y,z) - n_b^2\right) + 2d^{(2)}(x,y,z)\frac{A_1^2(x,y,z)}{A_2(x,y,z)}\right]A_2(x,y,z) \quad \textbf{(6.29)}$$

where ω is the FF field frequency, 2ω is the SH field frequency, $d^{(2)}$ is the nonlinear coefficient, n_ω and $n_{2\omega}$ are respectively the spatial dependent refractive indices at the frequencies ω and 2ω, n_b is the background refractive index, k_0 is the vacuum wave vector and $A_j(x,y,z)$ is the complex envelope of each interaction field.

Last terms in the square brackets of Eqs. (6.28) and (6.29) can be simplified by making explicit the phase dependence of the complex envelope, hence using $A_j = |A_j(x,y,z)|\exp(-i\phi_j(x,y,z))$, being j the index related to each field; in this way, in the first equation, the dependence from the input fields and from their relative phase becomes evident. This is important since, as pointed out before, relative phase between the interacting fields, determines whether an amplification nor de-amplification process occurs.

Looking at Eq. (6.29) it can be noticed that, when the SH input signal is more intense than the FF input beam, the last term in the square brackets is small if compared to the linear part of the equation; therefore the second harmonic field behaves essentially as if non-depletion approximation was considered. On the other hand, in Eq. (6.28), the intense SH signal enhances the nonlinear term, resulting in a strong nonlinear dependence of the FF field on A_2. Moreover a strong relative input phase dependence of the two signals is also expected.

In the numerical analysis carried out in this section, equations (6.28) and (6.29) are solved directly using a beam propagation method, based on a

Fast Fourier Transform (FFT) algorithm with a 200×200 mesh in the transverse plane.

6.5.2 FFT Beam Propagation Method

This numerical scalar tool works under the hypotheses of linear polarization and of main propagation along the *z* axis, with a slowly varying profile along the transverse direction *x*, and along *z*; this means only fields satisfying the paraxial approximation can be simulated.

Starting from the wave equation, applying the SVEA approximation and considering a paraxial field propagating along *z*, of the form $E_y(x,z)=\xi(x,z)e^{in_b k_0 z}$, where ξ is the complex envelope, the following equation can be obtained:

$$\frac{\partial^2\xi(x,y,z)}{\partial x^2}+\frac{\partial^2\xi(x,y,z)}{\partial y^2}+\frac{\partial^2\xi(x,y,z)}{\partial z^2}+2in_b k_0\frac{\partial\xi(x,y,z)}{\partial z} +k_0\left(n^2(x,y,z)-n_b^2\right)\xi(x,y,z)=0 \quad \textbf{(6.30)}$$

Where is emphasized the spatial dependence of the refractive index: this allow to define propagating structures, such as waveguide, rather than homogeneous media. Furthermore, $n(x,y,z)$ must be slowly varying along *z*. Since Eq. (6.30) is a spatial wave equation, it does not allow to study propagation together with reflections; in order to handle reflections, time dependence must be considered.
In order to solve Eq. (6.30) two operators are defined: one, indicated with the symbol $\hat{D}$, includes the spatial derivatives, while the other, identified by $\hat{V}$, is a potential operator which accounts for the refractive index step with respect to the background [104].

$$\hat{D} = \frac{i}{2n_b k_0}\left(\frac{\partial^2}{\partial x^2} + \frac{\partial^2}{\partial y^2}\right); \qquad \hat{\mathrm{V}} = \frac{ik_0}{2n_b}\left(n^2(x,y,z) - n_b^2\right) \textbf{(6.31)}$$

Beam Propagation Method assumes that the field profile at the input plane $\xi(x,y,z_0)$ is known; solving equation (6.30) allows to evaluate the field on the plane $z = z_0 + dz$.

$$\xi(x, z_0 + dz) = e^{(\hat{D}+\hat{V})dz}\xi(x, z_0) \qquad \textbf{(6.32)}$$

Since it is not easy to calculate operators D and V, the exponential term of Eq. (6.32) can be expanded in Taylor series, thus leading to:

$$e^{(\hat{D}+\hat{V})dz} = e^{\hat{V}dz/2}e^{\hat{D}dz}e^{\hat{V}dz/2} + \Theta(dz^3) \qquad \textbf{(6.33)}$$

Observing Eq. (6.33) it can be noticed that the integration step (D+V) has been split into three separate terms: the first accounts for the interaction with the medium by half of the spatial step dz; second term accounts for the free space propagation of a full spatial step; last term covers the interaction with the remaining half spatial step.
At this point, since operator D contains spatial derivatives, it can be evaluated in the Fourier Domain as

$$\tilde{\hat{D}} = \frac{-ik_x^2 - ik_y^2}{2n_b k_0}; \qquad \textbf{(6.34)}$$

This allows to take advantage of the efficiency of Fast Fourier Transform algorithm, since ξ evaluated in the plane $z = z_0 + dz$ becomes

$$\xi(x, y, z_0 + dz) = e^{\hat{V}dz/2}FT^{-1}\left\{e^{\tilde{\hat{D}}dz}FT\left[e^{\hat{V}dz/2}\xi(x, y, z_0)\right]\right\} \qquad \textbf{(6.35)}$$

where FT represents the Fourier Transform which, numerically can be implemented by means of the already mentioned FFT algorithm.
Therefore the BPM work in the following way: the refractive index distribution in the whole space is defined; for each spatial sample of z Eq. (6.35) is integrated using the field distribution evaluated in the previous step.
In order to include in BPM nonlinearities the wave equation can be rewritten as

$$\nabla^2 E_n(x,y,z) + \frac{\omega_n^2}{c^2} n^2(\omega_n) E_n(x,y,z) = -\frac{\omega_n^2}{\varepsilon_0 c^2} P_n^{NL}(x,y,z) \quad \textbf{(6.36)}$$

When considering a second order nonlinear process, such as second harmonic generation the total field can be written as the superposition of the FF and SH fields:

$$\begin{aligned} E &= E_\omega + E_{2\omega} = \\ &\left(\xi_\omega(x,y,z)e^{ik_0 z} + \xi_{2\omega}(x,y,z)e^{i2k_0 z}\right) + c.c. \end{aligned} \quad \textbf{(6.37)}$$

Referring to section 6.2, the nonlinear polarization limited to the SH is given by

$$\begin{aligned} P^{NL}(x,y,z) = 2\varepsilon_0 \Big(& 2d^{(2)}(x,y,z)\xi_\omega^*(x,y,z)\xi_{2\omega}(x,y,z)e^{ik_0 z} \\ & + d^{(2)}(x,y,z)\xi_\omega^2(x,y,z)e^{i2k_0 z}\Big) + c.c. \end{aligned} \quad \textbf{(6.38)}$$

While the linear polarization is

$$P^L(x,y,z) = \varepsilon_0 \varepsilon_\omega E_\omega(x,y,z) + \varepsilon_0 \varepsilon_{2\omega} E_{2\omega}(x,y,z) \quad \textbf{(6.39)}$$

By substituting Eqs. (6.39)-(6.41) into the wave equation (6.38) a set of coupled equations similar to Eqs. (6.28) and (6.29) is obtained. These can

be solved by means of BPM in a way completely analogous to the linear case, provided that operators D and V are correctly defined [105].
As a matter of fact for each step of the propagation length fields at FF and SH are updated, and each of them contributes to the new value of the opposite field.

6.5.3 Input conditions

In all the simulations FF and SH wavelengths are 800nm and 400nm respectively, both propagating collinearly in a type I nonlinear crystal with a nonlinear coefficient $d^{(2)}$ 50pm/V; same effects considered in this analysis can also be obtained by selecting a crystal with different nonlinear coefficient, as BBO or LiNbO3 [106], adjusting the total crystal length and the SH intensity level. Furthermore it is assumed a beam waist for the FF of the order of 10μm, while for the SH is considered the same value reduced of a factor $\sqrt{2}$.
In order to emphasize the role of the intensity of the SH field in controlling the OAM of the FF beam, several simulations were carried out, changing in each one the intensity level of the SH beam and choosing them sufficiently high, with respect to the FF, in order to avoid consistent energy transfers from the fundamental to the second harmonic field.
Moreover three case were investigated in which the fields carry different combinations of OAMs, as happened for Fig. 6.3. in the first situation, at the input plane of the nonlinear crystal, there are FF and SH fields with angular momentum per photon respectively equal to 0 and 2. In the second case, the SH field carries zero angular momentum while the fundamental field has an OAM ℓ = 1and, in the last scenario, both fields carry a fractional orbital angular momentum equal to 0.5.
The first two cases, where interacting fields possess integer OAMS, purely azimuthal Laguerre-Gaussian modes (LG_{0l}) were used; the OAM per photon of such beams is, as pointed out in previous chapters, equal to their azimuthal index l. On the other hand, when dealing with fractional OAMS (third case), the fields are modelled by displacing an integer phase singularity with unitary topological charge from the beam's axis, in order to obtain an angular momentum per photon of 0.5 in ħ units. As a matter of

fact, it can be reminded that reference [23] shows that the intrinsic OAM of a beam with a displaced OV reduces through a Gaussian law with the extents of the displacement: $\ell \propto Q \exp(-2\, r_v^2/w_0^2)$, being r_v the displacement of the singularity, w_0 the spot size and Q the topological charge.

In this dissertation the analysis of the fractional case is limited to the interaction of a FF field and its corresponding collinear SH generated beam; according to the Gaussian dependence of the OAM on the displacement, it can be easily found for a first fundamental field with $\ell = 0.5$ that, because of the momentum conservation, its collinear SH field should possess an OAM of 0.5ħ per photon, that is the same as FF. Therefore this situation is still consistent with the hypothesis of equal fraction OAMs which brought from Eq. (6.18) to Eq. (6.19).

The transverse input beam profiles $u(\rho,\varphi)$ of the FF fields are reported in Fig. 6.4 (first row), together with the corresponding SH input profiles (second row).

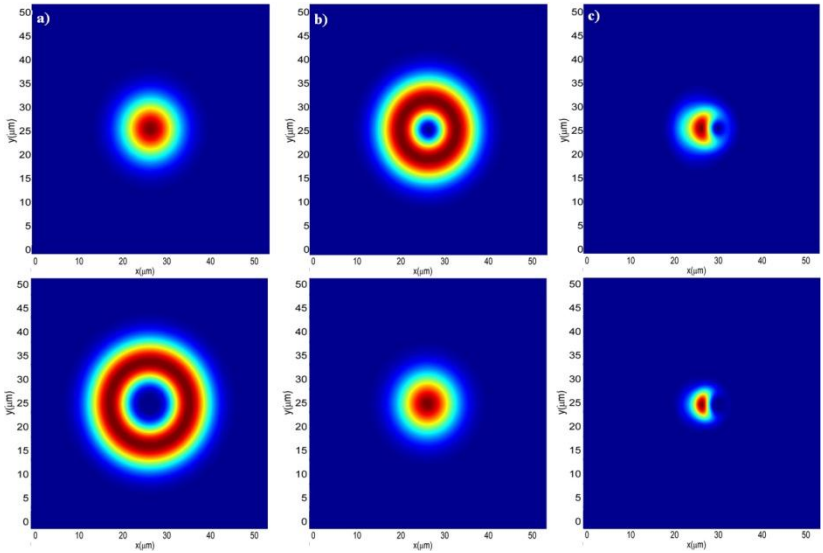

Fig. 6.4. Intensity profiles of the interacting fields at the input plane. First row: FF input beams; second row: SH input beams. a) FF with $\ell = 0$, SH with $\ell = 2$; b) FF with $\ell = 1$, SH with $\ell = 0$; c) FF with $\ell = ½$, SH with $\ell = ½$.

Figure 6.5 shows the phase profiles corresponding to the interacting fields of Fig. 6.4: when OAM is nonzero, the phase winds around a singularity; in Fig. 6.5c can be noticed the displaced optical vortex and the doubled topological charge of its corresponding second harmonic field.

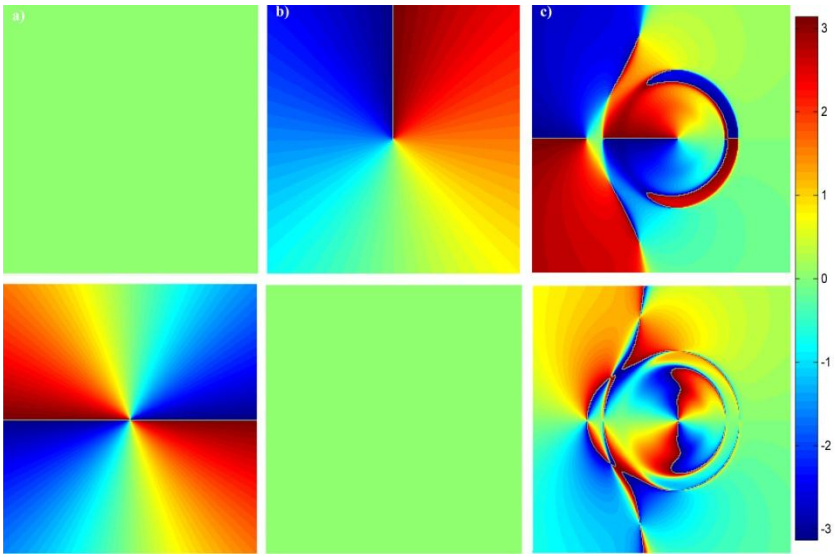

Figure 6.5. Phase profiles of the interacting fields at the input plane. First row: FF input beams; second row: SH input beams. a) FF with $\ell = 0$, SH with $\ell = 2$; b) FF with $\ell = 1$, SH with $\ell = 0$; c) FF with $\ell = ½$, SH with $\ell = ½$.

The off-axis OV beam was modelled via an LG decomposition, using Eq. (6.20); this field was numerically evaluated by integrating the coefficients of the superposition with a 200×200 mesh, over a distance five times larger than the beam waist.

In all of the three situations, the numerically evaluated transverse fields' profiles were propagated in a nonlinear crystal using the FFT BPM to solve Eqs. (6.28) and (6.29). Equation (6.27) predicts that the length over which

the change in OAM happens is strongly dependent on the amplitude of the SH field. Therefore, in order to keep the computational requirements low, i.e. reasonably short propagation distances, simulations were performed by taking both the FF and SH input beams with very high amplitudes, of the order of 10^6V/m to 10^7V/m. clearly it is possible to consider lower intensities (or higher nonlinearities) provided that larger propagation distances, i.e. longer crystals, are chosen.

6.6 Results

Looking at Eqs. (6.28) and (6.29), in phase-matching conditions and with a relative input phase of $-\pi/2$, an amplification process of the FF occurs. In the simulations it was followed the propagation of the fields over a total length of 300μm, with a SH field amplitude ranging from about 10 to100 times higher than the field at fundamental frequency, keeping the propagation away from the spatial soliton threshold.

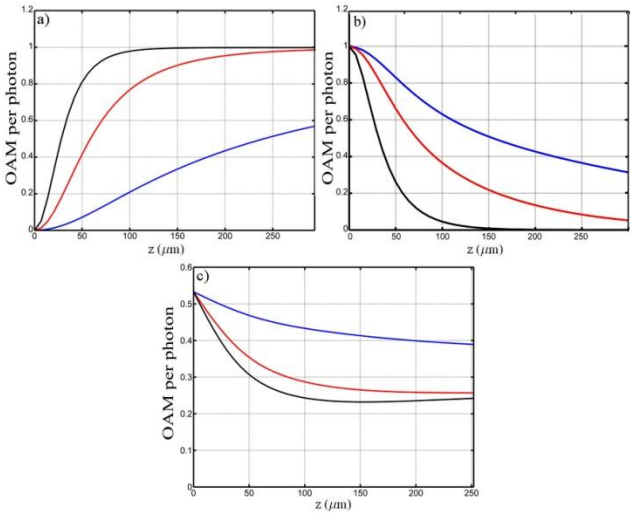

Figure 6.6. OAM per photon (in ħ units) vs. propagation distance in the nonlinear crystal for a FF with an amplitude of 3×10^5V/m and different input amplitudes of the second harmonic field. Blue: 7×10^6V/m, Red: 2×10^7V/m,

Black: 4×10^7V/m. a) FF with $\ell = 0$, SH with $\ell = 2$; b) FF with $\ell = 1$, SH with $\ell = 0$; c) FF with $\ell = ½$, SH with $\ell = ½$.

In Fig. 6.6, similarly to what happened in Fig. 6.3, the value of the fundamental field's OAM per photon, in ħ units, is plotted versus the propagation distance *z*, for different levels of the SH amplitude.

In all the considered cases it can be seen that the OAM of the FF field varies with an hyperbolic dependence on the propagation distance, until it reaches half of the OAM of the second harmonic beam; on the other hand, the momentum of the SH signal remains unaffected, as it was expected.

In fact, the SH input field is such intense to propagate almost un-depleted, even though an energy transfer to the FF field, which undergoes to amplification, happens.

It can be noticed that these results are in perfect agreement with what was predicted in section 6.4 (Fig. 6.3).

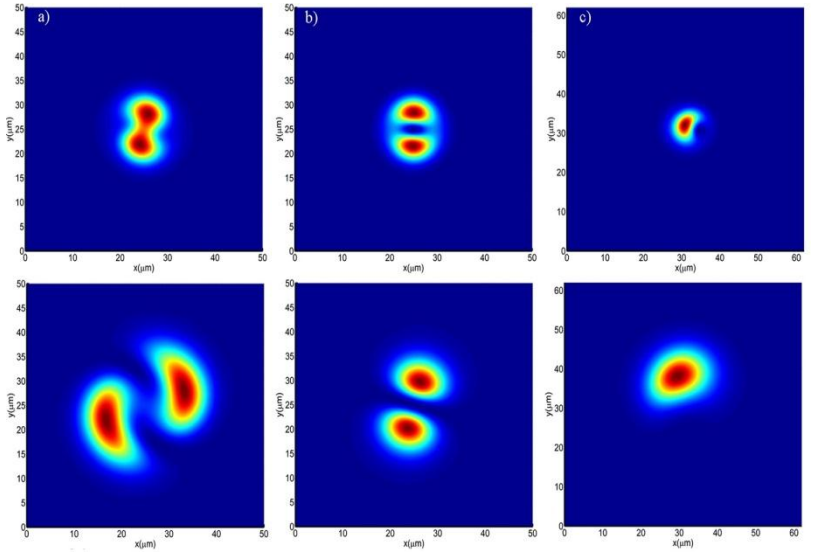

Figure 6.7. Intensity profiles of the three FF fields of Fig. 6.4 after 30μm (first row) and 300μm (second row) of propagation in the nonlinear crystal, with high SH input amplitude: after a suitable propagation length, the OAM per photon of

the FF is half of the SH OAM. As they carry OAM, field profiles rotate with the propagation; rotation is not present when OAM vanishes.

Again, from Fig. 6.6, emerges that the distance over which the value of FF OAM changes, depends on the amplitude level of the SH. Of course higher amplitudes if the SH input field lead to larger amplification of the fundamental beam, with a consequent faster variation of the momentum.
The change in the OAM due to the nonlinear interaction affects also the spatial transverse profile of the FF field. Figures 6.7 and 6.8 show respectively the intensity and phase profiles of the FF fields in the three considered combinations of OAMs, after different distances of propagation; SH field amplitude is taken as 100 times higher than the fundamental field.

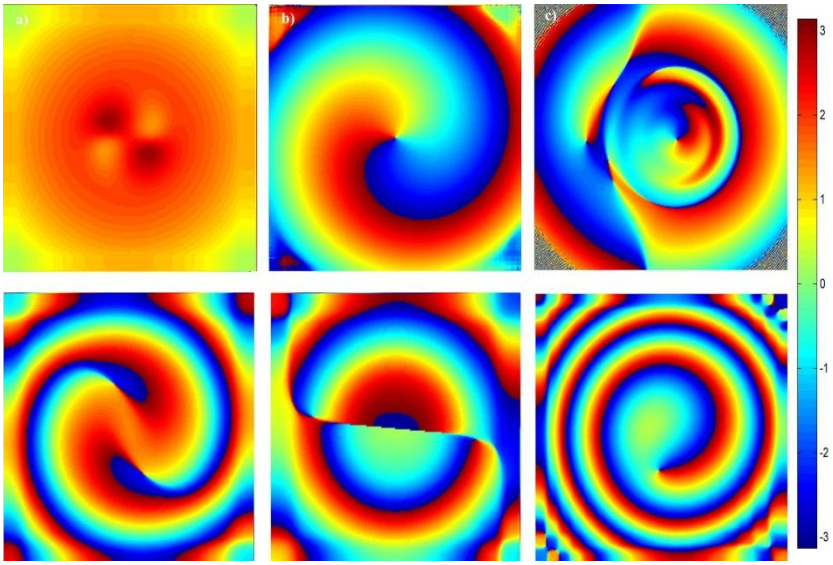

Figure 6.8. Phase profiles of the three FF fields after 30μm (first row) and 300μm (second row) of propagation in the nonlinear crystal, with high SH input amplitude: the OAM is bound to the presence of OVs. In the second case the final OAM is 0, and an edge dislocation is present.

In particular, looking at the second situation, where the final OAM tends to zero, it is possible to notice that the field distribution does not rotate with

the propagation, a typical feature of fields with zero OAM. On the contrary, in the other cases, where the final OAM is different from zero,, the field profile rotates as the propagation distance increases. In these situations the field distribution is found, after 300μm of propagation, rotated of a larger amount with respect to the second case. Looking at Fig. 6.8a it can be noticed that, as the OAM changes from zero to its ending value, OVs are created and, as the field propagates, the phase begins to whirl around the singularities, as also happens in Fig. 6.8c; on the other hand (Fig. 6.8b) a zero ending OAM entails the splitting of the initial vortex distribution and leads to a non-rotating phase profile.

Therefore the effect of the SH field is to modify the propagation length along which the OAM value changes from its starting value to half of the SH OAM. In this way, with a fixed crystal length, by properly choosing the SH intensity level, it is possible to tune the output OAM of the FF field at one of the possible intermediate values between its starting and the ending value.

If a non-phase-matched process is considered (in this case a coherence length of 1μm was selected, taking $n_\omega = 2.7$ and $n_{2\omega} = 2.9$) the behaviour of the FF field distribution is rather different from the phase-matched case.

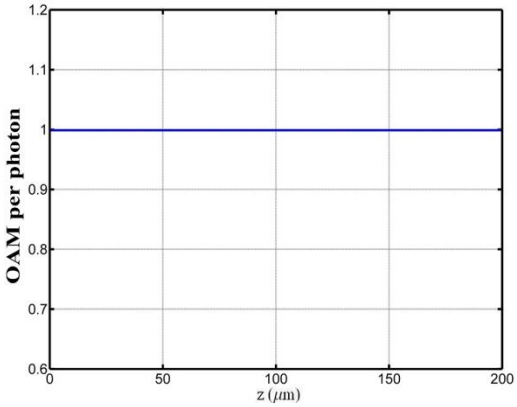

Figure 6.9. OAM per photon (in ħ units) of the FF and SH fields when $\ell_{FF} = 1$ and $\ell_{SH} = 0$: the OAM of the FF field remains constant during the propagation.

Figure 6.9 shows the evolution of the OAM versus the propagation length in non-phase-matching conditions: the behaviour of the fields in the nonlinear interaction is independent on the initial phase difference between the FF and SH beams and, as is shown in Fig. 6.9 for the case of FF with unitary OAM, the orbital angular momentum of the fundamental field is held constant during the propagation.

A parametric process of seeded second harmonic generation has been analyzed both analytically and numerically. Comparing Figs. 6.3 and 6.6 perfect agreement between numerical simulations and theoretical model can be observed. It was demonstrated that, as the interaction takes place, the orbital angular momentum of the field at FF frequency changes, tending to reach half of the SH OAM over a distance controlled by the amplitude of the SH beam [105].

Therefore, using a seeded second harmonic phase-matched interaction, it is possible to reach a fast and efficient control of the orbital angular momentum of a field at fundamental frequency, by simply changing the momentum of the input SH field and operating on a parameter such as the input fields' amplitude.

Chapter 7

Off-axis optical vortices in a noncollinear Second Harmonic Generation Process

Recalling what was said in the previous chapter, propagation dynamics of optical vortices offer an interesting tool, useful for obtaining control over the orbital angular momentum.

Among nonlinear optical interactions, undoubtedly second order interactions, such as second-harmonic generation and parametric processes concerning fields carrying optical vortices have attracted interest because the grant a flexible possibility of manipulating the dynamics of the phase singularities [93-99]. This means that, together with the frequency doubling, the SH-generated field shows phase defects correlated to the ones present in the pump beam. Properties of orbital angular momentum in nonlinear interactions of OV beams have been widely investigated both in parametric processes, such as down-conversion and parametric amplification, as described in Chapter 6, and in collinear second harmonic generation. Studies on the latter were mainly focused on experimental schemes where an *on-axis vortex pump beam* impinged on a quadratic nonlinear crystal. In Ref. [97], collinear SHG was studied using as pump field, Laguerre-Gaussian beams. It was shown that the second harmonic field generated from a purely azimuthal LG mode of the kind LG_{0n} (n is an integer), doubles its OAM, thus verifying momentum conservation. As a matter of fact, a purely azimuthal LG beam has an helical phase

dependence exp($in\theta$); under first order approximation, SH generated field can be considered, as suggested in paragraph 6.1, as proportional to the square of the incident electric field. Therefore can be easily verified that the squared azimuthal dependence becomes exp($i2n\theta$), hence doubling the topological charge and, as a consequence, the orbital angular momentum.
However, *there are no studies on non-collinear SHG schemes especially involving beams carrying fractional OAMs per photon*, and only little attention was placed on parametric processes with field with off-axis vortices nested [90].
In this chapter an experiment of non-collinear second-harmonic generation will be presented, where two pulsed femtosecond input beams, at the first fundamental frequency of 830nm, carrying a fraction OAM, impinge on a Type I nonlinear BBO crystal [100]. The non-integer angular momentum is obtained by means of a fractional spiral phase plate (SPP) [45], which impresses on the incident field a mixed screw-edge dislocation; the latter is then displaced from the beam's axis. The interacting beams are chosen so that they impinge on the nonlinear crystal with opposite OAM, in a "specular "configuration. It will be shown that the resulting second-harmonic field have always a zero angular momentum, even though the spatial profile can be different from case to case.

7.1 Half-integer orbital angular momentum

During this dissertation, it was pointed out several times that OAM states constitutes an orthonormal basis which can be used for representing with infinite degrees of freedom superposition states of light. Therefore OAM offers a multidimensional basis also for representing the quantum of information, thus overcoming the limit to which qubits are subjected. As a matter of fact, qubits are referred to polarization states which constitute a two dimensional space. Preparing a state of the electromagnetic field given by a superposition of n-dimensional states, allows to obtain a quNit, that is a N dimension quantum of information [8, 106].
From here the importance of studying nonlinear interactions of fractional OAM beams, since they are the most evident example of superposition states of the orbital angular momentum.

As mentioned before, fractional beams can be obtained by displacing a screw phase singularity from the beam's axis. It is worth to remind that when displacement happens, particular care should be used about the calculation of the OAM. In fact, the relevant quantity is the intrinsic OAM, i.e. not dependent on the choice of the axis. This can be calculated by properly choosing a reference frame that guarantees a zero transverse momentum [25]. When dealing with off-axis vortices, the choice of the *z* axis as reference for calculating OAM, is not so obvious: the right choice should be fixing the origin in the centre of mass of the vortex beam. However the vorticity is introduced by the singular optical device (SPP, hologram, etc.) into the field, which generally is a Gaussian beam. Hence it is possible to choose the *z* axis parallel to the propagation axis of the beam, and to place the origin at the centre of the beam in the near field [23].
In this way, following a general treatment, the angular momentum density can be defined as usual and the OAM per photon is again given by the expression of Eq. (6.16).

In the following, a situation where a Gaussian beam illuminates the centre of a spiral phase plate that impresses on the field an OAM per photon $\ell = 0.5$ (in ħ units) is considered. The beam's propagation axis coincides with the optical axis of the device. As pointed out before, in this situation, in the beam is nested a mixed screw-edge dislocation. It is possible to represent the field produced by such a SPP via the decomposition of Eq. (6.20). This modal expansion allows also to simply calculate the OAM with respect to the *z* axis as expressed by Eq. (2.25) reported below.

$$\ell = \sum_{p=0}^{\infty} \sum_{l=-\infty}^{\infty} l \left| C_{p,l} \right|^2 \qquad \textbf{(7.1)}$$

Oemrawsingh *et al.* [23] observed that, displacing a fork hologram from the beam's axis, would result in a decrement of the OAM of the field. In a very similar fashion, the OAM can be tuned by moving an SPP off the axis: the momentum obtained from the fractional SPP can be varied between ½ and 0, by means of the displacement of the SPP itself. The output momentum thus results smaller, following the Gaussian law predicted in

Ref. [25]: $\ell \propto Q \exp(-2\ r_v^2/w_0^2)$, where Q is the topological charge impressed by the device, r_v is the extent of the displacement, and w_0 is the spot size of the incident beam. In this way the OAM can be tuned to a well-defined value. The decomposition of Eqs. (6.20) and (7.1) are still valid to model an off-axis dislocation and to evaluate its OAM.

7.2 Non-collinear Second-Harmonic Generation

7.2.1 Experiment

In this work is considered a non-collinear SHG scheme in which two fraction helical beams generated by an SPP impinge with opposite OAMs on a nonlinear crystal (Type I BBO) with small angles of incidence.

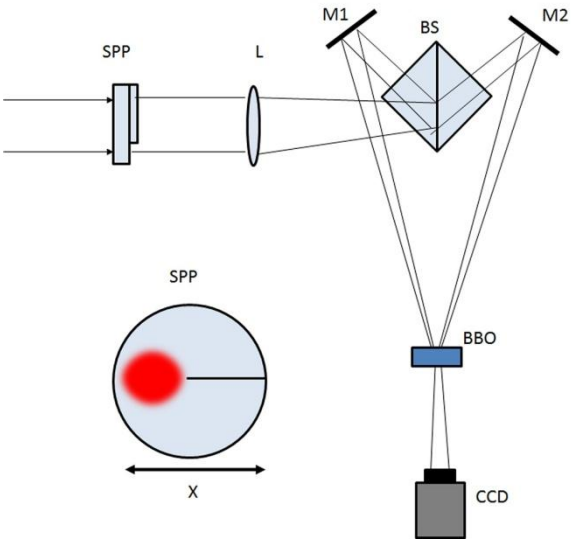

Figure 7.1. Experimental setup of non-collinear SHG. The collimated beam impinges on the SPP, and then is split and focused on the nonlinear crystal, impinging on it with relative angles of ±3.5° (total 7°). In the bottom left corner is illustrated the scan of the Gaussian beam performed by moving the SPP in the horizontal direction.

If the incidence angle is small enough, under a first-order approximation, this scheme can be treated similarly to a collinear scheme. Therefore a scalar model can be adopted for modelling the involved fields; in this case these are considered to fulfil the paraxial approximation.

The nonlinear interaction generates a second-harmonic signal carrying information on the input phase's dislocations. The evolution of the SH field' spatial distribution was followed as the SPP is displaced from the beam's axis. At the same time the OAM of the generated beam was evaluated. Subsequently the experimental results were compared with the numerical simulations performed using the modal expansion of Eq. (6.20).

Figure 7.1 shows the experimental setup for the non-collinear SHG interaction, together with the one used for displacing the SPP (inset).

In the experiment, the output of a mode-locked femtosecond Ti:sapphire laser system, tuned at λ = 830 nm with 76 MHz repetition rate and 130fs of pulse width, is collimated by a telescope, and spatially filtered by means of a 50μm pinhole. The so-prepared laser beam illuminates a spiral phase plate with a spot size of about 500μm. The distance between the lens and the SPP is 50cm, so as the distance from the lens to the BBO crystal. The SPP was designed to operate at a wavelength of 830nm introducing a fractional topological charge, hence an OAM per photon in ħ units of ½.

The centre of the SPP is dominated by the finite size of the height anomaly [44], which is of the order of 50μm; the diameter of the SPP is about 8mm.

The generated vortex beam is then split in two separate beams of about the same intensity. These beams are reflected by mirrors M1 and M2; the tightly focused beams intersect in the focus region with an angle of 7°, with respect to one another, on a BBO crystal 1mm long.

The spiral phase plate is mounted on an *XY* translational stage, in order to perform a full scan of the device. Therefore the plate can be displaced from the beam's propagation axis both in the horizontal and vertical directions, in a 8mm×8mm range, with a 100μm step. Displacing the SPP, causes the horizontal movement (besides the vertical one) of the mixed screw-edge dislocations enclosed in the fields reflected by mirrors M1 and M2, in opposite directions. With the chosen configuration, fields at the FF frequency, impinge on the nonlinear crystal with OAMs of the same magnitude but of opposite signs.

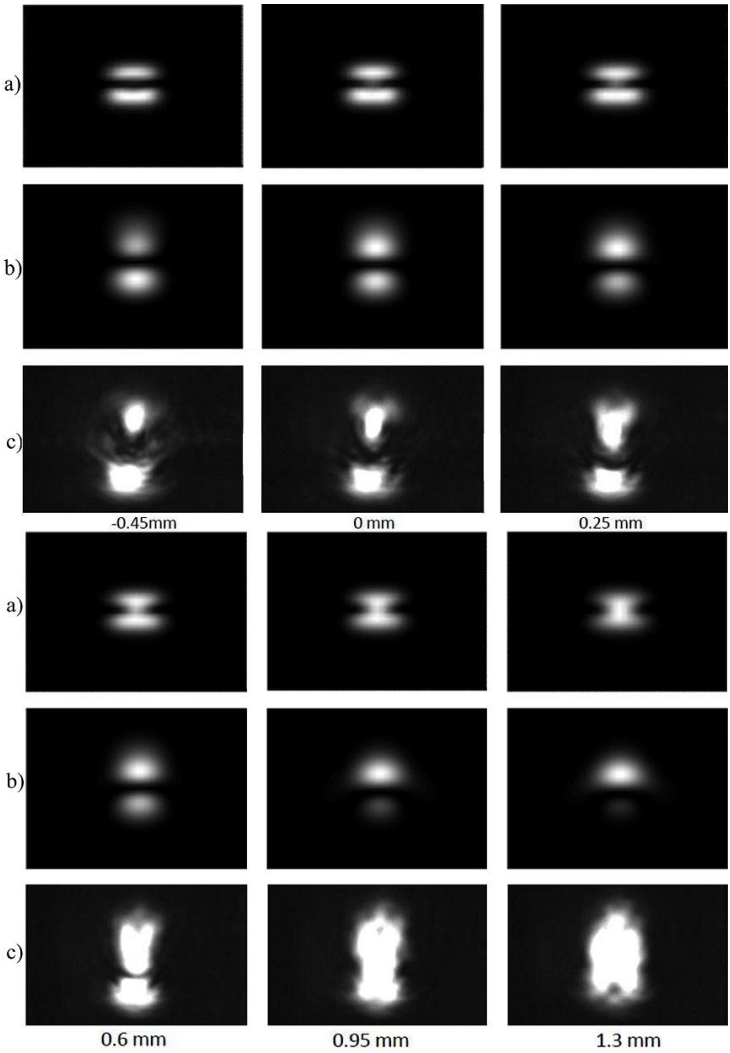

Figure 7.2. Non-collinear SHG signal obtained by displacing the SPP along the x axis at $y = 0$, for six different displacement values. a) Numerically simulated near field profiles; b) numerically simulated far field profiles; c) experimental results.

As a matter of fact, because of the reflections introduces by mirrors M1 and M2, and by the beam splitter, one of the two pump beams experiences an even number of reflections, thus maintaining its initial OAM.
On the contrary the other beam is first transmitted through the beam splitter, then it undergoes only to one reflection by the mirror M2; since OAM is obtained as a cross product, it is a pseudo-vector, hence a symmetry operation, such as reflection, results in a change of sign. Therefore the second pump beam arrives on the nonlinear crystal with an opposite OAM with respect to the other FF beam.
At the output plane of the crystal, the two FF fields come out with their collinear SH signals, propagating with the same angle that they had at the input plane, while the outgoing non-collinear SH signal propagates along the bisector of the total incidence angle. The latter is finally filtered and collected by a CCD camera about 30cm away from the BBO crystal. The non-collinear SHG occurs under Type I phase-matching conditions.
An example of experimental results is shown in Fig. 7.2, where the horizontal displacement of the SPP gives rise to an SH field with different configurations. The experimental results (bottom row) come from the horizontal scan in the central area of the SPP, i.e. for $y = 0$. The upper row is the near-field distribution calculated numerically, and the middle row is the far-field SHG distribution which will be discussed in the next section.
Looking at Fig. 7.2 it can be noticed that a slight difference is present between experimental and numerical results. On the writer's opinion, it can attributed to the finite size of the height anomaly of the SPP which produces a non-perfectly helical beam.
Since interacting fields possess opposite values of OAM, it can be expected that, at the output plane of the crystal, the second-harmonic field carries an orbital angular momentum given by the sum of the OAMs of the pump fields, which therefore should be zero.

7.2.2 Numerical Simulations

Numerical results are obtained by modelling the input fields by means of the modal decomposition of Eq. (6.20). This was used for evaluating the beam profiles both for the on-axis and for the off-axis cases.

Coefficients $C_{p,l}$ were calculated by numerically integrating Eq. (2.24), using rectangular mesh with 200×200 spatial samples. The integration dominion is chosen five times the beam waist, in order to include all the field spatial components.

The near-field shape of the intensity profile of the FF beams is shown in Figs. 7.2a and 7.2b, where the on-axis situation is considered, that is, when the Gaussian beam is located exactly at the centre of the spiral phase plate, thus generating an OAM per photon equal to 0.5ħ.

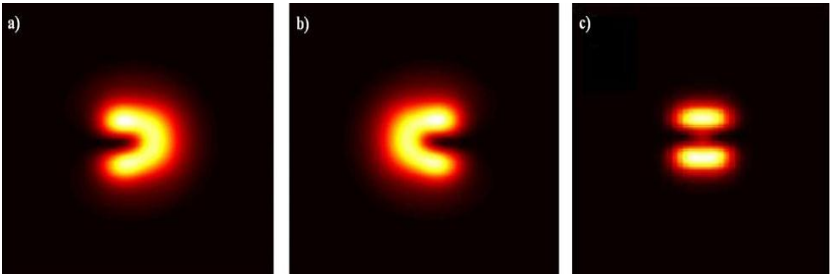

Figure 7.3. Numerically estimated near-field intensity profiles of the FF beams, a) and b), and of the corresponding non-collinear SH beam; in FF beams the singularity shifts in opposite directions. The SH beam's profile carries the singularities of both the FF beams, maintaining their original orientation.

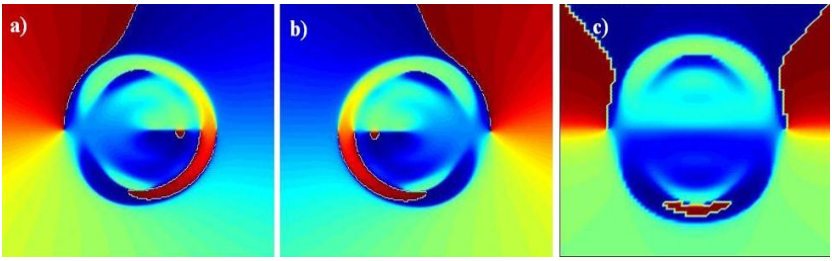

Figure 7.4. Phase plots of the electric field for the FF pump beams, a) and b), and for the SH signal c), corresponding to the configuration of fields given in Fig. 7.3. The phase ranges from 0 (blue) to 2π (red).

Considering a phase-matched interaction, neglecting walk-off, and under paraxial approximation [94, 96], the near-field non-collinear second harmonic intensity is given by

$$I^{2\omega} \approx |E_1^{\omega}(r,\vartheta,z_0)E_2^{\omega}(r,\vartheta,z_0)|^2 \qquad \textbf{(7.2)}$$

where E_1 and E_2 are the two near-field transverse distributions of the input beams. An example of SH's near-field intensity distribution is depicted in Fig. 7.3c, corresponding to the input conditions of Figs. 7.3a and 7.3b.
The phase of the FF and SH fields is shown in Fig. 7.4, where the presence of phase singularities is evident. It can be noticed that the SH signal (Fig. 7.4c) carries both the phase singularities of the incident fields, but with helical phases whirling in opposite directions.
This result, which comes out from the simplistic model adopted in reference [94] is not surprising. As a matter of fact it is widely known that, when a nonlinear interaction takes place, the phases of the interacting input beams are added; hence, the singularities compose in order to cancel each other [83].
In order to perform a comparison among experimental result and numerical modelling, far-field calculations of the second-harmonic signal have been carried out; in this way, still under paraxial approximation, the intensity of the SH field in a plane transverse to the non-collinear SH field's propagation direction is give by

$$I^{2\omega}(x,y,z) \approx \left|\int dr' E_1^{\omega}(x',y',z_0)E_2^{\omega}(x',y',z_0) \times \exp[i\frac{k}{z}(x'x+y'y)]\right|^2 \qquad \textbf{(7.3)}$$

being (x',y') the transverse coordinates on the plane $z = z_0$. Relevant results are shown in Fig. 7.2 (middle row).
For each step of SPP's displacement OAM of the SH generated field was numerically calculated by means of Eq. (6.16). As expected, the OAM of the generated field is conserved, hence producing a beam with an orbital

angular momentum equal to the sum of the individual OAMs of the two input beams: as a consequence, ℓ_{SH} is found to be always 0.
Obviously, since the dislocation is not purely a screw type, in the generated field only the screw components of the singularity cancel, while the edge dislocations of both fields, which do not possess an orientation, remains unaffected, thus creating the nodal lines that can be seen in all the figures above.

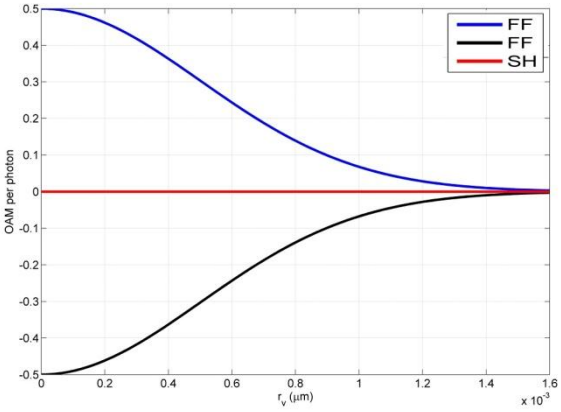

Figure 7.5. OAM of pump and SH fields versus SPP's displacement. As the device is moved from the beam's axis, both the FF beams (blue, upper, and black, lower, lines) reduce the absolute value of their OAM from the initial value that they have when on-axis (±0.5). OAM of the SH field (red, middle, line) is always given by the sum of other two, that is zero.

The behaviour of the OAM of second-harmonic signal, as a function of the SPP's displacement, is depicted in Fig. 7.6, together with the orbital angular momentum of the corresponding interacting pump beams at the fundamental frequency. As pointed out before, the value of the OAM of the SH is always zero, whichever is the displacement, hence regardless of the fundamental field's momentum.
The absence of orbital angular momentum in the generated second-harmonic field can also be emphasized by calculating the Poynting vector

using the transverse part of Eq. (2.11) which, for convenience' sake is reported below

$$\mathbf{P} = \frac{i\varepsilon_0}{\omega}\left(u\nabla_\perp u^* - u^*\nabla_\perp u\right) + 2\frac{k\varepsilon_0}{\omega}|u|^2\,\mathbf{z} \qquad \textbf{(7.4)}$$

The transverse Poynting vector of SH field, obtained when the displacement of the spiral phase plate is zero is shown in Fig. 7.6.

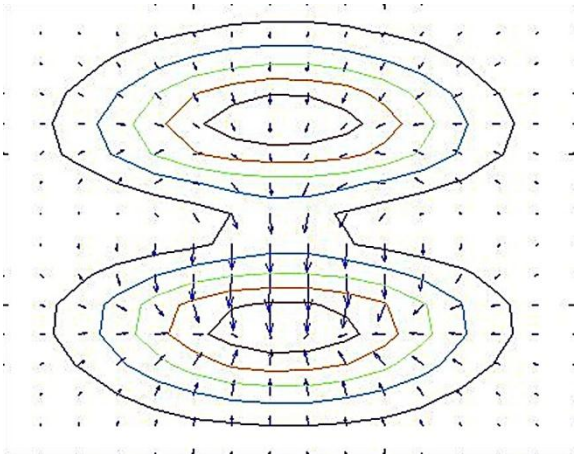

Figure 7.6. Transverse Poynting vector of the SH field generated in the case of on-axis SPP. The absence of rotation of arrows implies that there is no screw dislocation, hence there is no OAM.

From Fig. 7.6 can be observed that the arrows are directed along the linear trajectories entailing the absence of a tangential component of the Poynting vector. Therefore orbital angular momentum is zero.

Aim of this experiment was to investigate the process of non-collinear second harmonic generation involving beams carrying phase singularities generated by a half-integral spiral phase plate. The study focused mainly on the possibility of reaching, starting from fields with a certain OAM,

different spatial configurations, all characterized by the absence of OAM, simply by displacing the spiral phase plate from the beam's axis[107].

Experimental results were obtained performing a transverse scan of the SPP and by letting interact fields with opposite OAMs. These results were then successfully compared to numerical simulations based on a naive model, which validity exists for small incidence angle, and neglecting the walk-off. It was found that the OAM of the generated non-collinear second-harmonic field is always zero and is independent on the extent of the displacement of the SPP. Moreover, the transverse component of the Poynting vector of the SH beam was calculated in order to evidence that the energy of the considered field does not circulate, providing a further evidence of the absence of orbital angular momentum in all the spatial configurations obtained.

Chapter 8

Conclusions

Throughout this PhD thesis the intriguing topic of Orbital Angular Momentum of light was thoroughly analysed on many aspects.
The first part of the dissertation introduced the theoretical basis of the angular momentum. The chapters included in the second part dealt with the generation of optical vortices, hence of the OAM. Two devices (with related patents pending), based on different physical phenomena were proposed.

First was discussed the design of a macroscopic diffractive optical element constituted by a metallic segmented programmable mirror. This device produces helical wave-fronts on an incident beam by means of an azimuthally dependent reflection obtained by means of an azimuthal array of metallic slice whose height is adjusted by actuators. A simple theoretical model, based on a reflectance function, was provided to describe its operating principle. It was shown that, by configuring the mirror into a series of multiple azimuthal ramps higher values of topological charge can be obtained, together with short reconfiguration times. Moreover segments can be programmed in manifold fashions, allowing to produce well-defined spatial profiles of the reflected field. These features make this device suitable both for generating optical vortices, and for generating intensity distributions which can be employed for spatial encoding.

The second proposed device takes advantage of plasmonic interactions to realize a circular array of nanoantennas which allow to generate orbital

angular momentum. Each antenna is made of a sub-wavelength slit etched in a metal layer. Two main operating principles were discussed referring to this device. As a matter of fact it can be used as a spin-to-orbital angular momentum converter: this happens when a circularly polarized incident beam is present on one of the faces of the device. Circular polarization triggers plasmons, activating the nanoantennas with a suitable relative phase retardation of $2\pi/N$. This entails the production of an helical wave-front on the output side, thus generating an optical vortex of unitary topological charge, hence OAM.
At the same time, a step between the edges of the slits can be added on the output side. This makes the antennas to radiate with a tilted angle, hence emitting light field with a non-negligible tangential component of the Poynting vector. As discussed in the introductory chapters, a circular distribution of locally tilted Poynting vectors creates orbital angular momentum. It is worth noting that the OAM generation related to the tilted emission of the nano-light sources can be cumulated with the conversion effect between SAM and OAM, thus allowing to opportunely tune the angular momentum.
This device moves the field of singular optics to the nanoscale, entailing a series of fascinating applications such as micromachining and micro-helixes.

The central part of the thesis is dedicated to the measurement of the topological charge of optical vortices. A simple method based on the diffraction by a single narrow slit is proposed, in order to overcome the limitations connected with the issue of measuring sign and magnitude of the topological charge. It was shown that this method, taking advantage of a sort of tomography of the OV, allows to measure even high values of Q.

Last part of this work dealt with nonlinear processes and how they influence optical vortices dynamics.

First a method to achieve a nonlinear accurate control OAM was proposed. It is based on a parametric amplification process where the angular momentum and the intensity of a second harmonic beam is used as control

parameter to adjust the orbital angular momentum of the field at fundamental frequency. Furthermore an analytical theoretical model was provided in order to investigate superposition of OAM states and their evolution during nonlinear interactions.

Finally an experiment of non-collinear second harmonic generation involving off-axis optical vortices was described. It allowed to understand momentum conservation when dealing with fields carrying non-integer values of the orbital angular momentum. It was shown that, under certain hypotheses, OAM is conserved also in non-collinear processes, regardless of the amount of OAM of the interacting input fields.

All topics and results discussed in this PhD thesis were obtained during three years of research. Most of the issues included in these chapters were presented to the scientific community as journal papers, as well as oral presentations or posters in conferences and PhD schools.
At the time of writing the works related to the proposed devices have patents submitted to the Italian Patent Office; a paper on the helical segmented mirror was also submitted to specialized journal, while the article on the plasmonic spiral phase plate is in preparation.
Both the topics described in chapter 6 and 7 were published respectively on Optics Communications and on the Journal of Optical Society of America B (see Publications list). Finally, on November 2011, the article relative to chapter 7 was reviewed on OSA Spotlight On Optics.

Bibliography

[1] J.F. Nye, M.V. Berry, *Dislocations in wave trains*, Proc. R. Soc. Lond. A. **336**, 165-190 (1974).

[2]K.T. Gahagan, G.A. Swartzlander Jr., *Trapping of low index microparticles in an optical vortex*, JOSA B **15**, 524-534 (1998).

[3] J.E. Molloy, M.J. Padgett, *Lights, action: optical tweezers*, Contemp. Phys. **43**, 241-258 (2002).

[4] Y.S. Kivshar, B.Luther-Davies, *Optical dark solitons: physics and applications*, Phys. Rep. **298,** 81-197 (1998).

[5] G.A. Swartzlander Jr., *Achromatic optical vortex lens*, Opt. Lett. **31**, 2042-2044 (2006) .

[6] G. Foo, D.M. Palacios, G.A. Swartzlander Jr., *Optical Vortex Coronograph*, Opt. Lett. **30**, 3308-3310 (2005).

[7] S.W. Hell, *Far-Field Optical Nanoscopy*, Science **316**, 1153-1158 (2007).

[8]A. Mair, A. Vaziri, G. Wehis, A. Zeilinger, *Entanglement of the orbital angular momentum states of photons*, Nature **412**, 313-316 (2001).

[9] J.C. Maxwell, *Treatise on Electricity and Magnetism*, Oxford (1873).

[10] A. Sadowsky, *Acta et Commentationes Imp. Universitatis Jurievensis* **7**, 1-3 (1899).

[11] J.H. Poynting, *The Wave Motion of a Revolving Shaft, and a Suggestion as to the Angular Momentum in a Beam of Circularly Polarised Light*, Proc. R. Soc. Lond. A **82**, 560-567 (1909).

[12] R.A. Beth, *Mechanical Detection and Measurement of the angular momentum of light*, Phys. Rev. **50**, 115-125 (1939).

[13] J.M. Vaughan, D.V. Willets, *Interference properties of a light beam having a helical wave surface*, Optics Commun. **30**, 263-267 (1979).

[14] L. Allen, M.W. Beijersbergen, R.J.C. Spreeuw, J.P. Woerdman, *Orbital angular momentum of light and the transformation of Laguerre – Gaussian laser modes*, Phys. Rev. A **45**, 8185-8190 (1992).

[15] P. Coullet, L. Gil, F. Rocca, *Optical Vortices*, Opt. Commun. **73**, 403-408 (1989).

[16] M.V. Berry, R.G. Chambers, M.D. Large, C. Upstill, J.C. Walmsley, *Wavefronts dislocations in the Aharonov-Bohm effect and its water wave analogue*, Eur. J. Phys. **1**, 154-162 (1980).

[17] M.V. Berry, *Singularities in waves*, in Les Houches Lecture Series Session XXXV, eds. R. Balian, M. Klaeman, J.P. Poirier, North – Holland: Amsterdam (453-543).

[18] M.S. Soskin, M.V. Vasnetsov, *Singular Optics*, Progr. Opt. **42**, 219-276 (2001).

[19] J.D. Jackson, *Classical Electrodynamics Third Edition*, eds. John Wiley & Sons, New York (1999).

[20] M. Born, E. Wolf, *Principles of Optics 7th edition*, eds. Pergamon, New York (1999).

[21] F. Gori, *Elementi di Ottica*, eds. Accademica, Roma (1995).

[22] L. Allen, M.J. Padgett, M. Babiker, *The Orbital Angular Momentum of Light*, Progr. Opt. **34**, 291-372 (1999).

[23] S.S.R. Oemrawsingh, E.R. Eliel, G. Nienhuis, J.P. Woerdman, *Intrinsic Orbital Angular Momentum of Paraxial Beams with Off-axis Imprinted vortices*, J. Opt. Soc. Am. A **21**, 2089-2096 (2004).

[24] H.A. Haus, *Waves and Fields in Optoelectronics*, eds. Prentice Hall, Englewood Cliffs NJ (1984).

[25] A.T. O'Neil, I. Mac Vicar, L. Allen, M.J. Padgett, *Intrinsic and Extrinsic Nature of the Orbital Angular Momentum of a Light Beam*, Phys. Rev. Lett **88**, 053601-1-4 (2002).

[26] M.V. Berry, *Paraxial Beams of Spinning Light*, Singular Optics **3487** (ed. M.S. Soskin)**,** SPIE proceedings, Fruzenskoe, Crimea, 6-11 (1998).

[27] B.E.A. Saleh, M.C. Teich, *Fundamentals of photonics*, eds. John Wiley & Sons, New York (1991).

[28] O. Svelto, *Principles of Lasers 5th edition*, eds. Springer, New York (2010).

[29] E. Abramochkin, V. Volostnikov, *Beam Transformations and nontransformed beams*, Optics. Commun. **83**, 123-135 (1991).

[30] C. Tamm, C.O. Weiss, *Spontaneous Breaking of Cylindrical Symmetry in an Optically Pumped laser*, Optics Commun. **78**, 253-258 (1990).

[31] M.W. Beijersbergen, L. Allen, H.E.L.O. van der Veen, J.P. Woerdman, *Astigmatic Laser Mode Converters and Transfer of Orbital Angular Momentum*, Optics Commun. **96**, 123-132 (1993).

[32] D. McGloin, N.B. Simpson, M.J. Padgett, *Transfer of Orbital Angular Momentum from a Stressed Fiber Optic Waveguide to a Light Beam*, Appl. Opt. **37**, 469-472 (1998).

[33] I. Basistiy, M.S. Soskin, M.V. Vasnetsov, *Optical Wavefront Dislocations and their Properties*, Optics Commun. **119**, 604-612 (1995).

[34] V.Yu. Bazhenov, M.V. Vasnetsov, M.S. Soskin, *Laser Beams with Screw Dislocations in their Wavefronts*, JETP Lett. **52**, 429-431 (1990).

[35] V. Yu. Bazhenov, M.S. Soskin, M.V. Vasnetsov, *Screw Dislocations in Light Wavefronts*, J. Mod. Opt. **39**, 985-990 (1992).

[36] N.R. Heckenberg, R. McDuff, C.P. Smith, H. Rubinsztein-Dunlop, M.J. Wegener, *Laser Beams with Phase Singularities*, Opt. Quantum Electr. **24**, S951-S952 (1992)

[37] M.W. Beijersbergen, R.P.C. Coerwinkel, M. Kirstensen, J.P. Woerdman, *Helical-wavefront laser beams produced with a spiral phaseplate*, Optics Commun. **112**, 321-327 (1994).

[38] S.S.R. Oemrawsingh, J.A.W. van Houwelingen, E.R. Eliel, J.P. Woerdman, E.J.K. Verstegen, J.G. Kloosterboer, G.W. 't Hooft, *Production and Characterization of Spiral Phase Plates for Optical Wavelength*, Appl. Opt. **43**, 688-694 (2004)

[39] T. Watanabe, M. Fujii, Y. Watanabe, N. Toyama, Y. Iketaki, *Generation of a Doughnut – shaped Beam Using a Spiral Phase Plate*, Rev. Sci. Instrum. **75**, 5131-5135 (2004).

[40] M. Harris, C.A. Hill, P.R. Tapster, J.M. Vaughan, *Laser modes with helical wave fronts*, Phys. Rev. A **49**, 3119-3122 (1994).

[41] W.C. Cheong, W.M. Lee, X.C. Yuan, L.S. Zhang, K. Dholakia, H. Wang, *Direct Electron-beam Writing of Continuous Spiral Phase Plates in Negative Resist with High Power Efficiency for Optical Manipulation*, Appl. Phys. Lett. **85**, 5784-5786 (2004).

[42] J. Chen, D.F. Kuang, M. Gui, Z.L. Fang, *Generation of Optical Vortex Using a Spiral Phase Plate Fabricated in Quartz by Direct Laser Writing and Inductively Coupled Plasma Etching*, Chin. Phys. Lett. **26**, 014202 – 1-3 (2009).

[43] C. Rotschild, S. Zommer, S. Moed, O. Hershovitz, S.G.Lipson, *Adjustable Spiral Phase Plate*, Appl. Opt. **43**, 2397-2399 (2004).

[44] L. Marrucci, C. Manzo, D. Paparo, *Optical Spin-to-Orbital Angular Momentum Conversion in Inhomogeneous Anisotropic Media*, Phys. Rev. Lett. **96**, 163905 - 1-4 (2006).

[45] S.S.R. Oemrawsingh, E.R. Eliel, J.P. Woerdman, E.J.K. Verstegen, J.G. Kloosterboer, G.W. 't Hooft, *Half – integral Spiral Phase Plates for Optical Wavelengths*, J. Opt. A **6**, S288-S290 (2004).

[46] D.P. Ghai, P. Senthilkumaran, R.S. Sirohi, *Adaptive Helical Mirror for Generation of Optical Phase Singularity*, Appl. Opt. **47**, 1378-1383 (2008).

[47] D.P. Ghai, *Generation of optical vortices with an adaptive helical mirror*, Appl. Opt. **50**, 1374-1381 (2011).

[48] R.K. Tyson, M. Scipioni, J. Viegas, *Generation of an Optical Vortex with a Segmented Deformable Mirror*, Appl. Opt. **47**, 6300-6306 (2008).

[49] M. Reicherter, T. Haist, E.U. Wagemann, H.J. Tiziani, *Optical Particle Trapping with Computer – generated Holograms Written on a Liquid - crystal Display*, Opt. Lett. **24**, 608-610 (1999).

[50] G.A. Swartzlander Jr., *The optical vortex lens*, Opt. Photon. News **17**, 39-43 (2006).

[51] A.S. Desyatnikov, Y.S. Kivshar, L. Torner, *Optical vortices and vortex solitons*, Progr. Opt. **47**, 291-391 (2005).

[52] T.W. Ebbesen, H.J. Lezec, H.F. Ghaemi, T. Thio, P.A. Wolff, *Extraordinary optical transmission through sub-wavelength hole arrays*, Nature **931**, 667-669 (1998).

[53] A. Degiron, H.J. Lezec, W.L. Barnes, T.W. Ebbesen, *Effects of hole depth on enhanced light transmission through subwavelength hole arrays*, Appl. Phys. Lett. **81**, 4327-4329 (2002).

[54] H. Fischer, O.J.F. Martin, *Engineering the optical response of plasmonic nanoantennas*, Opt. Express **16**, 9144-9154 (2008).

[55] M. Centini, A. Benedetti, C. Sibilia, M. Bertolotti, *Coupled 2D Ag nano-resonator chains for enhanced and spatially tailored second harmonic generation*, Opt. Express **19**, 8218-8232 (2011).

[56] W. Chen, D.C. Abeysinghe, R.L. Nelson, Q. Zhan, *Plasmonic Lens Made of Multple Concentric Metallic Rings under Radially Polarized Illumination*, Nano Lett. **9**, 4320-4325 (2009).

[57] Z. Liu, J.M. Steele, W. Srituravanich, Y. Pikus, C. Sun, X. Zhang, *Focusing Surface Plasmons with a Plasmonic Lens*, Nano Lett. **5**, 1726-1729 (2005).

[58] H.J. Lezec, T. Thio, *Diffracted evanescent wave model for enhanced and suppressed optical transmission through subwavelength hole arrays*, Opt. Express **12**, 3629-3651 (2004).

[59] P.F. Chimento, G.W. 't Hooft, E.R. Eliel, *Plasmonic tomography of optical vortices*, Opt. Lett. **35**, 3775-3777 (2010).

[60] S.A. Maier, *Plasmonics, fundamentals and applications 1st edition*, Springer, New York (2007).

[61] P. Ginzburg, E. Hirshberg, M. Orenstein, *Rigorous analysis of vectorial plasmonic diffraction: single- and double-slit experiments*, J. Opt. A: Pure Appl. Opt. **11**, 114024 – 1-5 (2009).

[62] L. Martìn-Moreno, F.J. Garcìa-Vidal, H.J. Lezec, K.M. Pellerin, T. Thio, J.B. Pendry, T.W. Ebbesen, *Theory of Extraordinary Optical Transmission through Subwavelength Hole Arrays*, Phys. Rev. Lett. **86**, 1114-1117 (2001).

[63] H. Kim, J. Park, S.W. Cho, S.Y. Lee, M. Kang, B. Lee, *Synthesis and Dynamic Switching of Surface Plasmon Vortices with Plasmonic Vortex Lens*, Nano Lett. **10**, 529-536 (2010).

[64] B. Hecht, H. Bielefeld, L. Novotny, Y. Inouye, D.W. Pohl, *Local excitation, scattering and interference of surface plasmons*, Phys. Rev. Lett **77**, 1889-1892 (1996).

[65] Z. Sun, H.K. Kim, *Refractive transmission of light and beam shaping with metallic nano – optic lenses*, Appl. Phys. Lett. **85**, 642-644 (2004).

[66] A.E. Çetin, A. Sennaroglu, Ö.E. Mustecaplioglu, *Nanoscale plasmonic devices for dynamically controllable beam focusing and scanning*, Phot. Nano. Fund. Appl. **8**, 7-13 (2010).

[67] G. Gerosa, P. Lampariello, *Lezioni di campi elettromagnetici*, Ingegneria 2000, Roma (1995).

[68] E.D. Palik, *Handbook of Optical Constants of Solids*, Academic Press, San Diego (1991).

[69] J. Weiner, *The physics of light transmission through subwavelength apertures and aperture arrays*, Rep. Prog. Phys. **72**, 064401 – 1-19 (2009).

[70] C.P. Huang, Q.J. Wang, Y.Y. Zhu, *Dual effect of surface plasmons in light transmission through perforated metal films*, Phys. Rev. B **75**, 245421 – 1-7 (2007).

[71] M. Righini, G. Volpe, C. Girard, D. Petrov, R. Quidant, *Surface Plasmon Optical Tweezers: Tunable Optical Manipulation in the Femtonewton Range*, Phys. Rev. Lett. **100**, 186804 – 1-4 (2008).

[72] P. Sheng, R.S. Stepleman, P.N. Sanda, *Exact eigenfunctions for square-wave gratings: application to diffraction and surface-plasmon calculations*, Phys. Rev. B **26**, 2907-2916 (1982).

[73] D. Mawet, E. Serabyn, K. Liewer, Ch. Hanot, S. McEldowney, D. Shemo, N. O'Brien, *Optical Vectorial Vortex Coronographs using Liquid Crystal Polymers: theory, manufacturing and laboratory demonstration*, Opt. Express **17**, 1902-1918 (2009).

[74] F.J. Garcìa–Vidal, E. Moreno, J.A. Porto, L. Martìn-Moreno, *Transmission of Light through a Single Rectangular Hole*, Phys. Rev. Lett. **95**, 103901 – 1-4 (2005).

[75] V.S. Volkov, S.I. Bozhevolnyi, S.G. Rodrigo, L. Martìn-Moreno, F.J. Garcìa-Vidal, E. Devaux, T.W. Ebbesen, *Nanofocusing with channel Plasmon polaritons*, Nano Lett. **9**, 1278-1282 (2009).

[76] A. Yariv, *Quantum Electronics 3rd edition*, John Wiley and Sons, New York (1989).

[77] P. Yeh, *Optical waves in layered media*, John Wiley and Sons, New York (1998).

[78] H.I. Stzul, R.R. Alfano, *Double-slit interference with Laguerre-Gaussian beams*, Opt. Lett. **31**, 999-1001 (2006).

[79] C.S. Guo, L.L. Lu, H.T. Wang, *Characterizing topological charge of optical vortices by using an annular aperture*, Opt. Lett. **34**, 3686-3688 (2009).

[80] Y. Liu, J. Pu, *Measuring the orbital angular momentum of elliptical vortex beams by using a slit hexagon aperture*, Optics Comm. **284**, 2424-2429 (2011).

[81] A. Mourka, J. Baumgartl, C. Shanor, K. Dholakia, E.M. Wright, *Visualization of the birth of an optical vortex using diffraction from a triangular aperture*, Opt. Express **19**, 5760-5771 (2011).

[82] D.P. Ghai, P. Senthilkumaran, R.S. Sirohi, *Single-slit diffraction of an optical beam with phase singularity*, Opt. Las. Eng. **47**, 123-126 (2011).

[83] G. Indebetouw, *Optical vortices and their propagation*, J. Mod. Opt. **40**, 73-87 (1993).

[84] F.S. Roux, *Coupling of noncanonical optical* vortices, J. Opt. Soc. Am. B **21**, 664-670 (2004).

[85] F.S. Roux, *Distribution of angular momentum and vortex morphology in optical beams*, Optics Comm. **242**, 45-55 (2004).

[86] D. Rozas, C.T. Law, G.A. Swartzlander Jr, *Propagation dynamics of optical vortices*, J. Opt. Soc. Am. B **14**, 3054-3065 (1997).

[87] J. Scheuer, M. Orenstein, *Optical Vortices Crystals – Spontaneous Generation in Nonlinear Semiconductor Microcavities*, Science **285**, 230-233 (1999).

[88] D.V. Petrov, *Vortex-edge dislocation interaction in second-order nonlinear media*, Optics Comm. **200**, 381-387 (2001)

[89] V. Pyragaite, K. Regelskis, V. Smilgevicius, A. Stabinis, *Noncollinear interaction of optical vortices in Kerr nonlinear medium*, Optics Comm. **198**, 459-464 (2001).

[90] A.P. Sukhorukov, A. Kalinovich, G. Molina-Terriza, L. Torner, *Superposition of noncoaxial vortices in parametric wave mixing*, Phys. Rev. E **66**, 036608 – 1-10 (2002).

[91] Y.S. Kivshar, E. Ostrovskaya, *Folding and Twisting Waves of Light*, Opt. Photon. News **12**, 24-29 (2001).

[92] L. Torner, D.V. Petrov, *Splitting of light beams with spiral phase dislocations into solitons in bulk quadratic nonlinear media*, J. Opt. Soc. Am. B **14**, 2017-2023 (1997).

[93] A. Dreischuh, D.N. Neshev, V.Z. Kolev, S. Saltiel, M. Samoc, W. Krolikowski, Y.S. Kivshar, *Nonlinear dynamics of two-color optical vortices in lithium niobate crystals*, Opt. Express **16**, 5406-5420 (2008).

[94] A. Berzanskis, A. Matijosius, A. Piskarkas, V. Smilgevicius, A. Stabinis, *Conversion of topological charge of optical vortices in a parametric frequency converter*, Optics Comm. **140**, 273-276 (1997).

[95] M.S. Soskin, M.V. Vasnetsov, *Nonlinear Singular Optics*, Pure Appl. Opt. **7**, 301-311 (1998).

[96] K. Dholakia, N.B. Simpson, M.J. Padgett, L. Allen, *Second-harmonic generation and the orbital angular momentum of light*, Phys. Rev. A **54**, R3742-R3745 (1996).

[97] J. Courtial, K. Dholakia, L. Allen, M.J. Padgett, *Second-harmonic generation and the conservation of orbital angular momentum with high-order Laguerre-Gaussian modes*, Phys. Rev. A **56**, 4193-4196 (1997).

[98] J. Arlt, K. Dholakia, L. Allen, M.J. Padgett, *Parametric down-conversion for light beams possessing orbital angular momentum*, Phys. Rev. A **59**, 3950-3952 (1999).

[99] S. Feng, P. Kumar, *Spatial Symmetry and Conservation of Orbital Angular Momentum in Spontaneous Parametric Down-Conversion*, Phys. Rev. Lett. **101**, 16302 – 1-4 (2008).

[100] R.W. Boyd, *Nonlinear Optics, Third Edition*, Academic Press, San Diego (2008).

[101] G. Molina-Terriza, J.P. Torres, L. Torner, *Management of the Angular Momentum of Light: Preparation of Photons in Multidimensional Vector States of Angular Momentum*, Phys. Rev. Lett **88**, 013601 – 1-4 (2002).

[102] G.I. Stegeman, D.J. Hagan, L. Torner, $\chi^{(2)}$ *cascading phenomena and their application to all-optical signal processing, mode locking, pulse compression and solitons*, Opt. Quant. Elecron. **28**, 1691-1740 (1996).

[103] M. Centini, C. Sibilia, G. D'Aguanno, M. Bertolotti, M. Scalora, M.J. Bloemer, C.M. Bowden, *Reflectivity control via second-order interaction process in one-dimensional photonic band-gap structures*, Optics Comm. **184**, 283-288 (2000).

[104] M.D. Feit, J.A. Fleck Jr., *Computation of mode properties in optical fiber waveguides by a propagating beam method*, Appl. Opt. **19**, 1154-1164 (1980).

[105] M. Centini, G. D'Aguanno, M. Scalora, M.J. Bloemer, C.M. Bowden, C. Sibilia, N. Mattiucci, M. Bertolotti, *Dynamics of counterpropagating pulses in photonic crystals: enhancement and suppression of stimulated emission processes*, Phys. Rev. E **67**, 036617 – 1-4 (2003).

[106] V.G. Dmitriev, G. Gurzzadyan, D.N. Nikogosyan, *Handbook of Nonlinear Optical Crystals, Third Edition*, Springer, Berlin (1999).

[105] F.A. Bovino, M. Braccini, M. Bertolotti, C. Sibilia, *Management of the orbital angular momentum of vortex bbeams in a quadratic nonlinear interaction*, Optics Comm. **284**, 2587-2593 (2011).

[106] S.S.R. Oemrawsingh, X. Ma, D. Voigt, A. Aiello, E.R. Eliel, G.W. 't Hooft, J.P. Woerdman, *Experimental Demonstration of Fractional Orbital Angular Momentum Entanglement of Two Photons*, Phys. Rev. Lett. **95**, 240501 – 1-4 (2005).

[107] F.A. Bovino, M. Braccini, M. Giardina, C. Sibilia, *Orbital Angular Momentum in Noncollinear Second Harmonic Generation by off-axis vortex beams*, J. Opt. Soc. Am. B **28**, 2806-2811 (2011).

List of Publications

- F.A. Bovino, M. Braccini, C. Sibilia, *Management of the Orbital Angular Momentum of vortex beams in a quadratic nonlinear interaction*, in *Fotonica 2010*, Atti del Convegno (2010).

- F.A. Bovino, M. Braccini, C. Sibilia, *On the OAM in a quadratic nonlinear interaction of off axis vortex beams*, in *Fotonica 2010*, Atti del Convegno (2010).

- V. Tasco, I. Tarantini, A. Campa, T. Stomeo, G. Epifani, A. Passaseo, M. Braccini, M.C. Larciprete, C. Sibilia, F.A. Bovino, *GaN/AlGaN photonic crystals designed for the enhancement of nonlinear effects*, in *Fotonica 2010*, Atti del Convegno (2010).

- T. Stomeo, G. Epifani, V. Tasco, A. Massaro, I. Tarantini, A. Campa, M. De Vittorio, A. Passaseo, M. Braccini, M.C. Larciprete, C. Sibilia, F.A. Bovino, *Fabrication of GaN/AlGaN 1D photonic crystals designed for nonlinear optical applications*, in Proc. SPIE **7713**, 771316 (2010).

- V. Tasco, I. Tarantini, A. Campa, A. Massaro, T. Stomeo, G. Epifani, A. Passaseo, M. Braccini, M.C. Larciprete, C. Sibilia, F.A. Bovino, *GaN/AlGaN microcavities for enhancement of nonlinear optical effects*, in Proc. SPIE **7713**, 77131Q (2010).

- F.A. Bovino, M. Braccini, C. Sibilia, *Orbital Angular Momentum of off-axis Vortex Beams in a Quadratic Nonlinear Interaction*, in *Nonlinear Photonics*, OSA Technical Digest (CD) (Optical Society of America, 2010), paper NME50.

- F. A. Bovino, M. Braccini, M. Bertolotti, C. Sibilia, *Vortex Beams in a Quadratic Nonlinear Interaction: Optical Control of the Angular Momentum of Light*, Fotonica 2011, Atti del Convegno, ISBN 9788887237122 (2011).

- F.A. Bovino, M. Braccini, M. Bertolotti, C. Sibilia, *Management of the Orbital Angular Momentum of Vortex Beams in a Quadratic Nonlinear Interaction*, Optics Comm. **284**, 2587-2593 (2011).

- F.A. Bovino, M. Braccini, C. Sibilia, M. Bertolotti, *Twin Photons Generation in an Integrated Photonic Crystal Structure*, in *Selected Topics in Photonic Crystals and Metamaterials*, Edited by A. Andreone, A. Cusano, A. Cutolo, V. Galdi, World Scientific Publishing Co. Pte. Ltd. ISBN: 13 978-981-4355-18-6 10 981-4355-18-6 (2011).

- F.A. Bovino, M. Braccini, M. Giardina, C. Sibilia, *Orbital Angular Momentum in Noncollinear Second Harmonic Generation by off-axis vortex beams*, J. Opt. Soc. Am. B **28**, 2806-2811 (2011).

- F.A. Bovino, M. Braccini, A. Benedetti, *Piastra plasmonica per la generazione di vortici ottici*, Italian Patent No. TO2011A000682 (2011).

- F.A. Bovino, M. Braccini, *Piastra di fase regolabile in altezza per la generazione di vortici ottici*, Italian Patent No. TO2011A000683 (2011).

Acknowledgements

Sono passati tre lunghissimi anni da quando ho deciso di intraprendere questa sfida del dottorato. Seguire questa strada è stata una scelta in parte sofferta, in parte desiderata, che mi ha fatto vivere grandi soddisfazioni ma anche momenti di difficoltà, in cui la fiducia in me stesso ha vacillato un po' più del dovuto. Ovviamente, l'essere arrivato fino a questa pagina della tesi significa che, tutto sommato, alla fine ce l'ho fatta. È altrettanto ovvio dover ringraziare persone, cose ed entità che mi hanno permesso di raggiungere i miei obiettivi.

Come da immodestissima tradizione comincio con il ringraziare il sottoscritto, perché, nonostante tutto e tutti, ha abbondantemente contribuito a questa impresa con la sua tenacia (o forse sarebbe meglio dire ostinazione) ed il suo ottimismo, che ha sempre finito per trionfare in molti dei momenti più bui… e perché in questi tre anni ha compiuto il suo Rito di passaggio e la sua (Ri)Cerca.

Poi ringrazio Marta, la donna che, dall'ultima volta che ho scritto una pagina di ringraziamenti, è nel frattempo diventata mia moglie. A lei dedico questa tesi perché ha condiviso tutto con me, esaltandomi nei successi e sollevandomi nello sconforto. A lei perché si è presa cura di me tutte quelle volte che la mia autosufficienza mentale è venuta meno… e anche le altre. Perché mi ha sopportato nell'isteria di questi ultimi mesi, consentendomi di sfruttare al meglio ogni momento e perché dopo quasi sei anni continua a farmi una propaganda spudorata.

Perché ha scelto di essere la compagna della mia vita.

Ringrazio mio Padre e mia Madre, perché hanno sempre meritato la maiuscola. Perché mi hanno sostenuto e fatto diventare quello che sono; hanno sempre appoggiato incondizionatamente tutte le mie idee e scelte, per quanto strambe potessero essere, dispensandomi tanti di quei consigli che (qui lo posso scrivere) in più di un'occasione hanno fatto la differenza. Li ringrazio perché non hanno mai permesso che le nostre incomprensioni ci tenessero lontani. Perché so che potrò sempre contare su di loro.

Grazie a mia Zia Vera (un nome unico) perché è stata ed è la mia zia preferita, il mio terzo genitore e la mia testimone di matrimonio; perché mi ha aiutato in tutti i momenti difficili della mia vita e perdonato tutte le mie negligenze, mettendomi davanti a tutto il resto. Per la sua disponibilità, per le chiacchiere e per le polpette. E perché c'è sempre stata.
Grazie ai miei suoceri, la mia famiglia acquisita, perché fin dall'inizio mi hanno sempre trattato come uno di casa e perché, se mai dovesse esistere (a torto) un fan club intitolato a me, sono sicuro che loro ne sarebbero i presidenti. E grazie anche a Elsa, che ora è diventata mia cognata, per tutto il buon umore che si porta dietro.

Un ringraziamento particolare alla Prof per avermi seguito in questi tre anni, facendomi da guida nel mondo della ricerca ed incoraggiandomi nel mio lavoro.
Grazie a Fabio, che è stato il mio mentore e anche un amico; per tutte le dritte e gli insegnamenti; per le idee che mi ha dato, perché è riuscito sempre a trovare del tempo per far progredire il mio lavoro e per l'ospitalità nei miei giorni genovesi.
Grazie ad Alessandro, per tutto l'affetto che mi ha dimostrato, per le sue impagabili lezioni di fisica e di metafisica, per le lunghe chiacchierate e per avermi fatto scoprire il vero kung fu.
Grazie ad Alessio, un vero amico trovato nel seminterrato del Dipartimento di Energetica quando meno me lo aspettavo, perché con le sue stravaganze mi ha tirato su di morale più di una volta; grazie anche per tutto l'aiuto che mi ha dato per risolvere i miei problemi tecnici.
Grazie anche a Marco per la sua assistenza e i consigli che hanno colmato una buona parte delle mie (numerosissime) lacune. E grazie anche a tutti gli altri del laboratorio perché ho avuto la possibilità di imparare da ciascuno di loro giorno dopo giorno.

E grazie ad Andrea, perché ha saputo essermi amico giorno dopo giorno, rendendo la nostra amicizia sempre più salda; perché abbiamo affrontato il bello e il cattivo tempo insieme; grazie, perché adesso è uno di famiglia.
Grazie a Giacomo, mio amico da una vita e testimone di nozze, perché ho l'orgoglio di poter dire che sono decenni che ci conosciamo e riusciamo

ancora a superare insieme la burrasca, e perché ha voluto rinnovare la nostra amicizia.
Grazie a Paolo, che ha sopportato tanto negli anni, perché anche lui è un amico di cuore.
Grazie a Fabrizio, amico lontano ma sempre vicino, perché siamo sempre andati al di là di tutto, perché dopo tanto, continuiamo ancora a raccontarci le stesse follie su un mondo migliore. Perché con le sue originalità ha reso tantissimi periodi della mia vita degni di essere vissuti.
Grazie anche a Chiara perché, anche se ci siamo un po' persi, è stata la mia grandissima amica per tanti anni.
E grazie a Fra perché sarà sempre l'unico orsetto glutinoso con cui spero di scalare il Machu Pichu, a Valter per la sua zanzara e a Marina per il suo sarcasmo.
Grazie a Stefano e a Donatella, amici veri, persone su cui so di poter sempre contare e che spero di avere sempre accanto; grazie per il loro entusiasmo e il loro infinito affetto.
E poi grazie a tutti gli altri, agli amici presenti, a quelli assenti e a quelli che amici non lo sono più ma che hanno reso sicuramente la mia vita più bella.
Grazie a tutti i ragazzi della kwoon ed al kung fu perché è una scuola di vita.

Grazie a Sheldon, Leonard, Howard e Rajesh perché sono stati la colonna portante del mio dottorato, permettendomi di comprendere al meglio la Teoria del Big Bang. E siccome sono nerd fino in fondo, grazie anche a Dexter e alla flotta del comandante Adama, perché mi (ci) hanno tenuto compagnia in molte serate di questi ultimi 3 anni, e soprattutto perché hanno nerdizzato mia moglie.

Infine grazie a chi mi sono dimenticato di citare, perché non se la prenderà e capirà che è solo colpa del mostruoso ritardo con cui sto scrivendo queste ultime pagine; e grazie a chi ha avuto la pazienza di leggere questo lavoro…o anche solo queste ultime tre pagine.

Roma, 30 Novembre 2011

It's been three years since I started this challenge with myself called PhD. Choosing this path was a both a hard and satisfying road, plenty of success and dark times. Obviously, since I am writing these last pages, in the end it seems that I succeeded; and of course for this it is expected me to thank people, things and entities.
As usual, my humbleness imposes me to begin to thank Myself, for the contribution to this enterprise in terms of persistency (or better, stubbornness) and optimism which allowed to pass safe through the darkest times…and because in these three years he completed his Rite of passage and his (Re)Search.
Then I want to thank Marta, the woman who, since last I wrote acknowledgements on a thesis, became my wife. This thesis is dedicated to her, because we shared all, glorifying mi victories and comforting me in the darkest hours. To her, since she took care of me all the times that my mind was not enough…and even all the others. Because she tolerated my hysteria in the last few months, allowing me to write this thesis, e because, after almost six years, she continues to promote me.
Because she chose to share the life with me.
I want to thank mi Father and Mother, because they always deserved the capital letter. Because the supported me, allowing to become what I am. Furthermore they supported my choices and ideas, no matter how strange they were, and gave me advice, which revealed as helpful more than one time. I thank them because I can always count on them.
Thanks to Zia Vera, my favorite aunt, my third parent, and my wedding witness; because she helped me in the hardest times, and forgave me for my negligence. For her willingness, for chattering and for her meat balls. And because she is always there.
Thank to my parents in law, my adoptive family, because, since the beginning they treated me as one of the family, and because, if one day will exist a fan club with my name, I am sure that they would be presidents. Thanks to Elsa, who became my sister in law, for her positive mood.

A special thank goes to Prof. Sibilia, for guiding me in the amazing world of scientific research, encouraging me in my work as researcher.

Thanks to Fabio, my mentor and friend; for the tips and teachings of these three years, for the ideas, and for his effort to find time to assist me. And thanks for the hospitality in my days in Genova.
Thanks to Alessandro, for the affection he showed to me, for his valuable physics and metaphysics lessons, and for introducing me to the authentic kung-fu.
Thanks to Alessio, a real friend found in the basement of the Energetics Department, since his extravagances cheered me up a lot of times. Thanks also for all the technical help he gave to me.
A thanks also to Marco, for his assistance and scientific advices. And thanks to all people in my lab because each of them taught me something, day after day.

Thanks to Andrea, because he became one of my best friends, since we faced together good times and bad times. Thanks because now he is part of my family.
Thanks to Giacomo, my friend for a lifetime and best man, because I am proud to say that we have been knowing each other for decades, and because he decided to renew our friendship.
Thanks to Paolo, who tolerated our jokes for years, because he is one a very good friend.
Thanks to Fabrizio, friend living far away, but always near, because we continue to tell each other how we want to change the world. Because he made many years of my life worthy of being experienced.
Thanks also to Chiara, because, even though we are no more in touch, she has been my best friend for years.
And thanks to Fra, because he will always be my glutinous little bear, hoping that we can climb Machu Pichu soon, to Valter for his mosquito and to Marina for her sarcasm.
Thanks to Stefano and Donatella, true friends, people I know I can rely, hoping to keep them always beside me; thanks for their enthusiasm and infinite affection.
Then thanks to all other friends, who is here, and who is not, and to who is not a friend anymore, but made my life better anyway.

Thanks to all guys of the kwoon, and to kung fu for it is a way of life.

Thanks to Sheldon, Leonard, Howard and Rajesh, the spine of my PhD, since they allowed me to understand at best the Big Bang Theory. And, since I am nerd to the bone, thanks to Dexter and the fleet of commander Adama, because they accompanied me (us) during many nights of the last three years and, most of all, because they nerdizated my wife.

Finally I would like to thank people I forgot, since I know they would not be upset for this, hoping that they would understand how I am late in writing these last pages; and thanks to who had the patience to read this thesis…or even only the last three pages.

Rome, November 30, 2011